

MAGYAR ÁLLAMI
EÖTVÖS LORÁND
GEOFIZIKAI INTÉZET

GEOFIZIKAI
KÖZLEMÉNYEK

ВЕНГЕРСКИЙ
ГЕОФИЗИЧЕСКИЙ
ИНСТИТУТ
ИМ Л. ЭТВЕША

ГЕОФИЗИЧЕСКИЙ
БЮЛЛЕТЕНЬ

EÖTVÖS LORÁND
GEOPHYSICAL INSTITUTE
OF HUNGARY

GEOPHYSICAL TRANSACTIONS

CONTENTS

Modelling of multilayered media by computer processing of well logs	<i>Vermes M.</i>	187
Problems of seismic migration with erroneous velocity	<i>Kostecki A., Pólchlopek A.</i>	203
Computing of transient response of layered halfspace; problems in apparent resistivity inversion	<i>Prácser E.</i>	221
A model for the vertical subsurface radon transport in "geogas" microbubbles	<i>Várhegyi A., Baranyi I., Somogyi Gy.</i>	235
Earthquakes in the region of Komárom, Mór and Várpalota	<i>Szeidovitz Gy.</i>	255

VOL. 32. NO. 3. DEC. 1986. (ISSN 0016-7177)



TARTALOMJEGYZÉK

Rétegsor meghatározás karotázs szelvények számítógépes feldolgozásával	<i>Vermes M.</i>	202
A hibás sebességgel végrehajtott szeizmikus migráció néhány kérdéséről	<i>Kostecki A., Pólichlopek A.</i>	220
Rétegzett féltér tranziens válaszána számítása, látszólagos fajlagos ellenállás meghatározása	<i>Prácser E.</i>	234
Geogáz mikrobuborékok segítségével megvalósuló felszínalatti, vertikális radon transzport modellje	<i>Várhegyi A., Baranyi I., Somogyi Gy.</i>	253
Földrengések Komárom, Mór és Várpalota környezetében	<i>Szeidovitz Gy.</i>	274

СОДЕРЖАНИЕ

Определение геологического разреза с помощью обработанных на ЭВМ каротажных данных	<i>М. Вермеш</i>	202
О некоторых вопросах сейсмической миграции, осуществленной с неправильной скоростью	<i>А. Костецки, А. Полхлопек</i>	220
Расчет поля переходного процесса над слоистым полупространством, определение кажущегося удельного сопротивления	<i>Э. Прачер</i>	234
Модель подземного вертикального переноса радона, осуществляемого с помощью микропузырей геогаза	<i>А. Вархеци, И. Барани, Д. Шомоди</i>	253
Землетресения в окрестности гг. Комаром, Варпалота, Мор	<i>Д. Сейдович</i>	274

MODELLING OF MULTILAYERED MEDIA BY COMPUTER PROCESSING OF WELL LOGS

Mátyás VERMES*

The determination of the layered model from some well logs recorded in a single borehole is discussed. The problem is traced back to the determination of step functions fitting optimally to the well logs. The discontinuities of these step functions are correlated and the average width of the steps can be regulated. The step functions are given as the realizations of a multidimensional Markov chain. Mutual correspondence can be prescribed between the possible states of the Markov chain and the rocks of the investigated area. Using the transition probability matrix such a priori information can be introduced to the algorithm which are characteristic to the combination of the applied tools as well as the geological circumstances in the borehole. As a consequence when fitting the step functions the algorithm is able to distinguish between physically sensible and nonsensical combinations of the parameters. In the last part of the paper models are examined in which the slow variation of the petrophysical parameters is permitted inside the layers.

Keywords: well logging, models, Markov chain, physical parameters, optimization

1. Introduction

Modelling the stratified earth by a stochastic process is not a new concept in the technical literature. The Markov chain model seems to be very useful for certain practical applications [DOWDS 1969]. The Markov chain can be regarded as a simple extension of an independent white noise process, allowing some dependence of each sample on the preceding sample and only on it [FELLER 1978]. This property makes possible the application of simple combinatoric optimizing algorithms for certain fitting problems [LAWLER 1982]. The fitting of acoustic impedance logs and step functions deduced from the Markov chain model was reported by Godfrey et al., using the dynamic programming technique proposed by Bellman [GODFREY et al. 1980, LAWLER 1982]. The results reported by the foregoing authors will be generalized from several aspects in the present paper.

The use of multidimensional Markov chains makes possible the common interpretation of several types of well logs measured in the same borehole. This fact significantly increases the effectiveness of the interpretation. Certain possible states of the Markov chain — certain combinations of rock physical properties — can be related to certain lithological units existing in the given

* Geophysical Exploration Company (GKV), POB 213, Budapest, H-1391 Hungary
presently: Geophysical Department of L. Eötvös University 1083. Budapest, Kun Béla tér 2
Manuscript received: 10 July, 1986

area. It is stressed in this paper that the application of predefined Markov chain transition probability matrices gives means to the interpreter geophysicist to use the a priori information available for a given area.

2. Modelling with step functions

The structure of the collected experimental data and the properties of the mathematical model of a stack of horizontal layers is described below to explain the essence of the modelling. Let us suppose that we have L different logs of the same borehole, for example SP, acoustic log, etc. Denoting the depth sample interval by Δz , the depth of each i -th sample can be expressed as $i\Delta z$ ($i = 0, \dots, N$). The i -th values of the different log samples are denoted by $u_i^1, u_i^2 \dots u_i^L$, respectively. Thus, the lower index i relates to the depth, the upper index shows the particular type of logging tool applied. The experimental data can be denoted in the following compact matrix form:

$$U = \{u_i^{(l)}\} \quad (i = 0, 1, \dots, N; l = 1, 2, \dots, L)$$

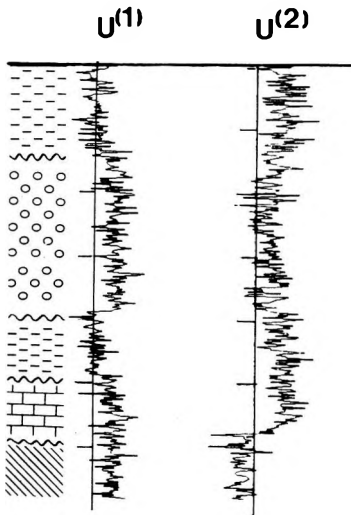


Fig. 1. The recorded logs

1. ábra. A mérési anyag

Рис. 1. Материал измерений

Figure 1 shows a lithological column of a borehole, and two acquired logs $u^{(1)}$ and $u^{(2)}$ respectively. Initially, the idealized layer stack is assumed as having the following properties:

- a) Each layer is homogeneous, i.e. all physical parameters are constant within a layer. The theoretical value characteristic for each layer is denoted by $v_i^{(l)}$ using the same indices as above. If the lower and upper boundaries of the layer are $i_1\Delta z$ and $i_2\Delta z$ respectively, then $v_i^{(l)}$ is constant in the case of $i_1 \leq i < i_2$.

- b) At least one of the $v_i^{(l)}$ functions will change at the layer boundaries. So $v_{i-1}^{(l)} \neq v_i^{(l)}$ for one or more l values if there is a layer boundary at depth $i\Delta z$. It follows from the above two conditions that the theoretical $v_i^{(l)}$ functions are discrete step functions with possible discontinuities at the layer boundaries.

Note: These conditions may seem too restrictive and a very poor approach to reality. The main argument may be that there exist layer sequences where the layers are not homogeneous and there are geological boundaries where none of the given logs have discontinuities. Since only L parts of the logs are used in the modelling of the layer stack, there is no possibility of separating such layers that are not visible on the logs. Thus the resultant model corresponds to rock intervals separated on the bases of physical properties rather than lithological section. An important further aim is to reveal the relationship between physical properties and lithology. This problem will only be briefly mentioned when specifying the transition probability matrix.

Figure 2 shows a schematic lithological column and the idealized model of well logs 1 and 2 along the same borehole as in Fig. 1. Functions $v^{(1)}$ and $v^{(2)}$ represent the theoretical values of the physical parameters measured by logging tools 1 and 2. Steps are present only at layer boundaries. Although there are no steps at every layer boundary, steps of the different functions are correlated.

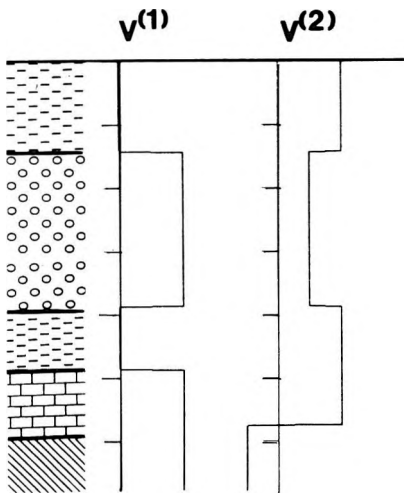


Fig. 2. The layered model

2. ábra. A rétegmodell

Рис. 2. Пластовая модель

Until the last part of this paper we accept the concept of homogeneous layers. Since, it implies neglecting the inner variations and regarding the major changes only provided by the actual resolution, we take it that the concept of homogeneous layers is fundamental from several aspects, as related to the problem of fitting a model to measured data.

The differences between the corresponding functions of Figs. 1 and 2 can be regarded either as measurement errors or the effect of the inhomogeneity

within the assumed "layers". The aim of the interpretation is to find those functions $v^{(l)}, \dots, v^{(L)}$ belonging to the measured functions $u^{(l)}, \dots, u^{(L)}$ that fulfil the following requirements:

a) The average length of steps of function $v^{(l)}$ must easily be able to be controlled.

b) The functions $v^{(l)}$ of the given average step length must be optimally fitted in the statistical sense to the original data $u^{(l)}$.

c) The steps of functions $v^{(l)}$ must be correlated. Thus, every layer boundary is defined as one or more steps in functions $v^{(l)}$. In ideal cases the lithology can be deduced from values $v^{(l)}$ as in the case of Fig. 2.

Finally, what can be done with such layer sequences in which the physical parameters change gradually within the layers? This problem is faced in the last part of the paper. It will be shown that the mathematical model (Markov chain) can also be generalized into the case of inhomogeneous layers. A method will be given to reduce this general case to the more simple case of homogeneous layers.

3. Construction of the Markov chain

As was shown above, construction of the mathematical model means a search for such a step function that fulfils requirements a), b) and c). Now, the mathematical representation of functions $v^{(l)}$ will be discussed. These functions will be regarded as the realization of an L dimension Markov chain. The idea of modelling with a Markov chain was taken from the paper of GODFREY et al. [1980]. The generalization of Godfrey's solution into several dimensions has proved to be important from practical aspects rather than from the mathematical point of view.

The alternative formulation of the problem of modelling leads to further differences. As a consequence, certain parameters of the Markov chain will have a meaning here that is different from that in GODFREY et al. [1980]. These difference will be stressed later in the text. Let the i -th sample of the L dimension series $\{v_i\}_{i=0}^N$ be

$$v_i = \begin{bmatrix} v_i^{(1)} \\ v_i^{(2)} \\ \vdots \\ v_i^{(L)} \end{bmatrix} \quad (1)$$

where v_i is an L dimensional column vector. In the case of fixed upper index l , $\{v_i^{(l)}\}_{i=0}^N$ is a function characterizing the l -th physical parameter. For simplicity, the set of values of step functions $v^{(l)}$ is supposed as being discrete. The possible values of $v^{(l)}$ are denoted as $x_1^{(l)}, x_2^{(l)}, \dots, x_m^{(l)}$, which means that the l -th physical parameter can have m discrete values only. This restriction is hardly critical if the values $x_1^{(l)}, \dots, x_m^{(l)}$ are dense enough in the range of practically occurring

parameter values. It can be concluded from this restriction that the set of possible values of the parameter combinations of models $\{v_i\}$ will also be discrete. The possible values of vectors v_i will be samples of a state space of $M = m_1 m_2 \dots m_L$ elements. If the elements of this state space are arbitrarily ordered, then the possible values of v_i can be assigned (omitting the upper index) by x_j ($j = 1, 2 \dots M$). One combination of physical parameters may be for example:

$$v_i = x_j = \begin{bmatrix} x_{j_1}^{(1)} \\ x_{j_2}^{(2)} \\ \vdots \\ x_{j_L}^{(L)} \end{bmatrix} \quad j_i = 1, \dots, m_i \quad (2)$$

if the state represented by the right hand side column vector of Eq. (2) comes to the j -th place during the ordering process.

Let us start with the description of statistical parameters. Denoting the probability independent from i with α_j

$$\alpha_j = Pr(v_i = x_j) \quad (3)$$

where $\sum_{j=1}^M \alpha_j = 1$. The column vector containing the elements α_j is denoted as $\bar{\alpha}$; the value of α_j shows the probability of state x_j of the physical parameters of a particular layer. This probability is the parameter of the interpretation algorithm so it must be specified independently from the actual measured data U . In the simplest cases the probability distribution $\bar{\alpha}$ can be regarded as uniform; $\alpha_j = 1/M$. Of course there are more interesting possibilities.

Up to now $\{v_i^{(h)}\}$ was considered as the function characterizing the l -th physical parameter, neglecting its actual meaning. Sometimes the probabilities of certain lithology and the corresponding parameter combinations are known a priori in the case of a given set of logging tools based on geological and geophysical considerations. Similarly the low probabilities of certain unacceptable (senseless) combinations are also known. If one has such an unacceptable measured data set at a certain depth it seems reasonable to regard the data as "noisy" and take them into consideration with smaller weight.

For example let us suppose that we have used two logging tools, both sensitive to resistivity ($L = 2$). Obviously the combinations $x_j^{(1)} \cong x_j^{(2)}$ will have large a priori probability α_j , all the others will have a small α_j or zero. In this way the interpreter can put in the algorithm significant a priori information by giving the $\bar{\alpha}$ distribution.

Markov chain modelling was introduced by GODFREY et al. as a noise cancelling procedure. The probabilities α_j were estimated by the relative frequencies computed from the measured data. So the distribution $\bar{\alpha}$ is the parameter of the experimental data U in their approach. Here a quite different approach is used. Let us suppose for example that we want to detect a thin layer

between two thick ones. Merely because of the geometrical conditions, the relative frequencies would result in very small value α_j for the physical parameter combination of the thin layer — which would exclude the data connected with the presence of the thin layer from the interpretation. It is obvious from the example that the distribution $\bar{\alpha}$ must represent the interpretability of a given combination x_j as real physical parameters of some lithology rather than the probability of some lithology.

Fixing the probabilities α_j and assuming an independent (white) noise process, the a priori probability of a given realization $V = (v_0, v_1, \dots, v_N) = x_{j_0}, \dots, x_{j_N}$ in the case of equal α_j values ($\alpha_j = 1/M$) would be:

$$Pr(V) = Pr(v_0 = x_{j_0}) \dots Pr(v_N = x_{j_N}) = \left(\frac{1}{M}\right)^{N+1}$$

Since $Pr(V)$ is equal for every realization, and the bulk of them represent fast abrupt variations between states x_j , such types of functions do not fulfil the restriction made on step-like behaviour. To ensure this latter property, some further statistical properties of the process must be taken into consideration and the restriction made on the independence of samples must be weakened. The most general expression of the previous probability $Pr(V)$ is:

$$Pr(V) = \prod_{i=0}^N Pr(v_i | v_{i-1}, v_{i-2}, \dots, v_0)$$

where the conditional probabilities express that the samples depend on all the previous samples. We limit ourselves to the case for which each sample v_i depends only on the previous sample v_{i-1} :

$$Pr(V) = Pr(v_0)Pr(v_1|v_0)\dots Pr(v_N|v_{N-1}) \quad (4)$$

This expression takes the form of

$$Pr(V) = \alpha_i Pr(v_1 = x_j | v_0 = x_i) Pr(v_2 = x_k | v_1 = x_j) \dots$$

$N + 1$ factors

using a given realization $V = (x_i, x_j, x_k, \dots)$ and the notation $Pr(v_0 = x_i) = \alpha_i$. Expression (4) is just the definition of a Markov chain. Let us introduce the annotation:

$$P_{jk} = Pr(v_i = x_k | v_{i-1} = x_j) \quad (5)$$

P_{jk} is the probability of state x_k of a random process $\{v_i\}$ with the condition that the state of the previous sample was x_j . P_{jk} , like the distribution $\bar{\alpha}$, is regarded to be independent from index i (the depth). In other words P_{jk} is the probability of the jump of the process from state j to k , thus

$$\sum_{k=1}^M P_{jk} = 1 \quad (6)$$

The matrix built up from elements P_{jk} -s is called a transition probability matrix and is denoted by P . This matrix gives a means of controlling the average thickness of "layers". The more dominant the elements of the main diagonal, the thicker the layers. For example if P_{jj} approaches unity, then the process is able to stay in an x_j state for a long time.

Now we examine some properties of matrix P and fix it to suit our purposes. Let us regard the following probability distribution to be known for a given:

$$p_j(i) = Pr(v_i = x_j) \quad j = 1, \dots, M \quad (7)$$

It can easily be shown that the probability distribution of the next sample $i + 1$ can be computed by $p_j(i)$

$$\bar{p}^T(i+1) = \bar{p}^T(i)P \quad (8)$$

using the notation $\bar{p}(i)$ for the column vector built up from elements $p_j(i)$ and T for transposition. As expected, the effect of the first state will vanish so the limit value

$$\lim_{n \rightarrow \infty} \bar{p}^T(i+n) = \lim_{n \rightarrow \infty} \bar{p}^T(i)P^n \quad (9)$$

is independent of $\bar{p}(i)$. This is true and it can be shown that

$$\lim_{n \rightarrow \infty} \bar{p}^T P^n = \bar{\alpha}^T \quad (10)$$

FILE:EC53 M: 2-2 YAC920e korr. elgi 39-

for all \bar{p} and

$$\bar{\alpha}^T P = \bar{\alpha}^T. \quad (11)$$

According to Eqs. (10) and (11), $\bar{\alpha}$ is the so called invariant distribution of the Markov chain. Let us specify matrix P in the form:

$$P = \lambda I + (1 - \lambda) \begin{bmatrix} \bar{\alpha}^T \\ \bar{\alpha}^T \\ \vdots \\ \bar{\alpha}^T \end{bmatrix} \quad (12)$$

where I is the unit matrix and λ is a scalar. This definition is valid only if P fulfils Eqs. (6) and (11). It can easily be shown that the matrix P defined by Eq. (12) satisfies (6) and (11). Since λ controls the magnitude of the elements in the main diagonal of matrix P , λ is directly related to the average layer thickness. For example $\lambda=0$ is the case of the independent random (white) process with minimum thickness. In the case of $\lambda \rightarrow 1$ the medium will contain only one "layer" or, in other words, the process $\{v_j\}$ will stay in state x_j for all i -s. This is the case of maximum thickness. Now taking $v_i = x_j$, the probability of the process remaining in the same (j -th) state along $n - 1$ steps can be calculated:

$$\begin{aligned} Pr(v_i = v_{i+1} = \dots = v_{i+n-1} = x_j, v_{i+n} \neq x_j) = \\ = P_{jj} P_{jj} \dots P_{jj} (1 - P_{jj}) = (1 - P_{jj}) P_{jj}^{n-1} \end{aligned} \quad (13)$$

The average thickness of the layer of state x_j can be expressed by calculating the expected value of n steps:

$$w_j = (1 - P_{jj}) \sum_{n=1}^{\infty} n P_{jj}^{n-1} = \frac{1}{1 - P_{jj}} = \frac{1}{(1 - \lambda)(1 - \alpha_j)}. \quad (14)$$

Hence, Eq. 14 gives a simple tie between λ and the average layer thickness w_j . Let us refer again to the paper of GODFREY et al. [1980], where λ is also regarded as a parameter of the experimental data U , and the evaluation at λ from U is detailed. λ in this paper is used as a simple parameter affecting the resultant average layer thickness only. Since the desired resolution of the model depends on the aim of the interpretation, λ must be chosen independently from the experimental data U . For seismic purposes resolution between 10 and 500 m seems desirable.

Summarizing the above concept, if the probabilities α_j and a parameter λ are prescribed, the transition probability matrix P can be constructed and an L dimension Markov chain can be defined. Functions $\{v_i^{(l)}\}$ derived in this way fulfil requirements a) and c) formulated in Section 2. In other words these are step functions with controllable step length and the steps are correlated along different function implementations. These functions $\{v_i\}$ have a priori probabilities according to Eq. 4.

4. Matching of step functions

The next step is to select the implementation from set $\{v_i\}$ whose functions $v_i^{(l)}$ fit best the original experimental data U , according to requirement b) in Section 2. Let us examine the so called additive model of experimental data [HOLTZMAN 1971]:

$$U = V + N \quad (15)$$

where U is the matrix of the measured data, V is the matrix containing the theoretical values of physical parameters of the possible rock column, and N is the difference between the previous two quantities. V will be chosen so that N should be sufficiently small. Elements of N will be regarded as noise and obviously $n_i^{(l)} = u_i^{(l)} - v_i^{(l)}$ and $Pr(N) = Pr(U|V)$. Elements of N are supposed to be independent with normal distribution, zero mean and standard deviation σ_i . However, it should be noted that there are other acceptable alternatives for the independence and the distribution type, which could be incorporated in the following derivations with minor changes. For example n_{i-1} and n_i may be correlated and σ_i may vary with the depth, or other types of distributions can be applied [GODFREY et al. 1980].

The a posteriori probability $Pr(V|U)$ is maximized to find the optimal solution. This solution matrix \hat{V} is characterized by large a priori probability (Eq.4) and results in small noise N :

$$\hat{V} = V\{\max Pr(V|U)\}. \tag{16}$$

Using the Bayes theorem

$$\hat{V} = V\left\{\max \frac{Pr(U|V)Pr(V)}{Pr(U)}\right\}. \tag{17}$$

Taking into consideration that the maximum does not depend on the denominator, and by taking the negative logarithm of the terms we may write:

$$\hat{V} = V\{\max Pr(U|V)Pr(V)\} = V\{\min [-\ln Pr(U|V) - \ln Pr(V)]\}. \tag{18}$$

Using the condition of independence and Eq. (4):

$$\hat{V} = V\left\{\min \left[-\sum_{i=0}^N \sum_{l=1}^L \ln Pr(u_i^{(l)}|v_i^{(l)}) - \sum_{i=0}^N \ln Pr(v_i|v_{i-1}) \right]\right\}. \tag{19}$$

All terms on the right hand side of Eq. (19) are known and are computable.

The following expression can be derived for the function to be minimized by taking into consideration the restrictions made on the distribution type of quantities $n_i^{(l)}$, using the annotations α_j and P_{jk} in the case of an actual realization $V = (x_{j0}, x_{j1}, \dots)$, viz.

$$C(V) = \frac{1}{2} \sum_{i=0}^N \sum_{l=1}^L \left(\frac{(u_i^{(l)} - x_{ji}^{(l)})^2}{\sigma_l} \right) - \ln \alpha_{j0} - \sum_{i=1}^N \ln P_{j_{i-1}, j_i}. \tag{20}$$

The terms of Eq. (19) independent from V have been omitted since these have no influence on the position of the minimum. The solution \hat{V} can be evaluated by minimizing the cost function (Eq. 20). The following notations are introduced:

$$D_{j,i} = \frac{1}{2} \sum_{l=1}^L \left(\frac{u_i^{(l)} - x_j^{(l)}}{\sigma_l} \right)^2 \tag{21}$$

$$i = 0, 1, \dots, N; j = 1, 2, \dots, M$$

where $D_{j,i}$ is the cost increment originating from the difference between the measured $u_i^{(l)}$ and the theoretical $v_i^{(l)} = x_j^{(l)}$ values at the i -th point. Let us take

$$T_{j,k} = -\ln P_{jk} \tag{22}$$

$$j, k = 1, \dots, M$$

where $T_{j,k}$ is the cost increment originating from the transition from state $v_{i-1} = x_j$ to state $v_i = x_k$. Let us introduce the following recursion scheme:

$$\begin{aligned}
 C_{j,0} &= -\ln \alpha_j + D_{j,0} \\
 C_{j,i+1} &= \min_k \{C_{k,i} + T_{k,j}\} + D_{j,i+1} \\
 i &= 0, 1, \dots, N \\
 j, k &= 1, 2, \dots, M
 \end{aligned}
 \tag{23}$$

If the end point of V is fixed at $v_N = x_j$, then the minimum cost computed by Eq. (20) will be equal to $C_{j,N}$. This property of the above recursion can be proved by complete induction on index N .

In the case $N=0$ this statement is trivial. Now, if the validity holds for $C_{k,N-1}$ ($k = 1, \dots, M$), then the minimum cost value of an implementation of end points $v_{N-1} = x_k$ and $v_N = x_j$ is $C_{k,N-1} + T_{k,j} + D_{j,N}$. Since the optimum implementation with end point $v_N = x_j$ is also a member of this set, the cost belonging to this is the same as the k minimum. Q. E. D.

To find the optimum function $\{v_j\}$ $C_{j,i}$ costs must be computed for every $j = 1, \dots, M$ and $i = 0, \dots, N$, while keeping the indices k giving the minimum in Eq. (23). The optimum $\{v_i\}$ can be found by tracking indices k backwards from the point having minimum cost $C_{j,N}$. The resultant coordinates give the step functions $\{v_i^{(l)}\}$.

5. Examples

A synthetic example is shown in Fig. 3. The idealized step functions A, B, C and D are four components of a realization of a Markov chain described in Section 3. The components consist of 1000 samples, each of them with four possible values. So the state space consists of $M = 4^4 = 256$ points. The distribution $\bar{\alpha}$ was chosen to be uniform, λ determining the average step length was 0.97. Functions E, F, G and H were produced by adding Gaussian, zero mean independent noise to A, B, C and D . Functions E, F, G and H were used as input for the algorithm. Functions I, J, K and L are the results which can be regarded as estimates of functions A, B, C and D . The good fit shows — there are only minor differences — the superior performance of the algorithm.

Figures 4 and 5 show a (four component) field example processed with different parameters. The four components (A, B, C and D) are compensated γ - γ , γ -ray, neutron-neutron, and resistivity logs respectively. The length of the functions is 150 m, with 1 m sampling rate. The result is represented by the step functions E, F, G and H , with value sets of 3, 5, 4 and 8 respectively. So, the state spaces consist of $3 \times 5 \times 4 \times 8 = 480$ points. In both cases $\bar{\alpha}$ distribution was assumed to be uniform and $\lambda = 0.98$ was used. The difference between the two results — the model exhibited in Fig. 4 is more detailed than in Fig. 5 — was caused by the different standard deviation term of noise applied. σ_i was greater in the latter case. If the parameter is increased, then the weight of the deviation term (in Eq. 20) becomes smaller, so the solutions of fewer steps become more probable, or in other words the resolution is decreased. It is quite

natural that increased noise results in smaller resolution. σ_l is also regarded to be a parameter of the interpretation similarly to $\bar{\alpha}$ and λ .

Figures 6 and 7 show a density and an acoustic log (A, B) and the two different step function models (C, D) fitted to the input data. The result was used for seismic interpretation purposes.

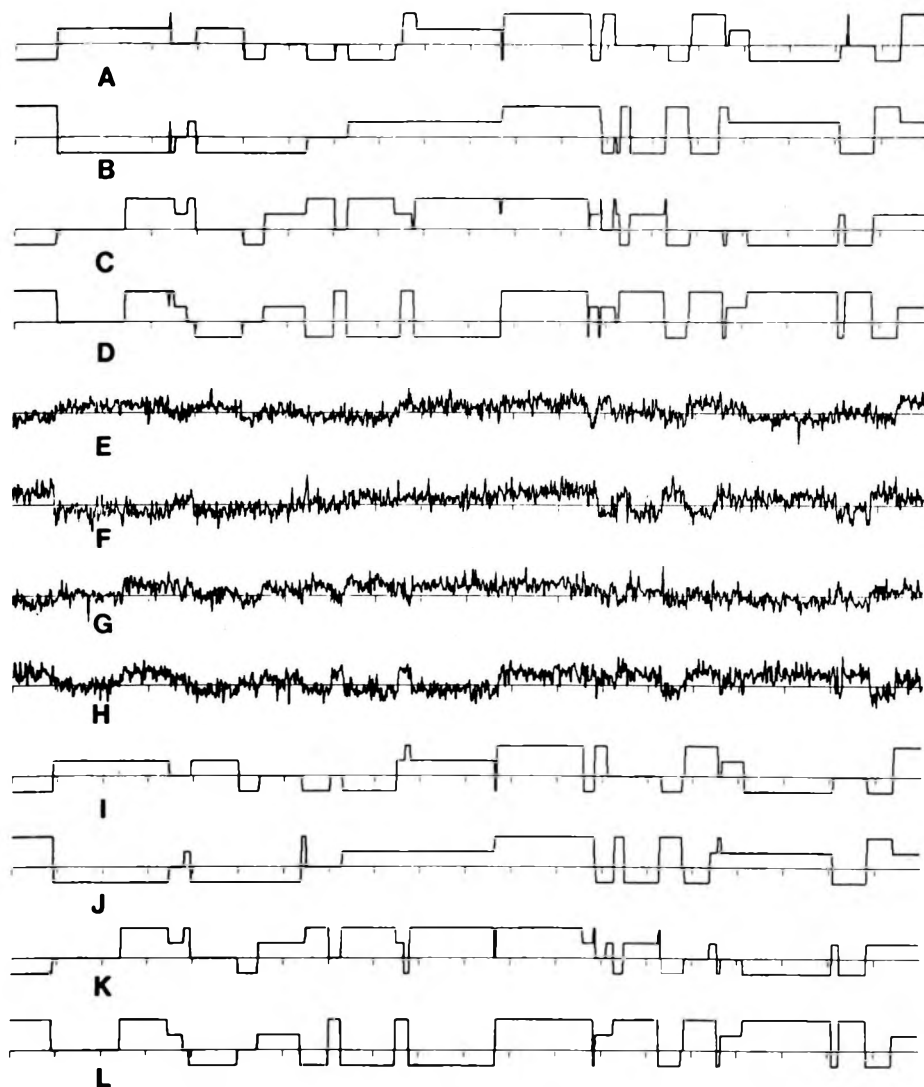


Fig. 3. A synthetic example including four channels

3. ábra. Szintetikus példa négy csatornával

Рис. 3. Синтетический пример с четырьмя каналами

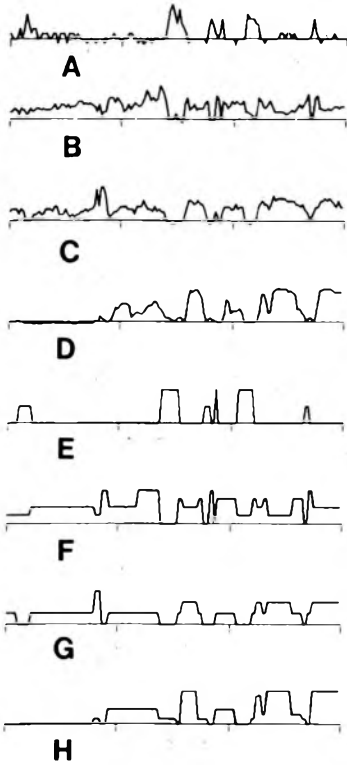


Fig. 4. Borehole Visonta F-389/0; step functions fitted to compensated γ - γ , γ -ray, neutron-neutron and resistivity logs

4. ábra. Visonta F-389/0 mélyfúrás; kompenzált γ - γ , természetes γ , neutron-neutron és ellenállás szelvényekhez illesztett lépcsős függvények

Рис. 4. Скважина F-389/0 Вишонта, ступенчатые зависимости совмещенные с кривыми ГГКП, ГК, ННК и КС

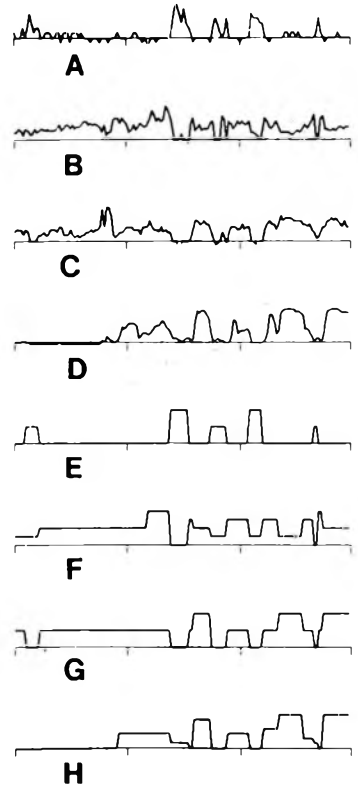


Fig. 5. Borehole Visonta F-389/0; step functions fitted to compensated γ - γ , γ -ray, neutron-neutron and resistivity logs

5. ábra. Visonta F-389/0 mélyfúrás; kompenzált γ - γ , természetes γ , neutron-neutron és ellenállás szelvényekhez illesztett lépcsős függvények

Рис. 5. Скважина F-389/0 Вишонта, ступенчатые зависимости совмещенные с кривыми ГГКП, ГК, ННК и КС

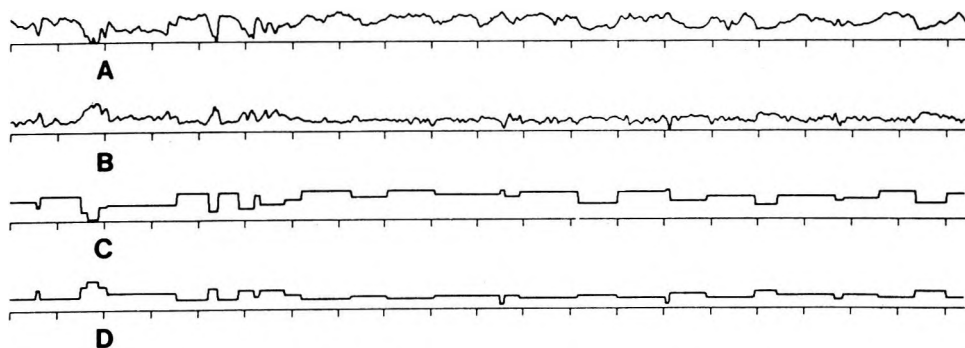


Fig. 6. Borehole AL-745; step functions fitted to density and acoustic logs

6. ábra. AL745 mélyfúrás; sűrűség és akusztikus terjedési idő szelvényhez illesztett lépcsős függvények

Рис. 6. Скважина AL-745, ступенчатые зависимости, совмещенные с кривыми плотности и интервального времени упругой волны

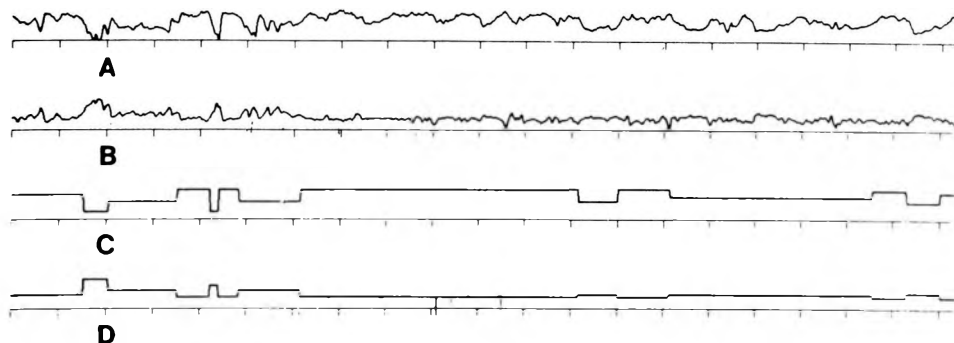


Fig. 7. Borehole AL-745; step functions fitted to density and acoustic logs

7. ábra. AL-745 mélyfúrás; sűrűség és akusztikus terjedési idő szelvényhez illesztett lépcsős függvények

Рис. 7. Скважина AL-745, ступенчатые зависимости, совмещенные с кривыми плотности и интервального времени упругой волны

6. Slowly varying layer parameters

In this part the restriction of homogeneity is omitted, allowing slow variations within the layers. The abrupt change of any physical parameter is still regarded as a layer boundary. It is useful to transform the measured data in

order to be able to handle them similarly to homogeneous layers, and to apply the previous methods. To achieve this aim the well log functions are factored into two terms; a slowly varying term, and a step function. The first will be described as a piecewise linear continuous function, while the second component will be the same step function already discussed. The information connected with the layering will be carried by the latter. If we remove the slowly varying component we get secondary experimental data fulfilling the original three requirements pertaining to homogeneous layers.

Our starting point is a two component Markov chain (see Section 3).

$$\{v_i\}_i^N = 0, \quad v_i = \begin{pmatrix} v_i^{(1)} \\ v_i^{(2)} \end{pmatrix} \quad (24)$$

The additive model of the experimental data can simply be constructed:

$$w_i = v_i^{(1)} + \sum_{j=0}^i v_j^{(2)} + n_i \quad (25)$$

$$i = 0, \dots, N$$

where w_i denotes the values of the well log to be factored. If we choose an appropriate value set for $\{v_i^{(1)}\}$ and $\{v_i^{(2)}\}$, the proper slowly varying and step function feature of the first two terms on the right hand side of Eq. (25) can be ensured. The third term is the same difference (noise) component as discussed earlier. The aim is to find the functions $\{v_i^{(1)}\}$ and $\{v_i^{(2)}\}$ matched optimally to the measured data set $\{w_i\}$. The principle chosen is again the maximum a posteriori probability. Equations 16-20 can be applied with minor changes.

Let us suppose that the $i-1$ -th sample is in the k -th, and the i -th sample is in the j -th state of the realization of the process described by Eq. (24). If the value belonging to the $i-1$ -th sample and k -th state of the slowly varying component is denoted by $S_{k,i-1}$, the cost of the difference is:

$$D_{k,j,i} = \frac{1}{2\sigma^2} (w_i - x_j^{(1)} - x_j^{(2)} - S_{k,i-1})^2 \quad (26)$$

where σ is the standard deviation parameter of the noise. The expression of the total cost now takes the form:

$$C_{j,i+1} = \min_k \{C_{k,i} + T_{kj} + D_{k,j,i+1}\} \quad (27)$$

where the term T_{kj} is the same as in Eq. (22). The recursive expression of $S_{j,i}$ is simply:

$$S_{j,i} = S_{k,i-1} + x_j^{(2)} \quad (28)$$

k is the index in this case which ensures the minimum in Eq. (27). So the whole problem has been reduced to the case discussed in the previous sections.

The result is shown on the synthetic example of Fig. 8. Curve *A* is a step function burdened by additive noise, curve *B* is a slowly varying piecewise linear

function. Curve *C* is the sum of the previous two functions and it is the input of the algorithm. The resultant functions *D* and *E* correspond to processes $\{v_i^{(1)}\}$ and $\{v_i^{(2)}\}$ respectively. The integral of function *E* would approach function *B*. *D* is practically the same as the noise-free component of function *A*. (The vertical scales of the curves are different because of the different normalization applied.)

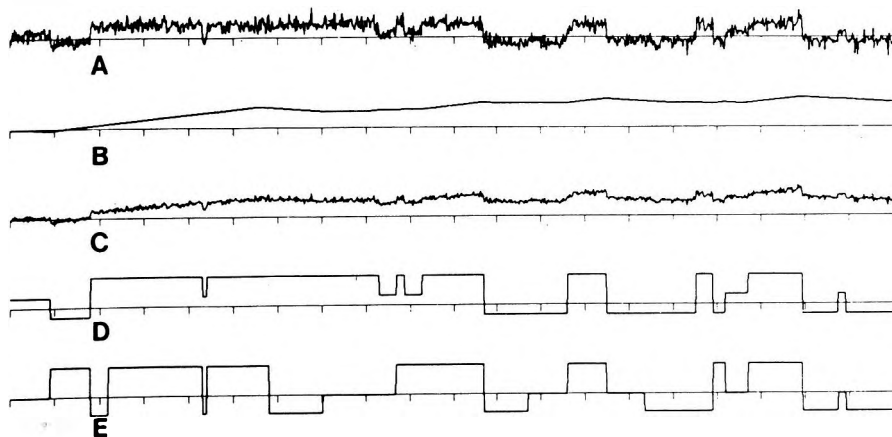


Fig. 8. Synthetic example containing inhomogeneous layers

8. ábra. Szintetikus példa inhomogén rétegekkel

Рис. 8. Синтетический пример с неоднородными пластами

7. Conclusions

A method is shown for constructing multilayered models based on arbitrary types of well logs measured in the same borehole. The layer boundaries were assumed to exhibit abrupt changes in one or more logs of the combination used. The problem was solved by optimum fitting of step functions with correlating discontinuities and controllable step lengths. The step functions were represented as realizations of multidimensional Markov chains. There is correspondence between the different states of the Markov chain and the possible lithological units, although this problem is beyond the scope of this paper. The distribution $\bar{\alpha}$ and the transition probability matrix *P* give a means of formulating and using a priori information for the interpreter, characterizing the particular logging tool combination and the geological conditions. In this way the algorithm is capable of discriminating between the interpretable and unacceptable cases of physical parameter combinations. Specifying the correspondence between the log combinations and lithology, and the distribution $\bar{\alpha}$ for the frequently used logging tool combinations is an important future research goal to support routine interpretation.

REFERENCES

- DOWDS J. P. 1969: Oil rocks: Information theory: Markov chains: Entropy. Quarterly of the Colorado School of Mines, **64**, 3, pp. 275-293
- FELLER W. 1978: An introduction to probability theory and its applications (in Hungarian). Vol. I. Műszaki Könyvkiadó, Budapest, 472. p.
- GODFREY R., MUIR F., ROCCA F. 1980: Modeling seismic impedance with Markov chains. Geophysics, **45**, 9, pp. 1351-1372
- HOLTZMAN F. M. 1971: Statistic models of interpretation (in Russian). Nauka, Moscow, 327 p.
- LAWLER E. L. 1982: Combinatorial Optimization: Networks and Matroids (in Hungarian). Műszaki Könyvkiadó, Budapest, 358 p.
- VERMES M. 1984: Computing interval velocities based on VSP data (in Hungarian). Magyar Geofizika, (in press)

RÉTEGSOR MEGHATÁROZÁS KAROTÁZS SZELVÉNYEK SZÁMÍTÓGÉPES FELDOLGOZÁSÁVAL

VERMES Máttyás

A dolgozatban egyetlen mélyfúrásban mért több karotázs szelvény alapján rétegmodell szerkesztéssel foglalkozunk. A feladatot olyan lépcsős függvények illesztésére vezetjük vissza, amelyek optimálisan illeszkednek a karotázs szelvényekhez, ugrási helyeik korrelálódhatnak, a lépcsők átlagos szélessége pedig szabályozható. A lépcsős függvényeket egy többdimenziós Markov-lánc realizációként állítjuk elő. A Markov-lánc lehetséges állapotaihoz az adott kutatási területen előforduló kőzetfajták hozzárendelhetők. Az átmenet-valószínűségi mátrix felépítése révén az algoritmussal olyan a priori információt közölhetünk, amely jellemző a fúrásban alkalmazott szonda-kombinációra és a geológiai viszonyokra. Ily módon a lépcsős függvények illesztésekor az algoritmus képes különbséget tenni a paraméterek fizikailag értelmes és értelmetlen kombinációi között. A dolgozat utolsó részében olyan rétegsorokat vizsgálunk, amelyeknél megengedjük a kőzetfizikai paraméterek lassú változását egyetlen rétegen belül is.

ОПРЕДЕЛЕНИЕ ГЕОЛОГИЧЕСКОГО РАЗРЕЗА С ПОМОЩЬЮ ОБРАБОТАННЫХ НА ЭВМ КАРОТАЖНЫХ ДАННЫХ

Маттяш ВЕРМЕШ

В работе описывается определение пластовой модели с помощью нескольких, полученных в одной скважине каротажных кривых. Задача состоит в получении таких ступенчатых зависимостей, которые оптимально аппроксимируют каротажные кривые, места скачков коррелируются, а средняя ширина ступеней регулируема. Ступенчатые зависимости определяются как реализации многомерной цепи Маркова. Представляется возможность совместить возможные состояния цепи Маркова с типами пород данной территории разведки. Строчные переходовероятностей матрицы дает возможность алгоритму содержать априорную информацию, характерную для геологических условий скважины и комбинации примененных зондов. При подгоне ступенчатых зависимостей алгоритм может различать имеющие или неимеющие физический смысл комбинации параметров.

В последней части работы исследуются и такие разрезы, в которых происходит медленное изменение физических свойств в пределах одного пласта.

PROBLEMS OF SEISMIC MIGRATION WITH ERRONEOUS VELOCITY

Andrzej KOSTECKI* and Anna PÓŁCHŁOPEK*

A thorough analysis is presented on how erroneous velocity affects the character of migration when several methods are applied ($k_x - \omega$ migration, $k_x - t$ migration and $x - t$ migration using the finite difference method). The observed change in seismic boundary dip angle and the associated dispersion phenomenon, both resulting from erroneous velocity, is explained and justified. Examples are provided of computer aided extrapolation of seismic fields for $\theta = 15^\circ, 30^\circ, 45^\circ$ seismic boundary dip angle in order to get a better insight into the migration phenomenon and to visualize the problem.

Keywords: seismic methods, migration, velocity, reflection, dispersion

1. Introduction

In seismic exploration practice it often occurs that seismic migration is carried out by means of wave equations which are charged with quite incorrect velocities. As a consequence seismic sections becomes poor in quality, particularly so far as the transformation of steeply dipping structures is concerned. The problem of utilizing erroneous velocities has been dealt with in the literature many times.

Among others DE VRIES and BERKHOUT [1984] have considered the possibility of velocity evaluation by means of field focusing as an ideal zero-phase pattern whereas ROCCA and SALVADOR [1982] proposed the method of migrated data correction by residual migration with different velocities. Moreover the aspect of errors of field displacement as a result of applied velocity was considered by HUBRAL [1977], and by LARNER et al. [1981]. The aim of the present article is to evaluate the influence of incorrect velocity on the quality of seismic migration transformation.

2. Theoretical considerations and modelling of wave field extrapolation

Let us assume that in a homogeneous medium of velocity v with a reflector dipping at angle θ to the axis x , the equation $z = z_0 - x \tan \theta$ is the phase surface of a plane wave moving towards the surface $z=0$ on which the wave field is recorded:

*Institute of Oil and Gas, Cracow, ul. Lubicz 25a, Poland
Manuscript received: 4. June, 1985

$$F(x, 0, t) = \delta\left(t - t_0 + \frac{2x \sin \theta}{v}\right) \quad (1)$$

where δ is the Dirac function and the argument

$$t = t_0 - \frac{2x \sin \theta}{v} \quad (2)$$

presents the time distance curve of the seismic wave field measured by the CDP method. Let us apply to the surface field $F(x, 0, t)$ k_x - ω migration in the domain of wave numbers k_x and frequency ω . Let us calculate the spectral function $F(k_x, 0, \omega)$ from the inverse Fourier transform:

$$\begin{aligned} \bar{F}(k_x, 0, \omega) &= \int_{-\infty}^{+\infty} e^{-ik_x x} \int_0^{\infty} \delta\left(t - t_0 + \frac{2x \sin \theta}{v}\right) e^{-i\omega t} dt = \\ &= 2\pi e^{-i\omega t_0} \delta\left(k_x - \frac{2\omega \sin \theta}{v}\right) \end{aligned} \quad (3)$$

In depth z , at the correct velocity v

$$F(k_x, z, \omega) = F(k_x, 0, \omega) e^{ik_z z} \quad (4)$$

where

$$k_z = (k^2 - k_x^2)^{\frac{1}{2}} \quad (5)$$

is the vertical component of the wave number, and $k = 2\omega/v$ is the wave number module. Let us assume, however, that for the wave field extrapolation in the lower halfspace the velocity $v_1 \neq v$ has been used. In such a case, at depth z we obtain:

$$\bar{F}(k_x, z, \omega) = 2\pi e^{-i\omega t_0} \delta\left(k_x - \frac{2\omega \sin \theta}{v}\right) e^{ik_{1z} z} \quad (6)$$

where

$$\begin{aligned} k_{1z} &= (k_1^2 - k_x^2)^{\frac{1}{2}} \\ k_1 &= \frac{2\omega}{v_1} \end{aligned} \quad (7)$$

The migrated wave field is given by the inequality $F(x, z, 0) \neq 0$ when

$$k_x = \frac{2\omega \sin \theta}{v} \quad (8)$$

which makes it possible to compute the integral in Eq. (6)

$$\begin{aligned}
 F(x, z, t) &= \frac{1}{4\pi^2} \iint_{-\infty}^{+\infty} \bar{F}(k_x, 0, \omega) e^{i(\omega t + k_x x + k_{1z} z)} d\omega dk_x = \\
 &= \delta \left[t - t_0 + \frac{2x \sin \theta}{v} + \frac{2z}{v_1} \left(1 - \frac{v_1^2}{v^2} \sin^2 \theta \right)^{\frac{1}{2}} \right]
 \end{aligned} \quad (9)$$

Setting

$$\frac{v_1^2}{v^2} \sin^2 \theta = \sin^2 \theta_1, \quad (10)$$

then for $t=0$

$$F(x, z, 0) = \delta \left(-t_0 + \frac{2x \sin \theta_1}{v_1} + \frac{2z}{v_1} \cos \theta_1 \right) \quad (11)$$

from which it turns out that the migrated field $F(x, z, 0)$ is different from zero when

$$z = z_{01} - x \tan \theta_1 \quad (12)$$

where

$$z_{01} = \frac{v_1 t_0}{2 \cos \theta_1}$$

which means that the migrated field $F(x, z, 0)$ is transformed on the horizon dipping at angle θ_1 to axis x .

It is easy to notice that relation (10) — stating the connection between the sine of the real dip angle θ , the real velocity v and the velocity assumed for the migration velocity v_1 constituted only to denote the value $v_1^2/v^2 \cdot \sin^2 \theta$ — can be interpreted as a directional characteristic of the derivative

$$\frac{dt}{dx} = -\frac{2 \sin \theta_1}{v_1} = -\frac{2 \sin \theta}{v} \quad (13)$$

of the CDP travel-time curve recorded on the surface $z=0$. Therefore the migration process with the assumption of the erroneous velocity v_1 can be treated as the extrapolation of the wave field recorded at surface $z=0$ originating from the reflection boundary dipping at angle θ_1 and propagating with velocity v_1 . One can accept this kind of interpretation if one takes the inverse case to be the extrapolation of recorded field at the time $t=0$ at the boundary dipping at angle θ of the equation $z = z_0 - x \tan \theta$ towards the surface $z=0$. If we start from the wave equation

$$F_{xx} + F_{\tau\tau} \frac{4}{v^2} - \frac{4}{v^2} F_{\tau\tau} = 0 \quad (14)$$

where

$$\tau = \frac{2z}{v}$$

and apply the Fourier transform

$$F(x, \tau, t) = \frac{1}{4\pi^2} \iint_{-\infty}^{+\infty} \bar{F}(k_x, k_\tau, t) e^{i(k_x x + k_\tau \tau)} dk_x dk_\tau \quad (15)$$

we obtain, for the subintegral function $F(k_x, k_\tau, t)$, the equation

$$F(k_x, k_\tau, t) = F(k_x, k_\tau, 0) e^{i\omega t} \quad (16)$$

where

$$\omega = \frac{v}{2} \left(k_x^2 + k_\tau^2 \frac{4}{v^2} \right)^{\frac{1}{2}} \quad (17)$$

If we assume that there exists a wave field at the boundary

$$F(x, \tau, 0) = \delta \left(\tau - \tau_0 + \frac{2x \tan \theta}{v} \right) \quad (18)$$

we obtain from the Fourier transform

$$\begin{aligned} \bar{F}(k_x, k_\tau, 0) &= \int_{-\infty}^{+\infty} e^{-ik_x x} dx \int_0^{\infty} \delta \left(\tau - \tau_0 + \frac{2x \tan \theta}{v} \right) e^{-ik_\tau \tau} d\tau = \\ &= 2\pi e^{-ik_\tau \tau_0} \delta \left(k_x - \frac{2k_\tau \tan \theta}{v} \right) \end{aligned} \quad (19)$$

Thence by means of Eq. (16), we get

$$\begin{aligned} F(x, \tau, t) &= \frac{1}{2\pi} \int_{-\infty}^{+\infty} e^{ik_\tau(\tau - \tau_0)} dk_\tau \int_{-\infty}^{+\infty} \delta \left(k_x - \frac{2k_\tau \tan \theta}{v} \right) \cdot \\ &\cdot e^{i \left[k_x x + \frac{vt}{2} \left(k_x^2 + k_\tau^2 \frac{4}{v^2} \right) \right]} dk_x = \delta \left(\tau_0 - \tau - \frac{2x \tan \theta}{v} - \frac{t}{\cos \theta} \right) \end{aligned} \quad (20)$$

From Eq. (20) it is evident that $F(x, 0, t) \neq 0$ when

$$t = t_0 - \frac{2x \sin \theta}{v} \quad (21)$$

where $t_0 = \tau_0 \cos \theta$ is the time constant. In the case of wave field modelling, applying the velocity v_1 and the same input field

$$F(x, \tau, 0) = \delta \left(\tau - \tau_0 + \frac{2x \tan \theta}{v} \right),$$

in Eq. (20)

$$e^{i \frac{v t}{2} \left(k_x^2 + k_\tau^2 \frac{4}{v^2} \right)^{\frac{1}{2}}}$$

is substituted for the function

$$e^{i \frac{v_1 t}{2} \left(k_x^2 + k_\tau^2 \frac{4}{v_1^2} \right)^{\frac{1}{2}}}$$

Using the condition defined by Eq. (19)

$$k_x = \frac{2k_\tau \tan \theta}{v} \tag{22}$$

we obtain

$$e^{i \frac{v_1 t}{2} \left(k_x^2 + k_\tau^2 \frac{4}{v_1^2} \right)^{\frac{1}{2}}} = e^{i k_\tau t \left[1 + \frac{v_1^2}{v^2} \tan^2 \theta \right]^{\frac{1}{2}}} \tag{23}$$

If we take

$$\frac{v_1^2}{v^2} \tan^2 \theta = \tan^2 \theta_1 \tag{24}$$

we obtain

$$e^{i k_\tau t \left(1 + \frac{v_1^2}{v^2} \tan^2 \theta \right)^{\frac{1}{2}}} = e^{i \frac{k_\tau t}{\cos \theta_1}} \tag{25}$$

Applying this expression to Eq. (20) we obtain

$$F(x, 0, t) = \delta \left(\tau_0 - \frac{2x \tan \theta_1}{v_1} - \frac{t}{\cos \theta_1} \right) \tag{26}$$

so

$$t = t_{01} - \frac{2x \sin \theta_1}{v_1} \tag{27}$$

where

$$t_{01} = \tau_0 \cos \theta_1$$

Therefore modelling the wave field of the input characteristics

$$\frac{d\tau}{dx} = -\frac{2}{v} \tan \theta = -\frac{2}{v_1} \tan \theta_1 \tag{28}$$

with erroneous velocity v_1 we obtain the wave field of the directional characteristics defined by the relation

$$\frac{dt}{dx} = -\frac{2}{v_1} \sin \theta_1 \quad (29)$$

The above mentioned considerations do not, however, describe the change of dynamic features which can accompany the migration and seismic modelling processes.

In order to explain the phenomenon, a computer simulation has been carried out for the model of reflected wave fields from monoclinical seismic boundaries enclosing with the axis x the angles 15° , 30° and 45° . The model was calculated using the method described by Eqs. (15–16), with $\Delta t = 0.004$ s and velocity $v = 2000$ m/s. An example for the dip angle $\theta = 45^\circ$ is presented in Fig. 1. For the same model, $k_x - \omega$ migration was carried out (Fig. 2), and the migra-

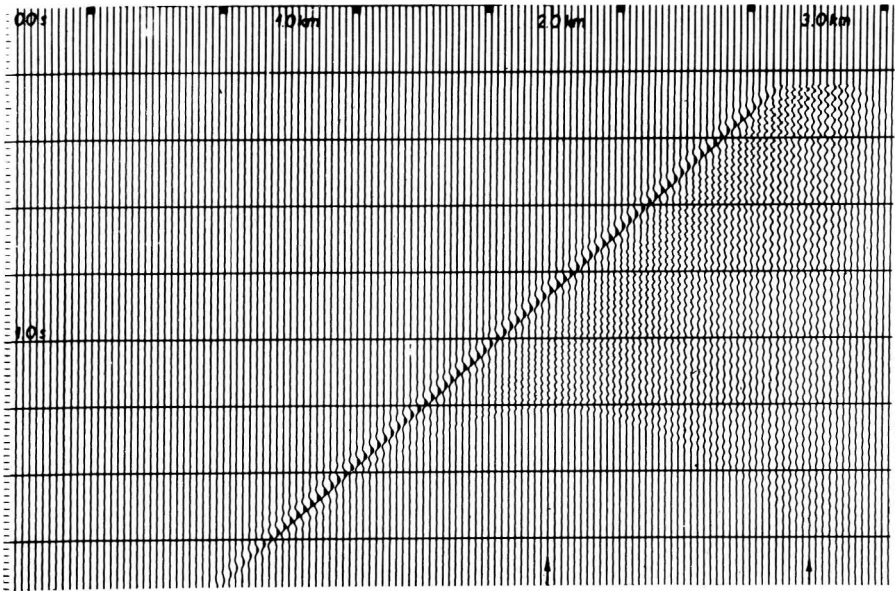


Fig. 1. Unmigrated synthetic time section of reflector inclined at 45° . $\Delta x = 25$ m, $\Delta t = 0.004$ s

1. ábra. 45° -os dőlésű reflektáló felület migrálatlan szintetikus időszelvénye, $\Delta x = 25$ m, $\Delta t = 0.004$ s

Рис. 1. Синтетический временной разрез без миграции отражающей поверхности с наклоном 45° . $\Delta x = 25$ м, $\Delta t = 0.004$ сек

tion in the domain of wave numbers and time ($k_x - t$ migration) by means of the three-coefficient equation method [STOLT 1978] is presented in Fig. 3. Both migrated sections direct attention to the high quality of representation of the

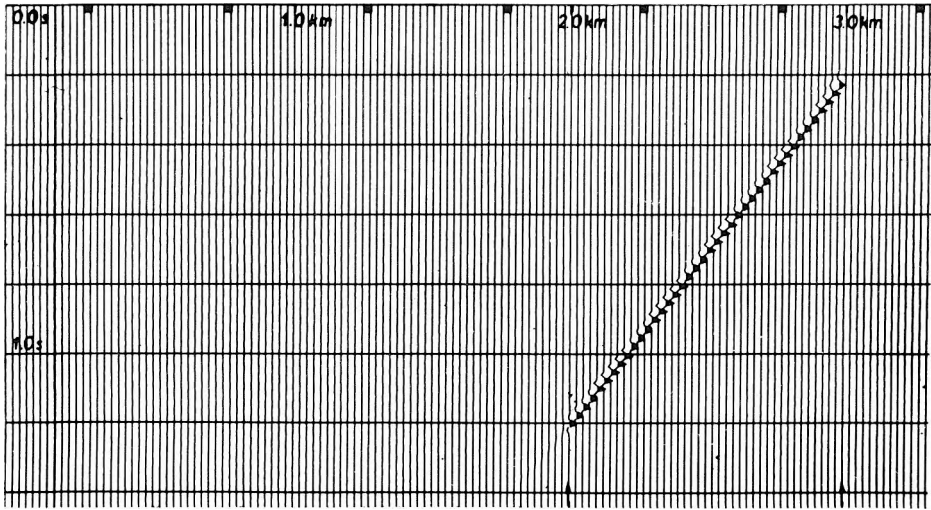


Fig. 2. Time section after $(k_x - \omega)$ migration of the synthetic section shown in Fig. 1 using $\Delta x = 25$ m, $\Delta t = 0.004$ s, $\Delta \tau = 0.004$ s, $v = 2000$ m/s

2. ábra. Az 1. ábrán látható szintetikus időszelvény $k_x - \omega$ migráció után, $\Delta x = 25$ m, $\Delta t = 0.004$ s, $\Delta \tau = 0.004$ s, $v = 2000$ m/s sebesség mellett

Рис. 2. Временной разрез рис. 1. после миграции $k_x - \omega$, $\Delta x = 25$ м, $\Delta t = 0.004$ сек, $\Delta \tau = 0.004$ сек, $v = 2000$ м/сек

boundary in the given x interval. The time sections in Figs. 4 and 5 migrated by the method $k_x - \omega$ and the method $k_x - t$ applying the erroneous velocity $v_1 = 2,400$ m/s are characterized by the presence of a band of waves beside the main phase. The main phase with a higher amplitude represents the dip angle $\theta_1 = 58^\circ.05$ in accordance with Eq. (10) (Fig. 4). This phenomenon can be expressed by an essential distortion of the seismic impulse form and of the amplitude spectra (Figs. 6 and 7). Together with the boundary dip angle ($\theta = 30^\circ$) one can detect a decrease of peripheral phases accompanying the main phase representing the false dip angle both in the $k_x - \omega$ migration (Fig. 8) and in the $k_x - t$ migration (Fig. 9). A similar phenomenon accompanies the decrease of velocity error used in the migration process ($k_x - \omega$, $v_1 = 2200$ m/s) (Fig. 10). The phenomenon of peripheral phase decay with decrease of the dip angle can distinctly be seen in Figs. 11 and 12 where, in a similar quality of representation, the boundary dipping at an angle of 15° with the false velocity $v_1 = 2,400$ m/s after $k_x - \omega$ and $k_x - t$ migration is presented. Although the observed wave dispersion is not a rare phenomenon in the wave extrapolation process and it accompanies those migrations which apply the simplified wave equation and approximate calculus operators [BERKHOUT 1980, CLAERBOUT 1976], in the above mentioned cases one cannot attribute dispersion to the approximative character of the solutions (both at $k_x - t$ migration and $x - t$

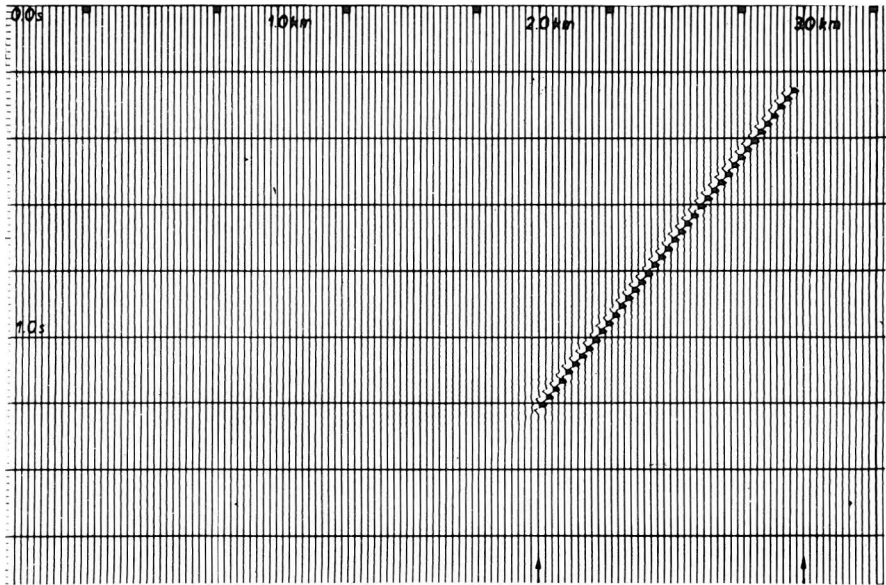
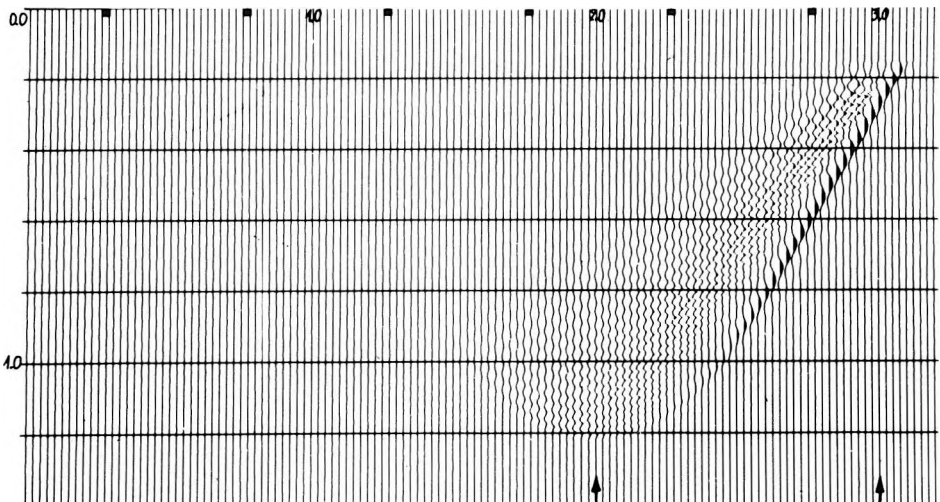


Fig. 3. Time section after $(k_x - t)$ migration of the synthetic section shown in Fig. 1 using $\Delta x = 25$ m, $\Delta t = 0.004$ s, $\Delta z = 40$ m, $v = 2000$ m/s

3. ábra. Az 1. ábrán látható szintetikus szelvény $(k_x - t)$ migráció után. $\Delta x = 25$ m, $\Delta t = 0.004$ s, $\Delta z = 40$ m, $v = 2000$ m/s mellett

Рис. 3. Временной разрез рис. 1. после миграции $(k_x - t)$, $\Delta x = 25$ м, $\Delta t = 0.004$ сек, $\Delta z = 40$ м, $v = 2000$ м/сек



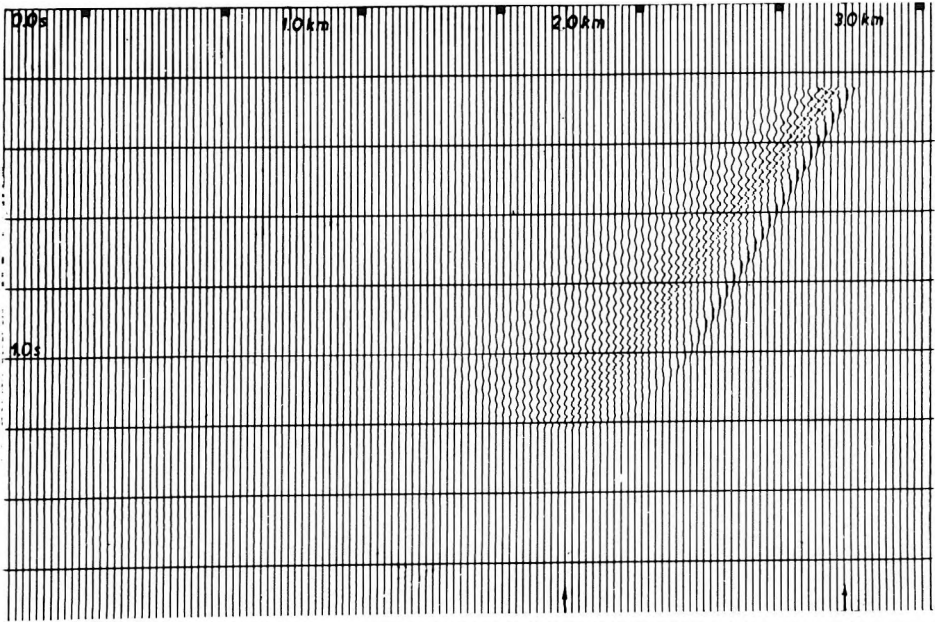


Fig. 5. Time section after $(k_x - t)$ migration of the synthetic section shown in Fig. 1 using $\Delta x = 25$ m, $\Delta t = 0.004$ s, $\Delta z = 40$ m, $v = 2400$ m/s

5. ábra. Az 1. ábrán látható szintetikus szelvény $(k_x - t)$ migráció után, $\Delta x = 25$ m, $\Delta t = 0.004$ s, $\Delta z = 40$ m, $v = 2400$ m/s mellett

Рис. 5. Временной разрез рис. 1. после миграции $(k_x - t)$, $\Delta x = 25$ м, $\Delta t = 0.004$ сек, $\Delta z = 40$ м, $v = 2000$ м/сек



Fig. 4. Time section after $(k_x - \omega)$ migration of the synthetic section shown in Fig. 1 using $\Delta x = 25$ m, $\Delta t = 0.004$ s, $\Delta \tau = 0.004$ s, $v = 2400$ m/s



4. ábra. Az 1. ábrán látható szintetikus szelvény $(k_x - \omega)$ migráció után, $\Delta x = 25$ m, $\Delta t = 0.004$ s, $\Delta \tau = 0.004$ s, $v = 2400$ m/s mellett



Рис. 4. Временной разрез рис. 1. после миграции $(k_x - \omega)$, $\Delta x = 25$ м, $\Delta t = 0.004$ сек, $\Delta \tau = 0.004$ сек, $v = 2400$ м/сек

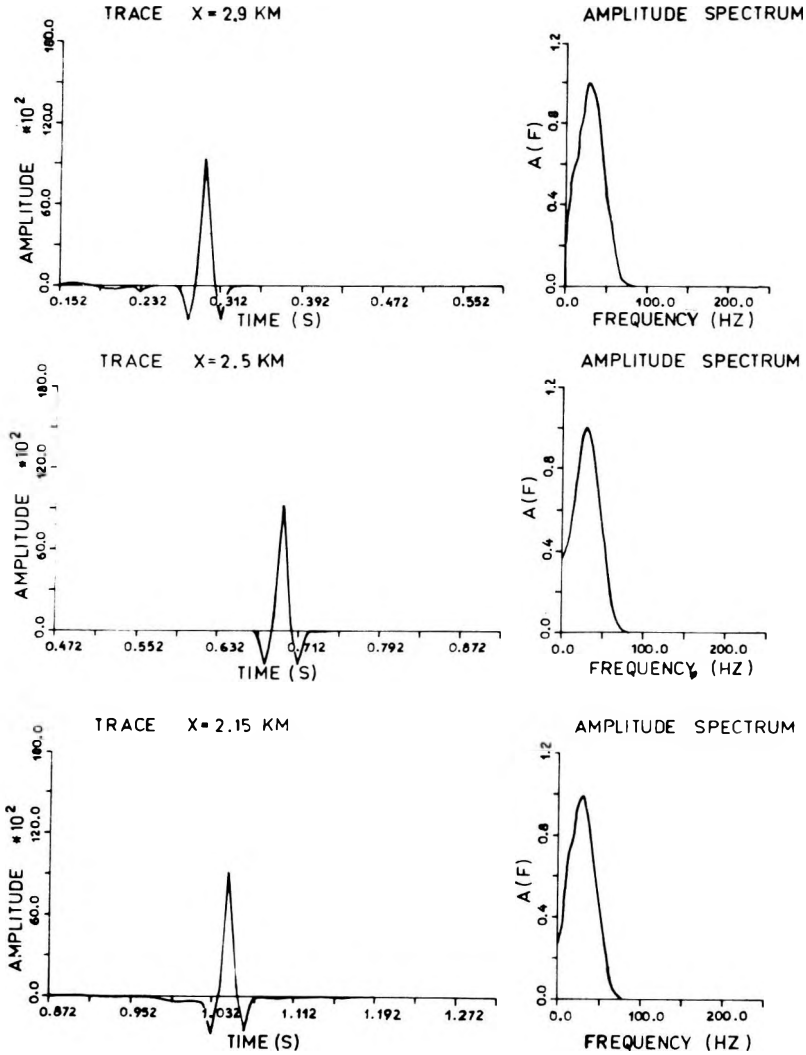


Fig. 6. The signals and their amplitude spectra after $(k_x - \omega)$ migration of the section shown in Fig. 1 using velocity $v = 2000$ m/s

6. ábra. Az 1. ábrán látható szeizmikus szelvény jelalakjai és amplitúdó spektrumai $(k_x - \omega)$ migráció után $v = 2000$ m/s mellett

Рис. 6. Сигналы и амплитудные спектры сейсмического разреза рис. 1. после миграции $(k_x - \omega)$ при $v = 2000$ м/сек

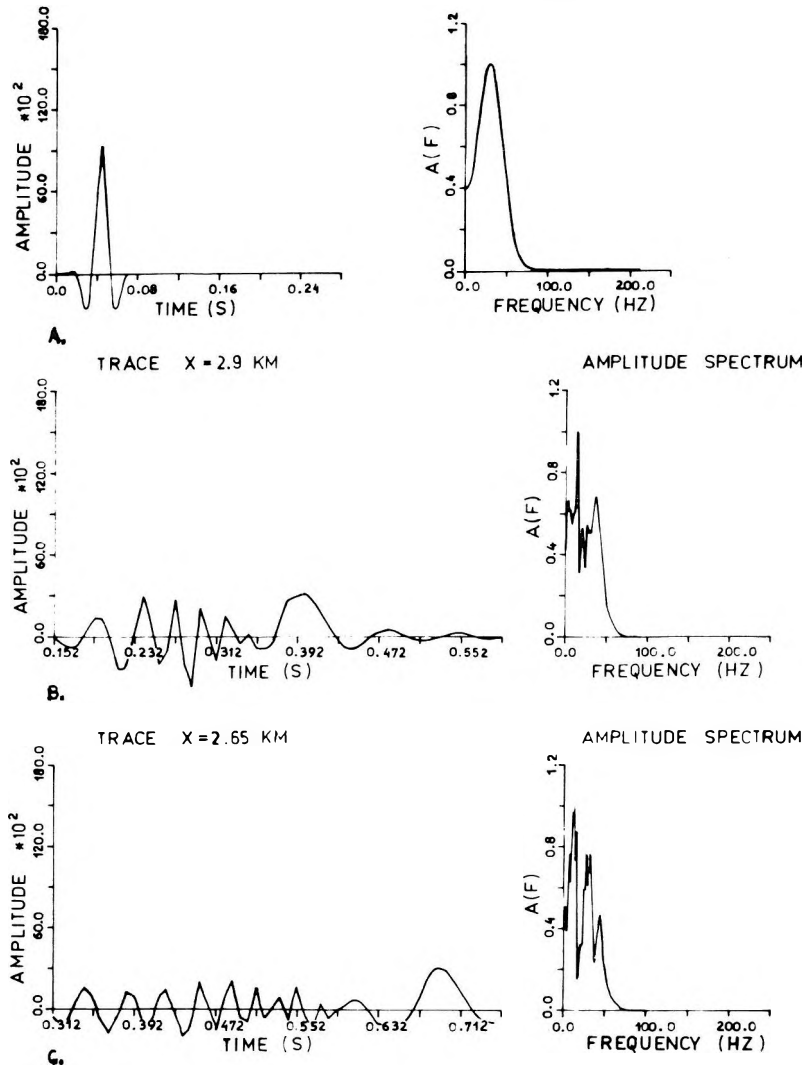


Fig. 7. A) Input signal and its amplitude spectrum. B), C) Signals and their amplitude spectra after $(k_x - \omega)$ migration of the section shown in Fig. 1 using velocity $v = 2400$ m/s

7. ábra. A) Bemenő jel és a hozzá tartozó amplitúdó spektrum. B), C) Az 1. ábrán látható szelvény jelalakjai és amplitúdó spektrumai $(k_x - \omega)$ migráció után, $v = 2400$ m/s sebesség mellett

Рис. 7. А) Входной сигнал и спектр амплитуды. В), С) сигналы и амплитудные спектры разреза рис. 1. после миграции $(k_x - \omega)$ при скорости $v = 2400$ м/сек

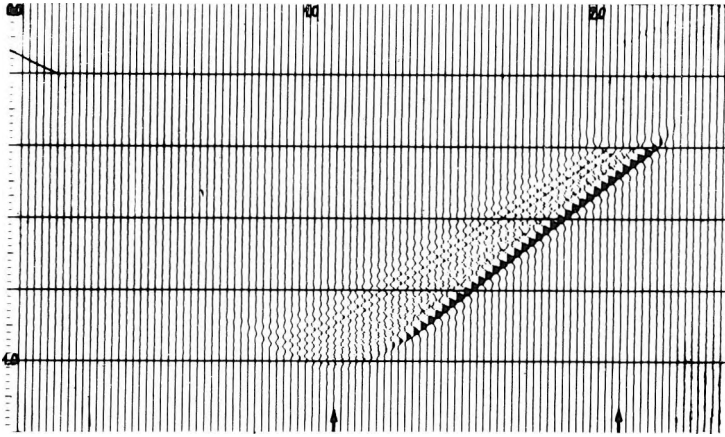


Fig. 8. Time section after $(k_x - \omega)$ migration of reflector inclined at 30 degrees using $v = 2400$ m/s, $\Delta x = 25$ m, $\Delta t = 0.004$ s, $\Delta \tau = 0.004$ s

8. ábra. 30°-os dőlésű reflektáló felület időszelvénye $(k_x - \omega)$ migráció után, $v = 2400$ m/s, $\Delta x = 25$ m, $\Delta t = 0.004$ s, $\Delta \tau = 0.004$ s mellett

Рис. 8. Временной разрез отражающей поверхности с наклоном 30° после миграции $(k_x - \omega)$ при $v = 2400$ м/сек, $\Delta x = 25$ м, $\Delta t = 0,004$ сек, $\Delta \tau = 0,004$ сек

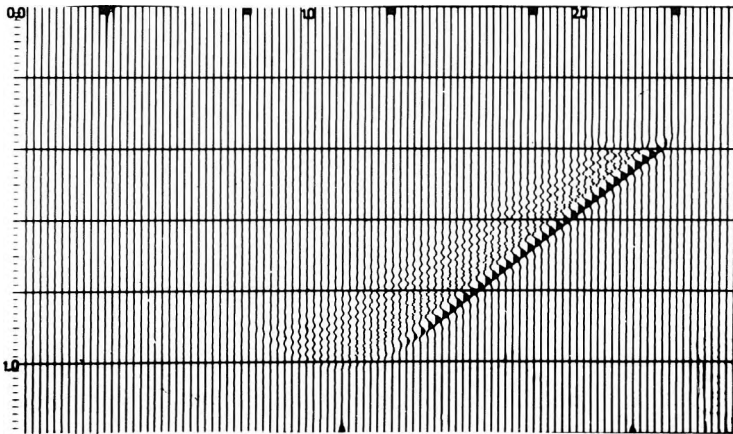


Fig. 9. Time section after $(k_x - t)$ migration of the reflector directed at 30 degrees using $v = 2400$ m/s, $\Delta x = 25$ m, $\Delta t = 0,004$ s, $\Delta z = 40$ m

9. ábra. 30°-os dőlésű reflektáló felület időszelvénye $(k_x - t)$ migráció után, $v = 2400$ m/s, $\Delta x = 25$ m, $\Delta t = 0,004$ s, $\Delta z = 40$ m mellett

Рис. 9. Временной разрез отражающей поверхности с наклоном 30° после миграции $(k_x - t)$ при $v = 2400$ м/сек, $\Delta x = 25$ м, $\Delta t = 0,004$ сек, $\Delta z = 40$ м

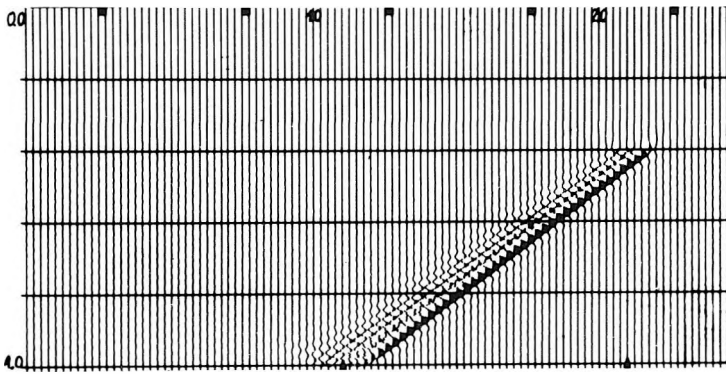


Fig. 10. Time section after $(k_x - \omega)$ migration of the reflector inclined at 30 degrees using $v = 2200$ m/s, $\Delta x = 25$ m, $\Delta t = 0.004$ s, $\Delta \tau = 0.004$ s

10. ábra. 30°-os dőlésű reflektáló felület időszelvénye $(k_x - \omega)$ migráció után, $v = 2200$ m/s, $\Delta x = 25$ m, $\Delta t = 0.004$ s, $\Delta \tau = 0.004$ s mellett

Рис. 10. Временной разрез отражающей поверхности с наклоном 30° после миграции $(k_x - \omega)$ при $v = 2200$ м/сек, $\Delta x = 25$ м, $\Delta t = 0.004$ сек, $\Delta \tau = 0.004$ сек

migration). This statement is supported by lack of dispersion in the case of the $k_x - t$ migration at the boundary dip angle $\theta = 45^\circ$ (Fig. 13) when applying a correct velocity, and with simultaneous occurrence of this phenomenon for smaller dip angles $\theta = 30^\circ$ and $\theta = 15^\circ$ with erroneous velocity v_1 and the occurrence of dispersion for the $k_x - \omega$ migration applying erroneous velocity. It is worth while to emphasize that the field extrapolation was carried out at relatively small extrapolating intervals: $\Delta t = \Delta \tau = 0.004$ s, $\Delta z = 40$ m which ensured stability of extrapolation by means of finite difference methods ($x - t$ and $k_x - t$ migrations). One has also to note that the utilization of erroneous velocity is not a source of aliasing errors.

In fact

$$\omega \leq \frac{\pi}{\Delta t'}$$

where

$$\Delta t' = 2\Delta x \frac{\sin \theta}{v}$$

remains unchanged when relation (13) is satisfied. From the above mentioned considerations and model experiments it is evident that migration with erroneous velocity is accompanied by the dispersion phenomenon. As for $k_x - \omega$ migration one can notice that due to the application of erroneous velocity the extrapolation operator is changed

$$\bar{F}(k_x, z, \omega) = \bar{F}(k_x, 0, \omega)e^{i(k_z + \Delta k_z)Z} \quad (30)$$

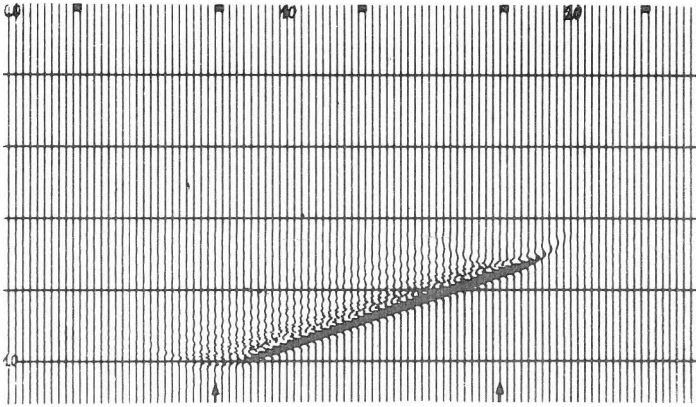


Fig. 11. Time section after $(k_x - \omega)$ migration of the reflector directed at 15 degrees using $v = 2400$ m/s, $\Delta x = 25$ m, $\Delta t = 0.004$ s, $\Delta \tau = 0.004$ s

11. ábra. 15°-os dőlésű reflektáló felület időszelvénye $(k_x - \omega)$ migráció után, $v = 2400$ m/s, $\Delta x = 25$ m, $\Delta t = 0.004$ s, $\Delta \tau = 0.004$ s mellett

Рис. 11. Временной разрез отражающей поверхности с наклоном 15° после миграции $(k_x - \omega)$ при $v = 2400$ м/сек, $\Delta x = 25$ м, $\Delta t = 0.004$ сек, $\Delta \tau = 0.004$ сек

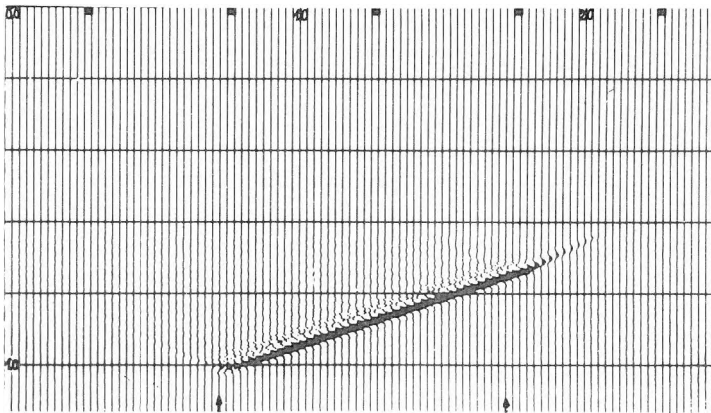


Fig. 12. Time section after $(k_x - t)$ migration of the reflector directed at 15 degrees using $v = 2400$ m/s, $\Delta x = 25$ m, $\Delta t = 0.004$ s, $\Delta z = 40$ m

12. ábra. 15°-os dőlésű reflektáló felület időszelvénye $(k_x - t)$ migráció után, $v = 2400$ m/s, $\Delta x = 25$ m, $\Delta t = 0.004$ s, $\Delta z = 40$ m mellett

Рис. 12. Временной разрез отражающей поверхности с наклоном 15° после миграции $(k_x - t)$ при $v = 2400$ м/сек $\Delta x = 25$ м, $\Delta t = 0.004$ сек, $\Delta z = 40$ м

where the increase of the vertical component of the wave number is given by

$$\Delta k_z = k_{1z} - k_z = k_1 \cos \theta_1 - k \cos \theta = k \left(\frac{v}{v_1} \cos \theta_1 - \cos \theta \right) = k \Delta \cos \theta, \quad (31)$$

In this case

$$(k_z + \Delta k_z)z = k(\cos \theta + \Delta \cos \theta)z = \omega \tau (\cos \theta + \Delta \cos \theta) = \omega \cos \theta (\tau + \Delta \tau) \quad (32)$$

where

$$\Delta \tau = \frac{\Delta \cos \theta}{\cos \theta} \tau \quad (33)$$

Thus, the application of erroneous velocity causes time displacement on the migrated section increasing with time and proportional to the value of the relative increase of the cosine of the boundary dip angle (according to definition $\Delta \cos \theta$).

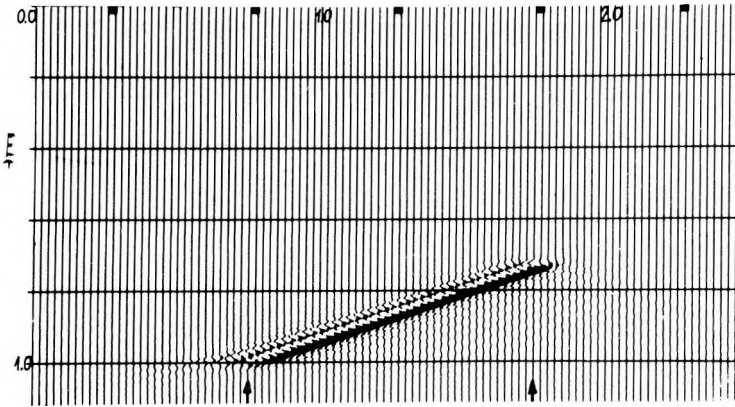


Fig. 13. Time section after $(x-t)$ migration of the reflector directed at 15 degrees using $v = 2400$ m/s, $\Delta x = 25$ m, $\Delta t = 0.004$ s, $\Delta z = 40$ m

13. ábra. 15°-os dőlésű reflektáló felület időszelvénye $(x-t)$ migráció után $v = 2400$ m/s, $\Delta x = 25$ m, $\Delta t = 0,004$ s, $\Delta z = 40$ m mellett

Рис. 13. Временной разрез отражающей поверхности с наклоном 15° после миграции $(x-t)$ при $v = 2400$ м/сек $\Delta x = 25$ м, $\Delta t = 0,004$ сек, $\Delta z = 40$ м

In order to test the possibilities of dispersion elimination from the migrated time sections an experiment was carried out by means of extrapolating the migrated field towards the test section by modelling. In order to define the velocity v_2 in relation to the extrapolation of a migrated section in the directional characteristics $\tan \theta_1/v_1$ let us transform Eq. (28)

$$\frac{\tan \theta_1}{v_1} = \frac{\tan \theta_2}{v_2} \quad (34)$$

and state the condition

$$\frac{\sin \theta_2}{v_2} = \frac{\tan \theta}{v} \quad (35)$$

which means identity of the correct and migrated section by means of the correct velocity v .

From Eqs. (34) and (35) and Eq. (13) we obtain

$$v_2 = (v_1^2 - v^2)^{\frac{1}{2}} \quad (36)$$

when $v_1 > v$.

It should be noted that in the case of residual migration with velocity v_2 (instead of modelling), i.e. when $v_1 < v$, in Eq. (36) transposition of velocities v_1 and v occurs. Correction of migrated sections by means of residual field extrapolation (modelling or migration) is an interesting proposition for the accuracy correction of migration [ROCCA, SALVADOR 1982, ROTHMAN et. al. 1985]. Using velocity v_2 in accordance with Eq. (36), modelling of the section migrated with velocity $v_1 = 2400$ m/s (Fig. 4) was carried out. The section migrated in the two phases shown in Fig. 14 hardly differs from the migrates section with the

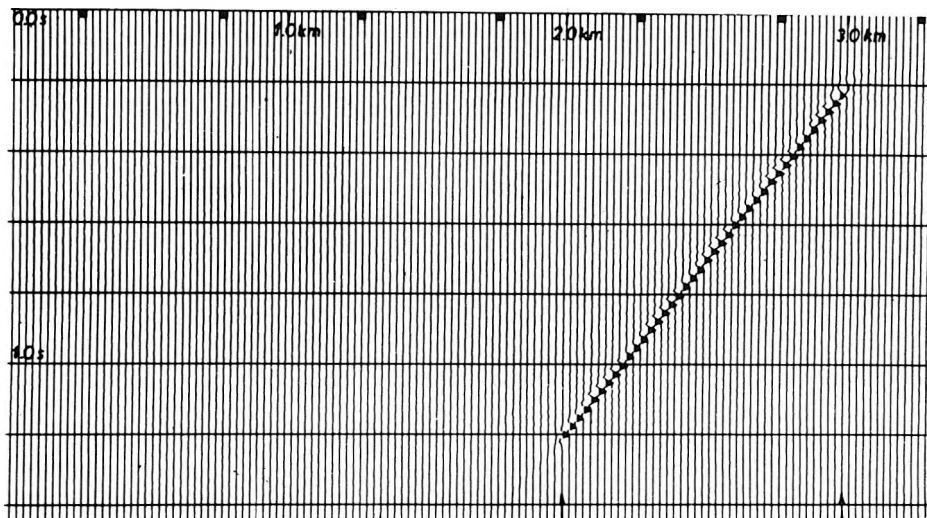


Fig. 14. Time section after residual migration of the section shown in Fig. 4 using velocity $v_2 = 1327$ m/s, $\Delta x = 25$ m, $\Delta t = 0.004$ s

14. ábra. Időszelvény, melyet a 4. ábrán látható szelvényen $v_2 = 1327$ m/s sebességgel végrehajtott reziduális migráció eredményeként kaptunk. $\Delta x = 25$ m, $\Delta t = 0.004$ s mellett

Рис. 14. Временной разрез, полученный в результате остаточной миграции разреза рис. 4. при $v_2 = 1327$ м/сек, $\Delta x = 25$ м, $\Delta t = 0,004$ сек

proper velocity (Fig. 2). The dispersion phenomenon has disappeared and the boundary has been represented at the angle 45° , i.e. at the real incident angle. Therefore the above mentioned experiment proved that the erroneous velocity applied in the migration process is the source of dispersional disturbances which can be eliminated in the residual migration process.

3. Conclusions

1. The application of erroneous velocity in the migration process causes seismic boundaries dipping at improper inclination angles to appear on the profiles. The dip angle θ if erroneous velocity is applied is defined by relation (10).
2. The application of erroneous velocity in the migration process is accompanied by an increase in the dispersion phenomenon together with increasing dips and increasing error of the applied velocity.
3. A field extrapolation process in two phases or the so called residual migration removes the dispersion phenomenon and represents the real seismic boundary dip angle.

REFERENCES

- BERKHOUT A. J. 1982: *Seismic Migration*. Amsterdam, Elsevier 351 p.
- CLAERBOUT J. F. 1976. *Fundamentals of Geophysical Data Processing*. New York, McGraw Hill, 274 p.
- DE VRIES D. B., BERKHOUT A. J. 1984: Influence of velocity errors on the focusing aspects of migration. *Geophysical Prospecting* **32**, 4, pp. 629–648
- HUBRAL P. 1977: Time migration — some ray theoretical aspects. *Geophysical Prospecting* **25**, 4, pp. 738–745
- LARNER K. L., HATTON L., GIBSON B. S., HSU I. 1981: Depth migration of imaged time sections. *Geophysics* **46**, 5, pp. 734–750
- ROTHMAN D. H., LEVIN S. A., ROCCA F. 1985: Residual migration: Application and limitations. *Geophysics* **50**, 1, pp. 110–126
- ROCCA F., SALVADOR L. 1982: Residual migration. Presented at the 52nd Annual International SEG Meeting, Dallas
- STOLT R. H. 1978: Migration by Fourier transform. *Geophysics* **43**, 1, pp. 23–48

A HIBÁS SEBESSÉGGEL VÉGREHAJTOTT SZEIZMIKUS MIGRÁCIÓ NÉHÁNY KÉRDÉSÉRŐL

Andrzej KOSTECKI és Anna PÓLCHŁOPEK

A tanulmány átfogóan elemzi a hibásan választott sebességnek a migráció jellegére gyakorolt hatását, különböző migrációs eljárások ($k_x-\omega$ migráció, k_x-t migráció és véges differenciák módszerével végzett $x-t$ migráció) esetén. Értelmezi és bizonyítja a hibás sebességből származtatott szeizmikus rétegdőlésszög változásokat és az azokat kísérő diszperziós jelenségeket. Példákat mutat be $\theta = 15^\circ, 30^\circ, 45^\circ$ dőlésű szeizmikus rétegek számítógépes modellezésére, a migrációs jelenség jobb megértése és szemléltetése céljából.

О НЕКОТОРЫХ ВОПРОСАХ СЕЙСМИЧЕСКОЙ МИГРАЦИИ, ОСУЩЕСТВЛЕННОЙ С НЕПРАВИЛЬНОЙ СКОРОСТЬЮ

Анджей КОСТЕЦКИ и Анна ПОЛХЛОПЕК

Детально анализируется влияние неправильно выбранной скорости на характер миграции при разных процедурах миграции (при миграции $k_x-\omega$, при миграции k_x-t и при миграции $x-t$, выполненной способом конечных разностей). Интерпретируются и доказываются изменения углов наклона сейсмических пластов, и сопровождающие их дисперсионные явления, образовавшиеся из-за неправильной скорости. Для лучшего понимания и демонстрации явления миграции показываются примеры моделирования на ЭВМ сейсмических пластов с наклоном $\theta = 15^\circ, 30^\circ$, и 45° .

COMPUTING OF TRANSIENT RESPONSE OF LAYERED HALFSPACE; PROBLEMS IN APPARENT RESISTIVITY INVERSION

Ernő PRÁCSER

This paper deals with the computation of the transient electromagnetic field on the surface of a layered halfspace for different transmitter-receiver configurations. The version of the spectral technique used here allows accurate computation of horizontal and vertical magnetic field components even at late times. An apparent resistivity computation method will be described, which is most advantageous because it is fast even for rectangular loops. This method is based on inverting formulae, expanded in series, that describe the transient field of a homogeneous halfspace; it gives accurate results at late times.

Keywords: electromagnetic methods, time domain, layered model, apparent resistivity, mathematical models

1. Introduction

In transient measurements different components of the magnetic field or their time derivatives are measured after turn-off of the direct currents flowing in the transmitter loop placed on the surface of the Earth. Depending on the resistivities of the layers in the halfspace, eddy currents are induced and they penetrate downwards like smoke rings. In the measurements the magnetic field of these currents is measured and we make attempts to deduce the layer parameters from the measurements. To perform these deductions with certainty, mathematical modelling of transient measurements over layered halfspace: i.e. computation of theoretical decay curves, is needed.

In the Eötvös Loránd Geophysical Institute (ELGI) we have been working on theoretical problems of the transient method since 1982. Our aim is the application of transient measurements in bauxite exploration and the development of their quick interpretation methods [KAKAS et al. 1985, 1986, in press]. These computer programs serve as a basis for this work and compute the transient field on the surface of a layered halfspace for the following three transmitter-receiver configurations (*Fig. 1*):

- a) Field of a magnetic dipole of vertical axis in the plane of the dipole, at distance r from the dipole; dipole-dipole array;
- b) Field at the midpoint of a circular loop lying on the surface of the halfspace; central induction loop (CIL) array;

c) Field at any point on the surface due to a rectangular loop laid out on the surface; TURAM array.

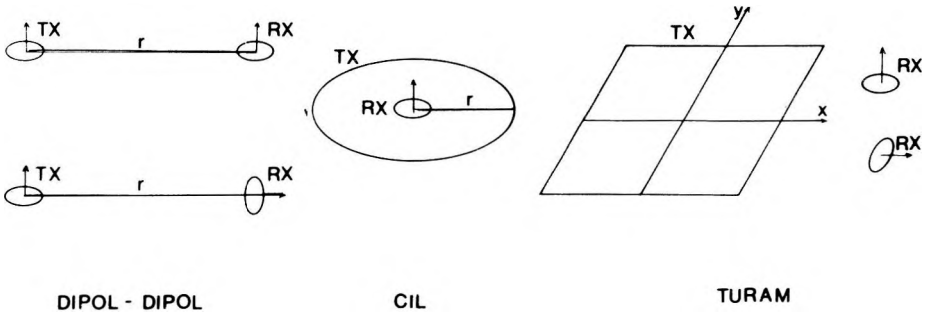


Fig. 1. Different transmitter–receiver configurations

1. ábra. Különböző adó–vevő elrendezések

Рис. 1. Разные установки датчика–приемника

An obvious and widely used method for computing transient curves is the application of inverse Fourier transformation to the frequency domain results. This is generally known as the spectral technique. In transient measurements inverse Fourier transformation means sine or cosine transformation. For any component of the magnetic field:

$$\dot{H}_u(t) = -\frac{2}{\pi} \int_0^{\infty} \text{Re}(H_u(\omega)) \cos \omega t \, d\omega \tag{1a}$$

$$\dot{H}_u(t) = \frac{2}{\pi} \int_0^{\infty} \text{Im}(H_u(\omega)) \sin \omega t \, d\omega \tag{1b}$$

where

$\dot{H}_u(t)$ is the time derivative of the magnetic field component of u direction, $\omega = 2\pi f$, f is the frequency, t is the time after turn-off of the direct current flowing in the transmitter loop, $H_u(\omega)$ is the magnetic field component of u direction in the frequency domain, u is the direction of a component (x , y or z).

The quick interpretation methods we use are based on apparent resistivity. Apparent resistivity is defined as the resistivity of a homogeneous halfspace that would produce a field component equal to the measured one for a given configuration. This is obtained by solving the following equation for ϱ :

$$\dot{H}_u^*(t, \varrho) = \dot{H}_u(t) \tag{2}$$

where

$\dot{H}_u^t(t, \varrho)$ is the value of the transient field component measured over homogeneous halfspace of resistivity ϱ , $\dot{H}_u^t(t)$ is the transient quantity to be transformed, measured over any kind of layered halfspace.

2. Computation of the magnetic field strength in frequency domain

For accuracy of transient curves computed by using the inverse Fourier transformation, adequate accuracy of frequency domain values and a reliable Fourier transformation technique are required. Therefore we should now briefly discuss the computation of the magnetic field in the frequency domain. For the CIL array the field of the electric dipole should be integrated along the circle, which means multiplication by $2\pi r$ because of symmetry. The formula describing the field of an electric dipole with axis in direction x over a layered halfspace is known from different sources [SCRIBA 1974, KAUFMAN and KELLER 1983]. Programs written in ELGI use the following formula:

$$H_z(\omega) = \frac{Idl}{4\pi} \frac{y}{r} \int_0^{\infty} J_1(\lambda r) \lambda e^{-\lambda z} (1 + R_0(\lambda)) d\lambda \quad (3)$$

where

J_1 is a Bessel function of the first kind, first order, z is the height of the transmitter. For convergence of the integral it is practical to choose a small z value, but not zero. x, y are the coordinates of the receiver, $r = \sqrt{x^2 + y^2}$, $R_0(\lambda)$ is the kernel function depending on layer parameters; it could be determined recursively.

$$R_j(\lambda) = \frac{\frac{\lambda_j - \lambda_{j+1}}{\lambda_j + \lambda_{j+1}} + R_{j+1}(\lambda) e^{-2d_j \lambda_j}}{1 + \frac{\lambda_j - \lambda_{j+1}}{\lambda_j + \lambda_{j+1}} R_{j+1}(\lambda) e^{-2d_j \lambda_j}}$$

$$\lambda_j = \sqrt{\lambda^2 + i\omega\mu\sigma_j}$$

where

σ_j is the conductivity of the j -th layer, d_j is the thickness of the j -th layer, $R_n(\lambda) = 0$, n is the number of layers, I is the current, and dl is the length of the dipole.

Here the response of the homogeneous halfspace having a resistivity equal to that of the first layer is not separated from the integral. Computation of the integral in (3) can be performed quickly and accurately using the filter method developed by Anderson [ANDERSON 1979, 1982]. From a computational viewpoint, the dipole-dipole array represents the same task as the CIL array with additional complication that the magnetic field has a horizontal component as well [KOEFOED et al. 1972, KAUFMAN and KELLER 1983].

The case of a rectangular loop is more complicated because the field of the electric dipole should be integrated along the loop, and that can be performed for the $H_z(\omega)$ component only numerically. This, together with the integral necessary for the Hankel transformation in equation (3) and the inverse Fourier transformation, means a threefold integration. By reasonable application of the filter method used for computing (3) the computation of the integral for all required values r does not take a significantly longer time than for only one r . Thus the computation time of the numerical integration along the loop can be reduced [ANDERSON 1982].

To compute the $H_x(\omega)$ component of the field of the loop, the $H_x(\omega)$ component of the field resulting from an electric dipole of direction x should be integrated along the two sides of direction x . Then the effect of the two sides of direction y should be added. After performing the $(x, y) \rightarrow (-y, x)$ coordinate transformation, the $H_y(\omega)$ component of the field resulting from the electric dipole of direction x should be integrated over x . The horizontal components of the magnetic field of the electric dipole are:

$$H_x(\omega) = \frac{Idl}{4\pi} \frac{\partial^2}{\partial x \partial y} \int_0^\infty J_0(\lambda r) \frac{e^{-\lambda z}}{\lambda} (1 + R_0(\lambda)) d\lambda \quad (4a)$$

$$H_y(\omega) = -\frac{Idl}{4\pi} \frac{\partial^2}{\partial x^2} \int_0^\infty J_0(\lambda r) \frac{e^{-\lambda z}}{\lambda} (1 + R_0(\lambda)) d\lambda + \frac{Idl}{4\pi} \int_0^\infty J_0(\lambda r) \lambda e^{-\lambda z} (1 - R_0(\lambda)) d\lambda \quad (4b)$$

The primitive function of $H_x(\omega)$ and the first term of the equation describing $H_y(\omega)$ exist in x , but for the second term numerical integration is necessary. Performing the computations, it should be taken into account that the current flowing in the opposite sides of the loop is of reverse direction. Details relating to the computation of the field of the loop in the frequency domain can be found in ANDERSON'S paper [1985].

3. Evaluation of the accuracy in computation of the transient field for late times

Transient curves computed by equations (1) become inaccurate primarily at late times. This can be recognized from the behaviour of the resistivity curves: with increasing time they fail to approximate asymptotically the resistivity of

the lower layer. Therefore in this section we evaluate the comparison and accuracy of transient computations over different models by means of apparent resistivity curves.

First, let us examine the CIL array. The TCILoop program was written at the United States Geological Survey (USGS) and ELGI received this program in 1982 through the scientific cooperation agreement between the USGS and the Central Office of Geology (KFH, Hungary). $\dot{H}_z(t)$ in this program is computed by equation (1a) [ANDERSON 1981], and from it the apparent resistivity, by an iterative method. The cosine transformation is carried out by a subroutine which is based on filtering and which was written by Anderson.

After adapting this program to ELGI's R-35 computer, test results computed for late times in the case of a resistive basement differed from those obtained on the VAX 11/780 computer of USGS. The reason for the deviations possibly lies in the difference in the precision of the two computers. From the resistivity curve (a) in Fig. 2, it can be seen that computation in the case of a resistive basement becomes unreliable with increasing time. The end of resistivity curve (b) computed for homogeneous halfspace shows some deviation from the correct values as well. For this reason our aim was to obtain a form of equations (1) which is more appropriate from the computational view point. Since the inaccuracy appears at late times, it could be explained by the behaviour of $H_z(\omega)$ for low values of ω . The following series expansions are valid for homogeneous halfspace:

$$\operatorname{Re}(H_z(\omega)) = \frac{I}{2r} \left(1 - \frac{\sqrt{2}}{15} r^3 \sqrt{\omega\mu\sigma^3} + \dots \right) \quad (5a)$$

$$\operatorname{Im}(H_z(\omega)) = \frac{I}{2r} \left(-\frac{1}{4} r^2 \omega\mu\sigma + \frac{\sqrt{2}}{15} r^3 \sqrt{\omega\mu\sigma^3} + \dots \right) \quad (5b)$$

where

σ is the conductivity of the halfspace and r is the radius of the circular transmitter loop.

The cosine transform of a constant and the sine transform of the ω -function are 0, therefore in the transformation of equations (1), the first terms of equations (5) theoretically make no contribution to the transient curve. With decreasing frequency the absolute values of these terms become greater than those of the other terms of the series which would make a contribution to the transient field. Because of the limited precision of the computer these other terms appear with steadily decreasing accuracy in the values of $\operatorname{Re}(H_z(\omega))$, and $\operatorname{Im}(H_z(\omega))$. As a limiting case it might happen that variables in the computer program containing the values of $\operatorname{Re}(H_z(\omega))$ and $\operatorname{Im}(H_z(\omega))$ become equal to the first terms in (5). Therefore one should not expect that transient curves computed by Eq.(1) have a correct asymptote for late times however accurate the technique used for inverse Fourier transformation may be. It is most expedient to remove the first terms of Eq.(5) by derivation. Computer programs

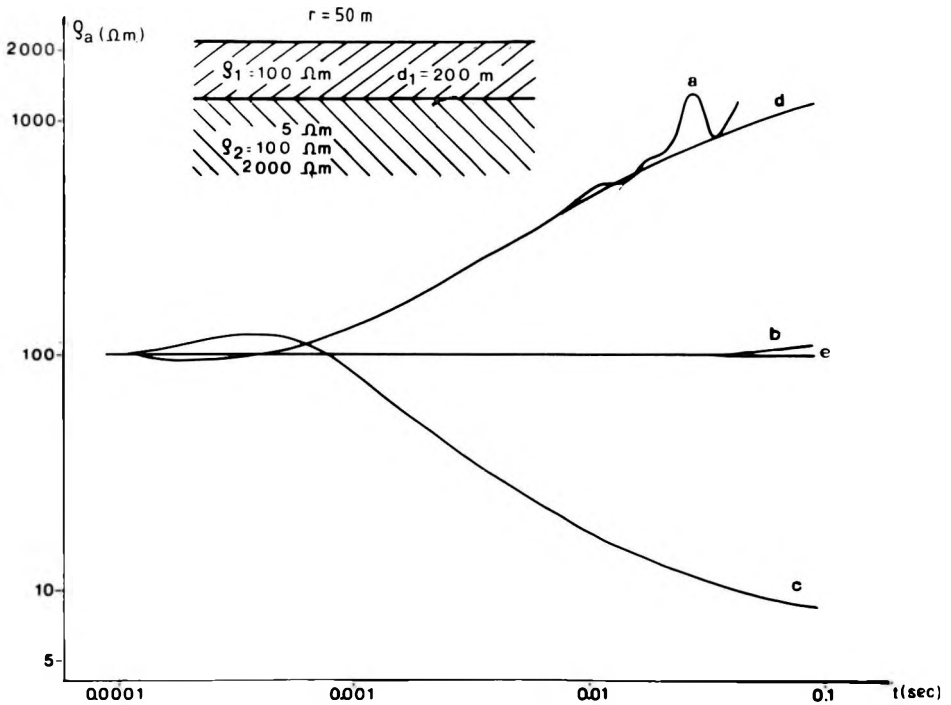


Fig. 2. Apparent resistivity curves for CIL array

For curves (a) and (d) $\rho_2 = 2000 \Omega m$, for (b) and (e) $\rho_2 = 100 \Omega m$, and for (c) $\rho_2 = 5 \Omega m$. Curves (a) and (b) were computed by Eq. 1a, curves (d) and (e) by Eq. 6, and curve (c) is the coinciding result of computation both by Eqs. (1a) and (6)

2. ábra. Látszólagos fajlagos ellenállásgörbék CIL elrendezésre

Az (a) és (d) görbére $\rho_2 = 2000 \Omega m$, (b) és (e) görbére $\rho_2 = 100 \Omega m$ és a (c) görbére $\rho_2 = 5 \Omega m$. Az (a) és (b) görbét az (1a) egyenlettel, a (d) és (e) görbét a (6) egyenlettel számítottuk, a (c) görbe mindkét egyenlettel azonosnak adódott

Рис. 2. Кривые кажущегося удельного сопротивления для соосной установки

Для кривых (a) и (d) $\rho_2 = 2000$ ом, для (b) и (e) $\rho_2 = 100$ ом, для (c) $\rho_2 = 5$ ом. Кривые (a) и (b) рассчитаны по формуле (1a), кривые (d) и (e) по формуле (6). Кривая (c) имеет одинаковый ход при применении любой формулы

written in ELGI compute components of the magnetic field using a formula obtained from (1b) by partial integration.

$$\dot{H}_u(t) = - \frac{2}{\pi t^2} \int_0^\infty \text{Im} \left(\frac{\partial^2}{\partial \omega^2} H_u(\omega) \right) \sin \omega t \, d\omega \quad (6)$$

If this form of sine transform is applied to Eq.(5.b.), then the disturbing first term disappears and the asymptote of the transient curve can be obtained accurately even for late times. Since the behaviour of $H_z(\omega)$ over layered models

is similar to that over homogeneous halfspace, and since the asymptotic behaviour is independent of the transmitter-receiver configuration as well, Eq.(6) can be used for computation of transient fields over layered models. Resistivity curves (d) and (e) shown in Fig.2 have been constructed on the basis of transient curves computed in this way. Conductive basement curves obtained by the two different methods coincide, i.e. curve (c) is obtained both by using Eq.(1a) and by using Eq.(6). For computation of sine transforms, a subroutine written by W. ANDERSON is used even if equation (6) is applied.

In the case of dipole-dipole and TURAM arrays, application of Eq.(6) plays an even more significant role in the computation of horizontal components because the accuracy of horizontal component computations using (1b) is much lower than that for vertical component computations (Fig.3, curves a and b). The explanation lies in the less favourable magnitude relations of terms in the series expansion of the formula describing the field strength in the frequency domain. For example, for a magnetic dipole

$$\text{Im}(H_r(\omega)) = \frac{IS}{4\pi r^3} \left(-\frac{\omega\mu\sigma r^2}{4} - \frac{3\pi}{64}(\omega\mu\sigma r^2)^2 + \dots \right) \quad (7)$$

where

IS is the moment of the magnetic dipole.

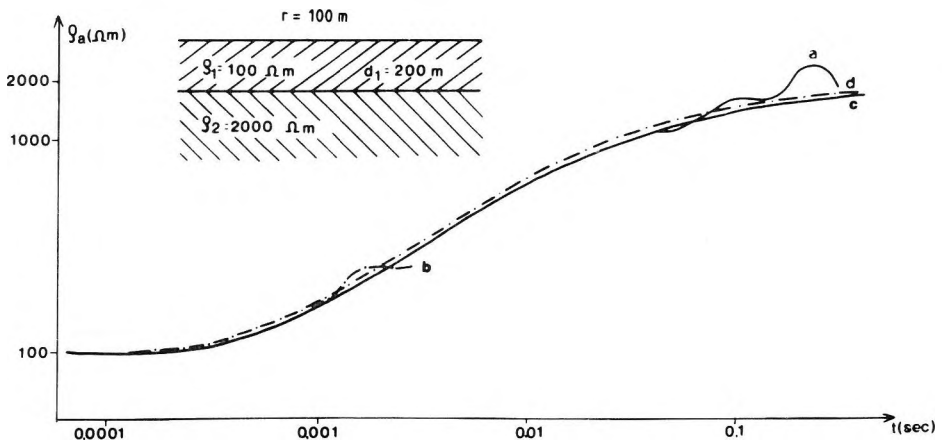


Fig. 3. Apparent resistivity curves for a magnetic dipole

Curves (a) and (c) are derived from $\dot{H}_z(t)$, curves (b) and (d) from $\dot{H}_r(t)$. Curves (a) and (b) were computed by Eq. (1b), curves (c) and (d) by Eq. (6)

3. ábra. Látszólagos fajlagos ellenállásgörbék mágneses dipólra

Az (a) és (c) görbe $\dot{H}_z(t)$ -ből, a (b) és (d) görbe $\dot{H}_r(t)$ -ből származtatva. Az (a) és (b) görbét az (1b) egyenlettel, a (c) és (d) görbét a (6) egyenlettel számítottuk

Рис. 3. Кривые кажущегося удельного сопротивления для магнитного диполя

Кривые (а) и (с) получены по компоненту $\dot{H}_z(t)$, а (b) и (d) по $\dot{H}_r(t)$. Кривые (а) и (b) рассчитаны по формуле (1b), а кривые (с) и (d) по формуле (6)

As ω tends to zero, the second term of (7) — which plays a role in determination of the asymptote valid for late times — approaches zero more rapidly than the second term of (5b). Therefore this term is less significant compared with the first term in the value of $\text{Im}(H_r(\omega))$ than is the second term of (5b) for the vertical component. Resistivity curves *a* and *b* Fig.3 have been constructed using Eq.(1b), and curves *c* and *d* using Eq.(6).

The computation of $\frac{\partial^2}{\partial \omega^2} H_z(\omega)$ and $\frac{\partial^2}{\partial \omega^2} H_r(\omega)$ is worth mentioning. The faster method is to compute values of $H_z(\omega_j)$ and $H_r(\omega_j)$ at given points (ω_j , $j = 1, 2, \dots, n$) of the frequency band necessary to perform transformation, and then to determine the values of the second derivative by spline approximation for every ω required to perform sine transformation. In this case the accuracy of transient curves improves mainly for the vertical components; for the less favourable horizontal components the improvement is negligible. A more accurate method is to determine numerically the second ω derivative of the $R_0(\lambda)$ kernel function contained in the integral used for Hankel transformation. Unfortunately, as a consequence the running time of the program increased significantly. In addition to the plotted resistivity curves, improvements in the accuracy achieved are also demonstrated by *Table I*. The transient field values for a magnetic dipole over a two-layer halfspace are given in the columns of the table.

$\frac{2t}{\mu\sigma_1 r^2}$	$\frac{2\pi\sigma_1 r^5}{M_z} \left(\frac{\delta B_z}{\delta t} \right)$			
	Spectral method Goldman 1983.	Spectral method Anderson 1983.	Integral-finite- difference method Goldman 1983.	Spectral method ELGI 1986.
0.100E0	0.662E1	0.662E1	0.662E1	0.662E1
0.178E0	0.230E1	0.230E1	0.230E1	0.230E1
0.316E0	0.597E-2	0.597E-2	0.597E-2	0.573E-2
0.562E0	-0.293E0	-0.293E0	-0.293E0	-0.293E0
0.100E1	-0.147E0	-0.147E0	-0.147E0	-0.147E0
0.178E1	-0.498E-1	-0.498E-1	-0.498E-1	-0.498E-1
0.316E1	-0.142E-1	-0.142E-1	-0.142E-1	-0.142E-1
0.562E1	-0.376E-2	-0.376E-2	-0.376E-2	-0.376E-2
0.100E2	-0.973E-3	-0.973E-3	-0.971E-3	-0.973E-3
0.178E2	-0.241E-3	-0.241E-3	-0.239E-3	-0.241E-3
0.316E2	-0.523E-4	-0.523E-4	-0.520E-4	-0.523E-4
0.562E2	-0.972E-5	-0.971E-5	-0.975E-5	-0.972E-5
0.100E3	-0.155E-5	-0.155E-5	-0.155E-5	-0.155E-5
0.178E3	-0.217E-6	-0.216E-6	-0.215E-6	-0.216E-6
0.316E3	-0.272E-7	-0.270E-7	-0.272E-7	-0.270E-7
0.562E3	-0.316E-8	-0.311E-8	-0.312E-8	-0.312E-8
0.100E4	-0.309E-9	-0.342E-9	-0.340E-9	-0.340E-9
0.178E4	0.198E-10	-0.361E-10	-0.358E-10	-0.358E-10
0.316E4	-0.187E-10	-0.352E-11	-0.369E-11	-0.370E-11
0.562E4	0.512E-11	-0.348E-12	-0.375E-12	-0.375E-12
0.100E5	-0.130E-10	-0.653E-13	-0.379E-13	-0.380E-13

Using a procedure similar to the method of obtaining formula (6) from (1b), formula (1a) could be modified as well.

Given the results of the frequency domain computations, it was possible to compute the transient field for a rectangular loop in the same way as for the dipole-dipole and CIL arrays. In this case, there is greater difficulty in conceptualizing a computational method for rectangular loops based on the time domain solution of Maxwell equations than for magnetic dipole and CIL array, which emphasizes the significance of the spectral technique. In the fourth column of Table I the results obtained by the time domain solution of Maxwell equation are listed [GOLDMAN 1983, 1984]. The resistivity curves shown in Fig. 4 are constructed using vertical and horizontal components of the transient field resulting from a rectangular loop.

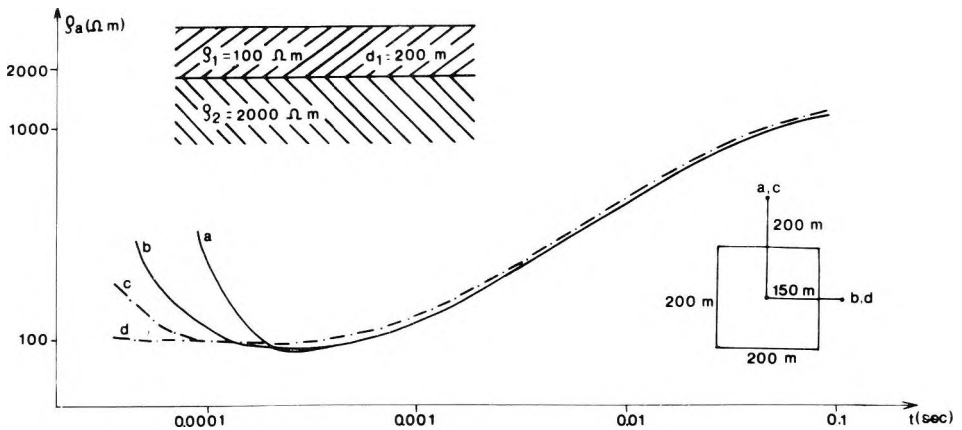


Fig. 4. Apparent resistivity curves for TURAM array

Curves (a) and (b) are derived from $\dot{H}_z(t)$, curve (c) from $\dot{H}_y(t)$ and curve (d) from $\dot{H}_x(t)$. All curves computed by Eq. 6

4. ábra. Látszólagos fajlagos ellenállásgörbék TURAM elrendezésre

Az (a) és (b) görbe $\dot{H}_z(t)$ -ből, a (c) görbe $\dot{H}_y(t)$ -ből, a (d) görbe pedig $\dot{H}_x(t)$ -ből származtatva. Mindegyik görbét a (6) egyenlettel számítottuk

Рис. 4. Кривые кажущегося удельного сопротивления для установки TURAM

Кривые (a) и (b) получены по компоненту $\dot{H}_z(t)$, (c) – по $\dot{H}_y(t)$, а (d) по $\dot{H}_x(t)$. Все кривые рассчитаны по формуле (6)

Table I.

Comparison of TEM field values computed by different methods for a two-layered section with $\sigma_2 = \infty$; $r/h_1 = 0.25$ [after GOLDMAN]

1. táblázat Különböző módszerekkel számított tranzienes tér értékek kétréteges modell felett mágneses dipól gerjesztésre $\sigma_2 = \infty$; $r/h_1 = 0,25$ [GOLDMAN nyomán]

Табл. I. Значения поля переходного процесса над двухслойной средой, при возбуждении магнитным диполем, полученные разными способами $\sigma_2 = \infty$, $r/h_1 = 0,25$ [по ГОЛДМАНУ]

Up to this point, the expression “transient field” has meant time derivatives of field components ($H_z(t)$, $H_r(t)$, $H_x(t)$, $H_y(t)$). The components themselves can be obtained from derivatives by integration over time.

4. Computational methods for apparent resistivity

It is generally more meaningful to examine the apparent resistivities instead of the measured or calculated field components. Resistivity can be derived from the field components, and the resistivity relations of the layers can be deduced more easily from the apparent resistivities than from the measured quantities, the decay curves. In apparent resistivity calculation (briefly: resistivity calculation) known parameters (moments of the transmitter and receiver and their relative position) are removed from the transient curves.

The solution of Eq.(2) can be obtained by iteration or by inverting the series expansion of $H_z^f(t, \varrho)$. SPIES and RAICHE [1980] have applied this latter method for coincident transmitter and receiver loops. By iterative methods two resistivity curves can be obtained; one is correct for early times and reflects the resistivities of the near-surface layers, the other is correct for late times, and reflects the response of deeper layers. This second curve can be obtained in close approximation by inverting the series expansion of $H_z^f(t, \varrho)$. For dipole-dipole and CIL arrays the iterative solution is also feasible because the transient field over homogeneous halfspace is given by a relatively simple formula. The other advantage of these arrays is that essentially only one transient curve exists over homogeneous halfspace. In the case of a rectangular loop the situation is considerably more complicated. Since in this case $H_z^f(t, \varrho)$ is the integral of the transient field of the electric dipole along the loop, an iterative solution of Eq.(2) would be extremely slow. It would be possible to calculate $H_z^f(t, \varrho)$ for one suitably long time interval, in properly dense time moments, and then to store the results and use it in every subsequent case for the solution of Eq. (2). However, this way is not expedient because for rectangular loops there are as many kinds of transient curves over the homogeneous halfspace as there are transmitter–receiver positions. Only those transmitter–receiver configurations can be considered as equivalent that are generated by enlargement/reduction. Therefore the following method, which is based on inverting the series expansion of $\dot{H}_z^f(t, \varrho)$ and which provides correct results primarily for late sections of the transient curve, is advisable.

Let us start from the series expansion of the formula describing the transient field of the electric dipole over homogeneous halfspace.

$$\dot{H}_z^f(t, \varrho) = - \frac{yI dl}{\pi^{\frac{3}{2}} 4tr^3} (a\alpha^3 + b\alpha^5 + c\alpha^7 + d\alpha^9 + \dots) \quad (8)$$

where

a, b, c, \dots are known constants, and $\alpha^2 = \frac{\mu\sigma r^2}{4t}$

The transient field of a rectangular loop can be obtained by integrating the field of dipoles along the sides of the loop, using the following integral (in this case for one of the loop sides, parallel to the x axis):

$$\int_{x_1}^{x_2} (x^2 + y^2)^k dx = \sum_{j=0}^k \binom{k}{j} y^{2j} \left(\frac{x_2^{2(k-j)+1}}{2(k-j)+1} - \frac{x_1^{2(k-j)+1}}{2(k-j)+1} \right) \quad (9)$$

$$\dot{H}_z^f(t, \varrho) = - \frac{I}{\pi^{\frac{3}{2}} 4t\bar{r}} (a\alpha^3 + b\alpha^5 + c\alpha^7 + d\alpha^9 + \dots) \quad (10)$$

where

\bar{r} is a quantity related to the transmitter-receiver configuration:

$$\bar{r} = \frac{r_1 + r_2 + r_3 + r_4}{4},$$

r_j is the distance between the midpoint of the j -th side of the loop and the measuring site,

and

$$\alpha^2 = \frac{\mu\sigma\bar{r}^2}{4t}.$$

Coefficients a, b, c, \dots depend on the transmitter-receiver configuration and, using (9), may be calculated quickly.

Let us solve (2). Substitute in (10) the transient quantity to be transformed for the transient value over the homogeneous halfspace:

$$\beta = - \frac{\pi^{\frac{3}{2}} 4t\bar{r} \dot{H}_z^f(t)}{I} = a\alpha^3 + b\alpha^5 + c\alpha^7 + d\alpha^9 + \dots \quad (11)$$

To this series there belongs an inverse series giving α as a function of β .

$$\alpha = A\beta^{\frac{1}{3}} + B\beta + C\beta^{\frac{5}{3}} + D\beta^{\frac{7}{3}} + \dots \quad (12)$$

Coefficients A, B, C, \dots can be obtained from $a, b, c \dots$ using the following formulae:

$$A = \frac{1}{a^{\frac{1}{3}}}$$

$$B = - \frac{b}{3a^2}$$

$$C = \frac{4}{9} \frac{b^2}{a^{\frac{11}{3}}} - \frac{1}{3} \frac{c}{a^{\frac{8}{3}}}$$

$$D = \frac{1}{a^{\frac{1}{3}}} \left(-\frac{d}{3a^3} + \frac{10}{9} \frac{bc}{a^4} - \frac{65}{81} \frac{b^3}{a^5} \right)$$

$$E = \frac{5}{3} \frac{b^4}{a^7} - \frac{10}{3} \frac{b^2c}{a^6} + \frac{4}{3} \frac{bd}{a^5} + \frac{2}{3} \frac{c^2}{a^5} - \frac{1}{3} \frac{e}{a^4}$$

$$F = \frac{1}{a^{\frac{2}{3}}} \left(-\frac{2737}{729} \frac{b^5}{a^8} + \frac{2380}{243} \frac{b^3c}{a^7} - \frac{119}{27} \frac{b^2d}{a^6} - \frac{119}{27} \frac{bc^2}{a^6} + \frac{14}{9} \frac{be}{a^5} + \frac{14}{9} \frac{cd}{a^5} - \frac{1}{3} \frac{f}{a^4} \right)$$

$$G = \frac{1}{a^{\frac{1}{3}}} \left(\frac{54\,200}{6561} \frac{b^6}{a^{10}} - \frac{20\,180}{729} \frac{b^4c}{a^9} + \frac{3344}{243} \frac{b^3d}{a^8} + \frac{1642}{81} \frac{b^2c^2}{a^8} - \frac{152}{27} \frac{b^2e}{a^7} - \frac{304}{27} \frac{bcd}{a^7} + \frac{16}{9} \frac{bf}{a^6} - \frac{152}{81} \frac{c^3}{a^7} + \frac{16}{9} \frac{ce}{a^6} + \frac{8}{9} \frac{d^2}{a^6} - \frac{1}{3} \frac{g}{a^5} \right)$$

Coefficients of series (12) need be determined only once for each transmitter–receiver configuration. Apparent resistivity values can be attached to the individual time moments in the following way: $\dot{H}_z(t)$, t , \bar{r} and I are known, so at first β is obtained from the first equation of (11), then α is obtained from the series (12) and, using the definition of α , σ and $\varrho = 1/\sigma$ can be expressed.

Similarly, resistivity calculation based on $\dot{H}_x(t)$ can be carried out, with the difference that the series expansion of $\dot{H}_x^l(t, \varrho)$ is obtainable only by more laborious computations.

The above method might also be applied to the dipole-dipole and CIL arrays, with the difference that to obtain the series expansion describing the transient field over the homogeneous halfspace there is no need for integration along the transmitter wire.

One possible characteristic of the quality of apparent resistivity calculations is the accuracy that can be achieved in re-obtaining the resistivity of the homogeneous halfspace by applying these calculations to the transient curve calculated over the homogeneous halfspace. This method is worth applying if the condition $\alpha < 1$ obtains.

In Fig. 4 it can be seen that apparent resistivity values deviate from the resistivity of the first layer at early times. It is obvious that on the one hand, the behaviour of the horizontal components is more favourable from this viewpoint, and that, on the other hand, deteriorating accuracy of this resistivity calculation for early times results from moving away from the transmitter. Disregarding the deviations appearing at early times, field components at different sites provide the same apparent resistivity. Curves c , d and e of Fig. 2 and the curves in Figs. 3 and 4 have been obtained from the series expansion of formulae describing the field over homogeneous halfspace, using the coefficients from first to seven. Determination of further coefficients would be useless

because the expressions describing them become more and more complicated and their use would ensure only a negligible improvement in the results.

Resistivity curves *a*, *b* and *c* in Fig. 2 have been constructed by an iterative method on the basis of $\tilde{H}_z(t)$ calculated from (1a). Thus in those intervals where the program using formula (1a) gives accurate results, the coincidence of the curves demonstrates that the two resistivity calculations are of equal quality.

5. Conclusions

By applying equation (6) every component of the magnetic field measurable on the surface of the layered halfspace can be calculated correctly for all three transmitter–receiver configurations. The resistivity calculation method discussed above allows calculation and analysis of resistivity curves over different layered models and this is a great help in interpreting resistivity curves calculated from transient values measured in the field.

REFERENCES

- ANDERSON W. L. 1979: Numerical integration of related Hankel transforms of orders 0 and 1 by adaptive digital filtering. *Geophysics*, **44**, 7, pp. 1287–1305
- ANDERSON W. L. 1981: Transient soundings for central induction loop forward solutions for layered models. USGS Open-File Report 81–1309
- ANDERSON W. L. 1982: Fast Hankel transforms using related and lagged convolutions. *Association for Computing Machinery Transactions on Mathematical Software* **8**, 4, pp. 344–368
- ANDERSON W. L. 1985: Fast evaluation of radial and vertical magnetic fields near a rectangular loop source on a layered earth. *Geophysical Transactions*, **31**, 4, pp. 339–357
- GOLDMAN M. M. 1983: The Integral-finite difference method for calculating transient electromagnetic fields in a horizontally stratified medium. *Geophysical Prospecting*, **31**, 4, pp. 664–686
- GOLDMAN M. M. 1984: Addendum to “The Integral-finite difference method for calculating transient electromagnetic fields in a horizontally stratified medium” by M. M. Goldman. *Geophysical Prospecting*, **32**, 3, pp. 507–509
- KAKAS K., FRISCHKNECHT F. C., ÚJSZÁSI J., ANDERSON W. L. and PRÁCSEER E. 1985: Transient electromagnetic soundings development of interpretation methods and application to bauxite exploration. *Geophysical Transactions*, **31**, 1–3 pp. 295–310
- KAKAS K., MCNEILL J. D., BALOG GY., PRÁCSEER E., SÓRÉS L. and ÚJSZÁSI J. 1986: Depth inversion for transient EM soundings: the TRH technique and results for central induction loop layout. EAEG 48th Meeting and Technical Exhibition, Oostende (443.)
- KAKAS K., BALOG GY., PRÁCSEER E., SÓRÉS L. és ÚJSZÁSI J. (in press): A tranziens módszer hazai bevezetése, fejlesztése és alkalmazása. Annual Report of the Eötvös Loránd Geophysical Institute of Hungary for 1985
- KAUFMAN A. A. and KELLER G. V. 1983: *Frequency and Transient Soundings*. Amsterdam–Oxford–New-York, Elsevier
- KOEFOD O., GHOSH D. P. and POLMAN G. J. 1972: Computation of type curves for electromagnetic depth sounding with a horizontal transmitting coil by means of a digital linear filter. *Geophysical Prospecting*, **20**, 2, pp. 406–420
- SCRIBA, H. 1974: A numerical method to calculate the electromagnetic field of a horizontal current dipole. *Pageoph*, **112**, 5, pp. 801–809
- SPIES B. R. and RAICHE A. P. 1980: Calculation of apparent conductivity for the transient electromagnetic (coincident loop) method using an HP-67 calculator. *Geophysics*, **45**, 7, pp. 1197–1200

**RÉTEGEZETT FÉLTÉR TRANZIENS VÁLASZÁNAK SZÁMÍTÁSA, LÁTSZÓLAGOS
FAJLAGOS ELLENÁLLÁS MEGHATÁROZÁSA**

PRÁCSER Ernő

A cikk a rétegzett féltér felszínén kialakuló tranziens elektromágneses tér számításával foglalkozik, különböző adó-vevő elrendezések esetében. A spektrál módszernek az itt alkalmazott változata lehetővé teszi a mágneses térerősség függőleges és vízszintes komponensének pontos számítását késő idő értékekre is. A tanulmány egy látszólagos fajlagos ellenállászámítási eljárást is ismertet, amelynek a gyorsasága folytán a négyszögletes keret esetében van a legnagyobb jelentősége. Ez a módszer a homogén féltér tranziens terét leíró képletek sorbafejtett alakjának invertálásán alapul és késői időértékek esetén ad pontos eredményt.

**РАСЧЕТ ПОЛЯ ПЕРЕХОДНОГО ПРОЦЕССА НАД СЛОИСТЫМ
ПОЛУПРОСТРАНСТВОМ, ОПРЕДЕЛЕНИЕ КАЖУЩЕГОСЯ УДЕЛЬНОГО
СОПРОТИВЛЕНИЯ**

Эрнő ПРАЧЕР

В этой статье изложен расчет электромагнитного поля переходного процесса, образующегося на поверхности слоистого полупространства, для случая разных установок. Примененный здесь вариант спектрального способа дает возможность точно определить значений вертикального и горизонтального компонентов магнитного поля даже при поздних временах. Также излагается один способ расчета кажущегося удельного сопротивления, который, в связи со своей быстротой, имеет значение прежде всего для случая квадратных рамок. Этот способ основан на инвертации разложенных в ряд формул, описывающих поле переходного процесса однородного полупространства, и дает точные результаты для поздних времен.

A MODEL FOR THE VERTICAL SUBSURFACE RADON TRANSPORT IN "GEOGAS" MICROBUBBLES

András VÁRHEGYI*, István BARANYI* and György SOMOGYI**

Based on the phenomenon of "geogas", rising in the form of microbubbles from deeper regions, the authors have developed a new model for the transport of radon released from deep sources, and a new method for its detection. The advantage of the new model compared to the earlier ones is the elimination of the well-known problems of the radon emanation research methods (penetration depth, reproducibility, etc.), and it provides a qualitative and quantitative description of the transport mechanism, which is realistic from both geological and physical viewpoints. The authors emphasize the role of groundwater and gases of deep origin in the movement of radon, briefly discussing possible sources of these gases. The problems of detecting the radon below the water-table with track detectors are reviewed and the connection between the rock physical parameters (tortuosity, porosity, grain size distribution) and transport characteristics is investigated in detail. Assuming different geological conditions and rock physical parameters theoretical vertical radon concentration and track production profiles were calculated. Finally detectability of deep radon sources depending on geological conditions is analysed and methodological recommendations are made for the more efficient use of the radon emanation uranium exploration methods.

Keywords: radon, transport, models, uranium ores, emanation method, track-etch method, microbubbles, geogas

1. Introduction

A worldwide trend in the exploration for uranium is the growing interest in mineralization at greater depths, after having discovered the near-surface deposits. Methods based on the measurement of gamma radiation (gamma level mapping and gamma spectrometry) are being replaced by other indirect methods like radon emanometry and geochemistry. There is a large volume of literature dealing with the versatile application of the radon emanation (briefly radon) exploration method (detection of uranium ores, prediction of earthquakes, exploration of geothermal energy resources, etc.). The state of the art is well reflected by the review paper of GINGRICH [1984], indicating some of the problems and doubts in the course of development of geochemical exploration using radon.

Results obtained by pump-type emanometers applying short-term sampling are not reliable, the anomaly pattern changes in time. GINGRICH and FISHER [1976] listed eight environmental factors that might influence the instantaneous radon concentration of the soil air. It is rather difficult or impossible

* Mecsek Ore Mining Enterprise, POB 121, Pécs, H-7614

** Institute of Nuclear Research of the Hungarian Academy of Sciences, Debrecen, H-4001
Manuscript received: 26 March, 1986

to take all these effects into account. According to our experience the radon concentration of the soil air can change by one or two orders of magnitude even within the same day.

The 70's brought significant changes in the radon detection devices developed for integrating measurements, first of all the alpha sensitive solid state track detectors have appeared. Using these monitors the undesirable effects caused by short-term variations in the radon concentration of the soil air can be eliminated, although even these integrating measurements indicate long-term seasonal variations. Emanation measurement with inverted cups placed in 50 to 100 cm deep holes is widespread [GINGRICH and FISHER 1976; FLEISCHER and MOGRO-CAMPERO 1978; SOMOGYI et al. 1978; TITOV et al. 1985].

2. Problems of integrating radon measurement techniques

The opinion of scientists involved in uranium exploration is not unanimous concerning the usefulness and reliability of the emanation method, although most of the technical problems encountered in practice have been properly solved. The misting over of detector films [LIKES et al. 1977], the radon – thoron discrimination [WARD et al. 1977], the distinguishing between deep and shallow radon sources [FLEISCHER and MOGRO-CAMPERO 1978], the depth dependence of radon detection [SOMOGYI et al. 1982; KRISTIANSOON and MALMQVIST 1984], the effect of the detector cup geometry and the detector type [FLEISCHER and MOGRO-CAMPERO 1978; SOMOGYI et al. 1982, 1983], the role of the meteorological factors [CLEMETS and WILKENING 1974]: all have been thoroughly studied and are mostly solved problems.

The behaviour of radon in the real physical environment determined by geology, however, raises further specific difficulties. The question of measurement reproducibility in time has not been solved satisfactorily. The reasons for interpretation problems are the seasonal variation in radon emission [SOMOGYI et al. 1978, 1982], and on the other hand the great differences often observed in field measurements carried out close to each other [KRISTIANSOON and MALMQVIST 1984]. These allow only probability conclusions to be reached in the interpretation of the results.

The most severe problem is, however, to determine the maximum depth of Rn sources that can produce concentrations detectable on the surface and significantly higher than the "background noise". Several case histories have been published about the detection of uranium mineralizations at the depth of 100 m or even deeper, using integrating radon measurement [GINGRICH 1975; BECK and GINGRICH 1976; GINGRICH and FISCHER 1976; FLEISCHER and MOGRO-CAMPERO 1978; TITOV et al. 1985]. At the same time under unfavourable geological conditions even near-surface deposits might remain undetected by emanation exploration methods.

In the author's opinion the problems about the emanation method are seated in the lack of a geological and physical model which properly describes

the migration of radon from greater depths to near the surface. No unambiguous exploration criteria are available for planning the technical parameters of emanation measurements and the results cannot be interpreted quantitatively. In the present paper after briefly summarizing the existing theories for radon transport the authors introduce a novel transport mechanism which seems to be able to solve the long-standing problems. Formulas suitable for the quantitative description of the subsurface radon transport and results obtained by the track detector exploration technique are presented as well. Vertical radon concentration profiles calculated using the new theory are shown and some practical methods are recommended.

3. Traditional theories for radon transport

The steady state depth (1D) distribution of radon concentration in a homogeneous host medium is given by the differential equation [GRAMMAKOV 1936]

$$D \frac{\partial^2 c}{\partial z^2} - \frac{\partial(vc)}{\partial z} - \lambda c + Q = 0, \quad (1)$$

where

c is the radon concentration ($\text{atom} \cdot \text{cm}^{-3}$)

D is the diffusion coefficient of radon ($\text{cm}^2 \text{ s}^{-1}$)

v is the velocity of the medium carrying the radon in z direction (cm s^{-1})

λ is the decay constant of radon (s^{-1})

Q is the intensity of radon generation in the host medium ($\text{atom} \cdot \text{cm}^{-3} \cdot \text{s}^{-1}$)

It is noted that in porous media (e.g. in rocks) effective values should be used, like $D = D_{eff}/\varepsilon$ and $v = v_{eff}/\varepsilon$, where ε is the effective porosity of the medium.

Using a wide variety of approximations and boundary conditions different solutions of equation (1) are given in the literature. Solutions of the equation for two simple geological models are summarized in *Tables 1/a* and *b*.

If the transport of radon is due to diffusion only, attenuation of radon concentration moving away from the radon source is described by the diffusion length

$$z_d = \sqrt{D/\lambda} \quad (2)$$

and at this distance the Rn concentration is the e -th part of that at the source. So using the possible highest diffusion coefficient (which is the diffusion coefficient of radon for air: $\sim 0.1 \text{ cm}^2 \cdot \text{s}^{-1}$), the radon concentration decreases to its one thousandth part within 15 m from the source.

To explain the radon movement from greater depths encountered under natural conditions several authors suggest another transport mechanism, the

vertical upward flow of the medium filling the pore space. Detectable radon concentration anomalies from about 100 m deep sources, however, could be explained this way only if a flow velocity of several $\text{m} \cdot \text{day}^{-1}$ is supposed for the medium filling the pores. In our opinion flow velocities of this order of magnitude for the pore filling medium (being either gas or fluid) cannot be taken as realistic ones from the geological viewpoint (excluding some extreme cases, like active faults, volcanic or postvolcanic areas).

According to recent investigations [KRISTIANSSON and MALMQVIST 1982; MALMQVIST and KRISTIANSSON 1984, 1985; BARANYI et al. 1985; SOMOGYI and LÉNÁRT 1985] it seems reasonable that the buoyant force, the result of the differences in the density of ground water and gases moving upward, can ensure the required transport velocities if the upward flow means movement of microbubbles consisting of different gases, including radon. The assumption of upward bubble movement adds new geological, physical and mathematical aspects to the radon transport model.

4. Origin of subsurface gases and their role in radon transport

KRISTIANSSON and MALMQVIST [1982] were the first to suggest that the upward flow of gases from deep sources in bubble form could be a factor of decisive importance in radon transport. In a recent paper the same authors [MALMQVIST and KRISTIANSSON 1984] reported on the measurement of the flux of the upward moving gas bubbles from deep sources ("geogas") under different geologic conditions, and on the chemical composition of these gases.

BARANYI et al. [1985] called the attention to the fact that — especially in the vicinity of radioactive ore deposits — large volumes of gases could be released by radioysis as well. If the medium is water-bearing a part of the radioactive energy, first of all energy released by alpha decay, is used for decomposition of the water molecules in the close vicinity. According to VOVK [1981] an alpha decay occurring in water can result in $4\text{--}8.5 \cdot 10^3$ radiolytically decomposed water molecules, depending on the energy of the alpha particle. Thus a radioactive ore deposit could be regarded as a special gas-generating object. During the complete decay of a ^{238}U atom, besides the gaseous products of the decay series, one ^{222}Rn and eight ^4He atoms, 36,000 water molecules could be decomposed radiolytically in water-bearing environment, as an average. The released hydrogen generally forms free H_2 molecules, while the oxygen is usually bonded to organic materials often accompanying the uranium deposits or it is released as CO_2 .

Several measurements demonstrate the wide range of possibilities for the existence of an upward gas flow in nature the flux of which may exceed the value of several thousand $\text{cm}^3 \cdot \text{m}^{-2} \cdot \text{year}^{-1}$ [VOYTOV 1974, SUGISAKI et al. 1983, MALMQVIST and KRISTIANSSON 1984]. In case of such a significant gas flow through water-filled rock pores, movement of gases in the form of microbubbles and the development of an unusually high vertical component of the gas flow

Table I/a

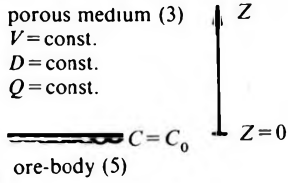
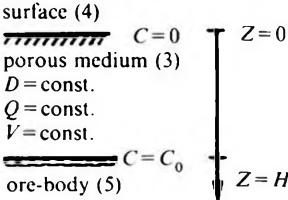
Model I: "thick" overburden (1)	Model II: "shallow" overburden (2)
porous medium (3) $V = \text{const.}$ $D = \text{const.}$ $Q = \text{const.}$  ore-body (5)	surface (4)  ore-body (5)
Boundary conditions: (6) at $Z=0$ $C = C_0$ when $Z \rightarrow \infty$ $C = \frac{Q}{\lambda}$	Boundary conditions: (6) at $Z=0$ $C = 0$ at $Z=H$ $C = C_0$

Table I/b

(8) Mechanism	(9) Differential equation	(10) General solution	(11) Solution for Model I.	(12) Solution for Model II.
(1) decay + generation	$-\lambda c + Q = 0$	$c = \frac{Q}{\lambda}$	$c = \frac{Q}{\lambda}$ boundary conditions cannot be used (13)	$c = \frac{Q}{\lambda}$ boundary conditions cannot be used (13)
(2) diffusion + decay	$D \frac{\partial^2 c}{\partial Z^2} - \lambda c = 0$	$c = K_1 e^{\sqrt{\frac{\lambda}{D}} Z} + K_2 e^{-\sqrt{\frac{\lambda}{D}} Z}$	$c = c_0 e^{-\sqrt{\frac{\lambda}{D}} Z}$	$c = c_0 \frac{\text{sh} \sqrt{\frac{\lambda}{D}} Z}{\text{sh} \sqrt{\frac{\lambda}{D}} H}$
(3) transport + decay	$-v \frac{\partial c}{\partial Z} - \lambda c = 0$	$c = K e^{-\frac{\lambda}{v} Z}$	$c = c_0 e^{-\frac{\lambda}{v} Z}$	$c = c_0 e^{\frac{\lambda}{v} (Z-H)}$ only the lower boundary condition can be used (14)
(4) diffusion + decay + generation	$D \frac{\partial^2 c}{\partial Z^2} - \lambda c + Q = 0$	$c = K_1 e^{\sqrt{\frac{\lambda}{D}} Z} + K_2 e^{-\sqrt{\frac{\lambda}{D}} Z} + \frac{Q}{\lambda}$	$c = \left(c_0 - \frac{Q}{\lambda} \right) e^{-\sqrt{\frac{\lambda}{D}} Z} + \frac{Q}{\lambda}$	$c = \left(c_0 - \frac{Q}{\lambda} \right) \frac{\text{sh} \sqrt{\frac{\lambda}{D}} Z}{\text{sh} \sqrt{\frac{\lambda}{D}} H} + \frac{Q}{\lambda} \left(1 - \frac{\text{sh} \sqrt{\frac{\lambda}{D}} (H-Z)}{\text{sh} \sqrt{\frac{\lambda}{D}} H} \right)$
(5) transport + decay + generation	$-v \frac{\partial c}{\partial Z} - \lambda c + Q = 0$	$c = K e^{-\frac{\lambda}{v} Z} + \frac{Q}{\lambda}$	$c = \left(c_0 - \frac{Q}{\lambda} \right) e^{-\frac{\lambda}{v} Z} + \frac{Q}{\lambda}$	$c = \left(c_0 - \frac{Q}{\lambda} \right) e^{\frac{\lambda}{v} (Z-H)} + \frac{Q}{\lambda}$ only the lower boundary condition can be used (14)
(6) diffusion + transport + decay	$D \frac{\partial^2 c}{\partial Z^2} - v \frac{\partial c}{\partial Z} - \lambda c = 0$	$c = e^{\frac{v}{2D} Z} \left[K_1 \exp Z \sqrt{\frac{v^2}{4D^2} + \frac{\lambda}{D}} + K_2 \exp \left(-Z \sqrt{\frac{v^2}{4D^2} + \frac{\lambda}{D}} \right) \right]$	$c = c_0 \exp \left[\frac{v}{2D} - \sqrt{\frac{v^2}{4D^2} + \frac{\lambda}{D}} \right] Z$	$c = c_0 e^{\frac{v}{2D} (H-Z)} \frac{\text{sh} Z \sqrt{\frac{v^2}{4D^2} + \frac{\lambda}{D}}}{\text{sh} H \sqrt{\frac{v^2}{4D^2} + \frac{\lambda}{D}}}$
(7) diffusion + transport + decay + generation	$D \frac{\partial^2 c}{\partial Z^2} - v \frac{\partial c}{\partial Z} - \lambda c + Q = 0$	$c = e^{\frac{v}{2D} Z} \left[K_1 \exp Z \sqrt{\frac{v^2}{4D^2} + \frac{\lambda}{D}} + K_2 \exp \left(-Z \sqrt{\frac{v^2}{4D^2} + \frac{\lambda}{D}} \right) \right] + \frac{Q}{\lambda}$	$c = \left(c_0 - \frac{Q}{\lambda} \right) \exp \left[\frac{v}{2D} - \sqrt{\frac{v^2}{4D^2} + \frac{\lambda}{D}} \right] Z + \frac{Q}{\lambda}$	$c = e^{\frac{v}{2D} (H-Z)} \left(c_0 - \frac{Q}{\lambda} \right) \frac{\text{sh} Z \sqrt{\frac{v^2}{4D^2} + \frac{\lambda}{D}}}{\text{sh} H \sqrt{\frac{v^2}{4D^2} + \frac{\lambda}{D}}} + \frac{Q}{\lambda} \left(1 - e^{-\frac{v}{2D} Z} \frac{\text{sh} (H-Z) \sqrt{\frac{v^2}{4D^2} + \frac{\lambda}{D}}}{\text{sh} H \sqrt{\frac{v^2}{4D^2} + \frac{\lambda}{D}}} \right)$

Table 1/a. Main data and boundary conditions for the idealized radon transport models of Table 1/b

Table 1/b. Solutions for the differential equations describing the radon transport for the two models of Table 1/a. Equilibrium in time and the presence and absence of different physical mechanisms are assumed, $c(z)$ is the vertical profile of radon concentration for the boundary conditions of the given models; K , K_1 and K_2 are constants

1/a. táblázat. Az 1/b. táblázatban használt, idealizált radon-szállítás modellek jellemző adatai és határfeltételei

1 — I. Modell: „vastag” fedő; 2 — II. Modell: „vékony” fedő; 3 — porózus közeg; 4 — felszín; 5 — érctest; 6 — határfeltételek

1/b. táblázat. A radon-transzportot leíró differenciálegyenlet megoldásai az 1/a. táblázatban vázolt két modell esetén, időbeli egyensúlyt és különböző fizikai mechanizmusok jelenlétét, ill. hiányát feltételezve. $c(z)$: a radonkoncentráció mélységprofilja az adott modellek határfeltételei között; K , K_1 és K_2 : állandók

1 — bomlás + keletkezés; 2 — diffúzió + bomlás; 3 — szállítás + bomlás;
4 — diffúzió + bomlás + keletkezés; 5 — szállítás + bomlás + keletkezés;
6 — diffúzió + szállítás + bomlás; 7 — diffúzió + szállítás + bomlás + keletkezés;
8 — Mechanizmus; 9 — Differenciál egyenlet; 10 — Általános megoldás;
11 — I. Modell szerinti megoldás; 12 — II. Modell szerinti megoldás;
13 — határfeltétel nem vehető figyelembe; 14 — csak az alsó határfeltétel vehető figyelembe

Табл. 1/a. Характерные данные и граничные условия моделей переноса радона, примененных в табл. 1/b

1 — Модель I. «мощные» наносы; 2 — Модель II «маломощные» наносы; 3 — пористая среда; 4 — дневная поверхность; 5 — руда; 6 — граничные условия

Табл. 1/b. Решения дифференциального уравнения переноса радона для моделей табл. 1/a. предполагая наличие временного равновесия при наличии и отсутствии разных физических процессов

1 — распад + образование; 2 — диффузия + распад; 3 — перенос + распад; 4 — диффузия + распад + образование; 5 — перенос + распад + образование; 6 — диффузия + перенос + распад; 7 — диффузия + перенос + распад + образование; 8 — процесс; 9 — дифференц. уравнение; 10 — общее решение; 11 — решение по модели I.; 12 — решение по модели II.; 13 — граничное условие нельзя учитывать; 14 — учитывается лишь нижнее граничное условие

velocity should be supposed. Gas bubbles passing through the water saturated uranium ore deposit and those produced by radiolysis could carry away a part of the released radon [KRISTIANSSON and MALMQVIST 1982], and could ensure the rapid transport (with total time comparable to the half-life of radon) up to the uppermost level of the continuous pore water system, the ground-water table. From the viewpoint of radon monitoring this bubble transport mechanism provides favourable conditions only if there is no geological formation (e.g. clay layer) impermeable to water or gases between the ore deposit and the water table.

The medium above the water table behaves in a different way in radon transport, the buoyant force result of specific weight differences between the gases and the pore fluid ceases to exist, and the movement of radon is determined by physical laws governing the behaviour of gases filling the pore space in a solid medium. From among the pore gas components the radon has the highest relative atomic mass, therefore in this zone the lighter components of the geogas (H₂, He) might have a higher mobility. Above the water table the diffusion can be regarded as the basic mechanism in upward movement of the radon. In what follows we make an attempt to give a quantitative description of the radon movement in a medium below and above the water table, assuming two different transport mechanisms, viz. microbubbles and diffusion.

5. Physical model for radon transport in microbubbles

The velocity of the microbubble movement in water is determined by the Stokes' law

$$v = \frac{g}{18\eta_w} (\rho_w - \rho_g)d^2 \tag{3}$$

- where g is acceleration due to gravity (cms⁻²)
- η_w is dynamic viscosity of water (gcm⁻¹s⁻¹)
- ρ_w is density of water (gcm⁻³)
- ρ_g is density of the gas in the bubbles (gcm⁻³)
- d is diameter of the spherical gas bubble (cm).

The velocity in the differential equation (1) describing the radon transport should be substituted for velocity given by Eq. (3). As the velocity is a function of depth (i.e. the coordinate z) too, this equation has no trivial solution. Namely during their upward movement the bubbles are expanding because the hydrostatic pressure is decreasing, thus the bubble velocity is increasing according to Eq. (3).

Using Boyle's gas law ($p \cdot V = \text{constant}$ at a given temperature), and the equation giving the hydrostatic pressure ($p = p_0 + \rho_w g z$)

$$v = v_0 \left(\frac{h_0}{h_0 + z} \right)^{2/3} \tag{4}$$

is obtained for the velocity of the bubbles as a function of depth, where v_0 is the velocity of the bubble at the moment of reaching the water surface (i.e. the highest value of transport velocity), h_0 is the piezometric height of a water column being in hydrostatic equilibrium with atmospheric pressure p_0 (practically 10 m). The equation is valid only in water; in rocks the velocity might be significantly lower (see Section 9).

In first approximation the terms describing the diffusion and the radon production (Q) can be neglected in Eq. (1). The validity of this assumption has already been checked for the first term [VÁRHEGYI et al. 1986], and neglecting the source term Q which describes the local radon generation does not effect basically the essentials of the solution (the solution including the term Q is discussed elsewhere [BARANYI et al. 1985]. In this case the general solution of Eq. (1) is

$$c = K(h_0 + z)^{2/3} \cdot \exp \left[\frac{3h_0\lambda}{5v_0} \left(\frac{h_0 + z}{h_0} \right)^{5/3} \right] \quad (5)$$

It is noted that z is positive downward and $z=0$ at the water table. For negative z values this equation is meaningless because above the water table the diffusion is considered to be the basic physical process of radon transport, and here the general solution of the transport equation is (see Table I)

$$c = K_1 \exp(z\sqrt{\lambda/D}) + K_2 \exp(-z\sqrt{\lambda/D}) \quad (6)$$

K , K_1 and K_2 in Eqs. (5) and (6) are arbitrary constants.

6. The depth function of radon concentration

For quantitative description of the radon transport the rock volume between the ore deposit and the surface is divided into two regions: from the ore-body up to the water table, where the pores are filled with water (medium 2), and the region between the water table and the surface without continuous water saturation (medium 1). Parameters of the model are shown in *Figure 1*. The depth change of radon concentration (radon profile) in medium 1 is given by Eq. (6), while in medium 2 by Eq. (5). Using the relevant boundary conditions we get for the radon profile in medium 1

$$c = c_0 \frac{\text{sh}(z\sqrt{\lambda/D})}{\text{sh}(h\sqrt{\lambda/D})} \quad (7)$$

and in medium 2

$$c = c_s \left(\frac{y}{y_s} \right)^{2/3} \exp \left[\frac{3h_0\lambda}{5v_0} (y^{5/3} - y_s^{5/3}) \right] \quad (8)$$

where

$$y = \frac{h_0 + z - h}{h_0} \quad \text{and} \quad y_s = \frac{h_0 + H - h}{h_0} \quad (8a)$$

If we suppose that c_0 at the water table ($z = h$) is independent of the approach direction, i.e. the same value could be obtained in media 1 and 2 (this is not trivial), then for c_0 we get

$$c_0 = c_s y_s^{-2/3} \cdot \exp \left[\frac{3h_0 \lambda}{5v_0} (1 - y_s^{5/3}) \right] \quad (9)$$

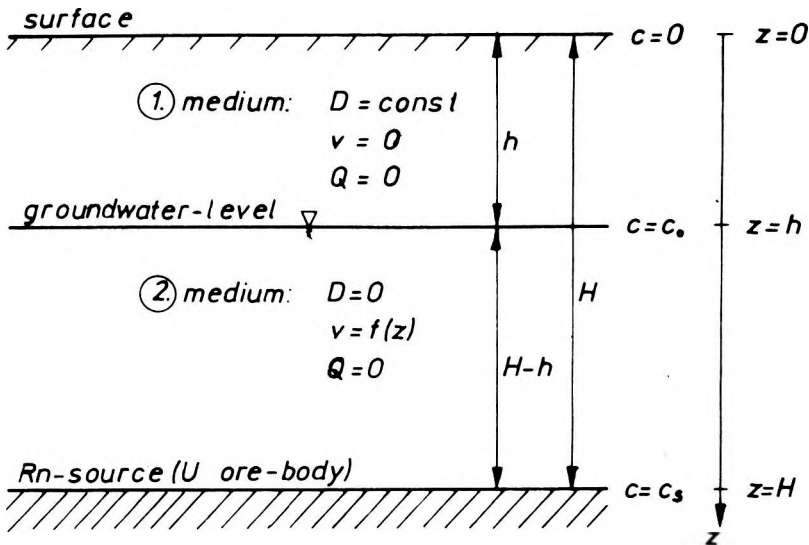


Fig. 1. Parameters used in model calculations for vertical one-dimensional radon transport in microbubbles and by diffusion

1. ábra. A mikrobuborékos és diffúziós, vertikális, egydimenziós radontranszport-modell számításaink során használt paramétereit

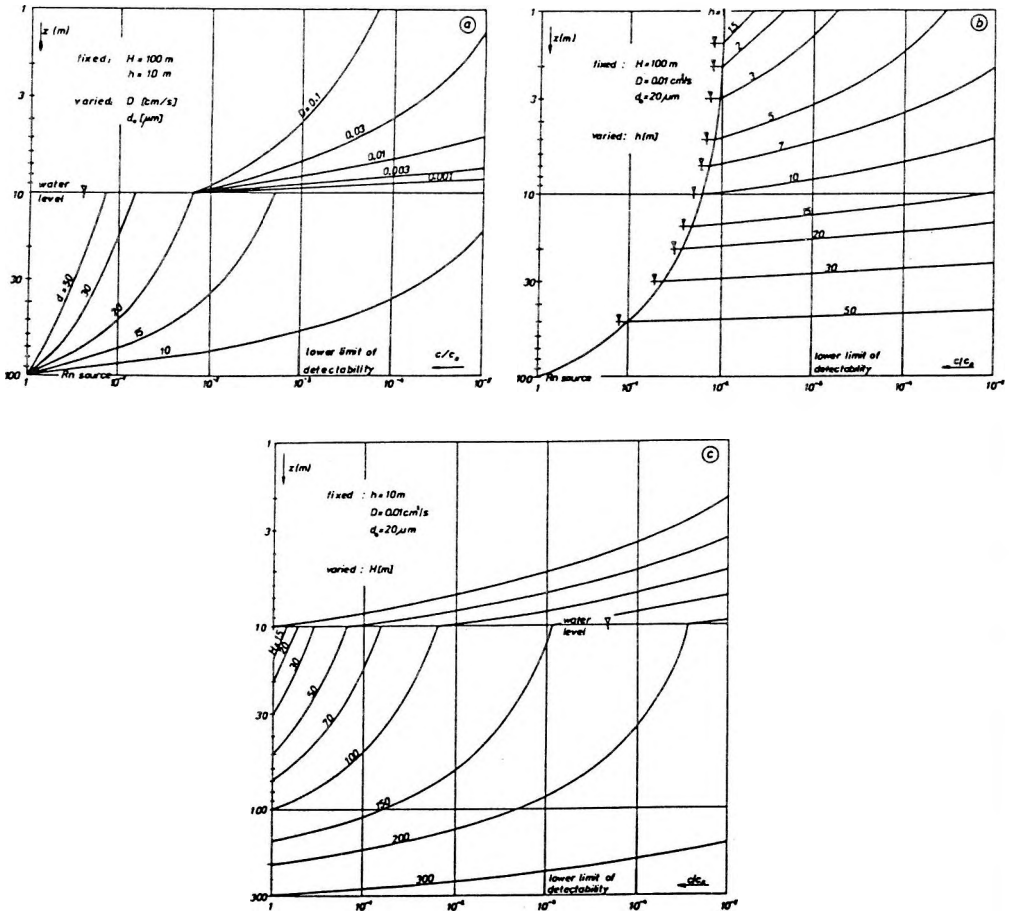
Рис. 1. Параметры, используемые нами при расчетах микропузырьковой и диффузионной моделей вертикального, одномерного переноса радона

7. Theoretical radon profiles

Theoretical profiles of the relative radon concentration c/c_s can be calculated using equations (7) to (9) for any value of D , v_0 (or using Stokes' law for the maximum bubble diameter d_0), h and H .

Of course, this form of the curves (without including the rock physical parameters) can reflect only the trend of the expected real changes. They are, however, suitable for drawing some important—sometimes unexpected and surprising—conclusions. In *Figure 2* theoretical relative radon concentration profiles are shown calculated for some arbitrarily fixed values of the parameters. In the figure the concentration range considered as practical detectability threshold (minimum of signal-to-noise ratio required) is marked. This range is determined by the radon concentrations always present in the vicinity of the monitoring site (background).

Figure 2a shows the radon profiles for different d_0 and D values if the ore-body is at the depth of 100 m and the water table at 10 m. The most striking feature of the figure is that the attenuation in the radon concentration does not exceed three orders of magnitude for bubble diameters over 15 μm if the whole 90 m below the water table is considered (because the radon being in the bubbles



relatively quickly reaches the water table). Above this level, however, up to the depth of 1 m below the surface (which is the depth generally applied in traditional track detector measurements) there is a further attenuation of more than two orders of magnitude in the radon concentration, even under the most favourable conditions.

Figure 2b shows the effect of the water table depth on the radon profile for 100 m source depth. A practically important conclusion is that for water tables deeper than a few m there is a significant attenuation in the near-surface radon concentration. At the same time in case of shallow water tables anomalous radon concentrations can be detected from deep sources with an attenuation of less than two orders of magnitude in the concentration compared to that at the source. Attempts were made to explain the temporal changes in radon concentration obtained in field measurements by the development of global subsurface flows; these attempts, however, failed in identifying the real cause of this phenomenon. A consequence of our model is that the assumption of such a mechanism is not mandatory, the phenomenon can be explained by changes in the water table.

Figure 2c shows the effect of the depth to the ore-body on the radon profile for a water table at 10 m. It can be seen that for the given parameters an anomalous radon concentration can be detected at the water table even if the source depth exceeds 150 m. Near to the surface, however, there is no chance to detect deep sources.

Fig. 2. Theoretical curves of vertical radon transport in microbubbles and by diffusion

- a) Attenuation of the relative radon concentration (c/c_s) for a source at the depth of 100 m, if the water table is at 10 m. d_0 — bubble diameter at the water table; D — diffusion coefficient of radon for medium 1; c_s — radon concentration at the source
- b) The effect of the depth to the water table (h) on the vertical radon concentration profile, assuming a maximum bubble diameter d_0 of 20 μm
- c) The effect of the source depth (H) on the vertical radon concentration profile, assuming a maximum bubble diameter of 20 μm

2. ábra. A mikrobuborékos és diffúziós, vertikális radontranszport elméleti görbéi

- a) A relatív radonkoncentráció (c/c_s) változása egy 100 m mélyen levő forrás felett, ha a talajvízszint 10 m mélyen van. d_0 — buborékátmérő a vízszintnél; D — a radon diffúziós állandója a vízszint feletti közegben; c_s — radonkoncentráció a forrásnál
- b) A talajvízszint (h) változásának hatása a mélységi radonkoncentráció-profilra, 20 μm -es maximális buborékátmérőt (d_0) feltételezve
- c) A forrásmélység (H) hatása a mélységi radonkoncentráció-profilra, 20 μm -es maximális buborékátmérőt feltételezve

Рис. 2. Теоретические кривые микропузырькового и диффузионного, вертикального переноса радона

- a) Изменение относительной концентрации радона (c/c_s) над источником на глубине 100 м при залегании уровня грунтовой воды на глубине 10 м. d_0 — диаметр пузыря на уровне воды; D — постоянная диффузии радона в среде над уровнем воды; c_s — концентрация радона у источника
- b) влияние изменения уровня грунтовой воды (h) на профиль глубинной концентрации радона при предположении максимального диаметра пузыря, равного 20 мкм (d_0)
- c) влияние глубины источника (H) на профиль глубинной концентрации радона при предположении максимального диаметра пузыря, равного 20 мкм

8. Theoretical track production profiles for radon measurements with track detectors

Theoretical vertical concentration profiles from the ore-body up to the water table have been shown for radon carried by "geogas" bubbles for different boundary conditions. Using the track detector radon measuring technique, however, the track production is not proportional to the radon content because of the pressure changes in the cup placed into the water. The pressure in the sensitive volume of the cup is obviously in equilibrium with the sum of the actual hydrostatic (p) and atmospheric pressures. Consequently the track production efficiency of the detector changes according to

$$\frac{R}{R_s} = \frac{p_s}{p} = \frac{h_0 + H - h}{h_0 + z - h} \quad (10)$$

because of the pressure dependence of the range of alpha particles in air (R). The relationship between the measured track density and the radon concentration is

$$\frac{Q}{Q_s} = \frac{P_s}{p} \cdot \frac{c}{c_s} \quad (11)$$

Finally, using Eqs. (11) and (8), the theoretical track density profile for the configuration of Figure 1 is

$$\frac{Q}{Q_s} = \left(\frac{y}{y_s}\right)^{-1/3} \exp\left[\frac{3h_0\lambda}{5v_0}(y^{5/3} - y_s^{5/3})\right] \quad (12)$$

One of the remarkable features of Eq. (12) is that it has a minimum at a depth of z_{min} if certain boundary conditions are met. The minimum can be found at the depth of

$$z_{min} = h + h_0 \left[\left(\frac{v_0}{3h_0\lambda} \right)^{3/5} - 1 \right] \quad (13)$$

below the surface.

This equation is valid only between h and H . If $v_0 \leq 0.23 \text{ mh}^{-1}$ no minimum might be expected. We have observed a minimum in the track density profile measured in a 270 m deep borehole [SOMOGYI and LÉNÁRT 1985].

Figure 3a shows a typical set of track density profiles calculated using equation (12) and assuming different bubble diameters at the water table. It is worth mentioning that for fixed initial conditions (water depth, bubble size) the track density profiles depend on water temperature through viscosity as well. Results of calculations about this phenomenon are shown in Figure 3b. It is obvious from the figure that our model results in higher radon concentrations at the surface of thermal springs.

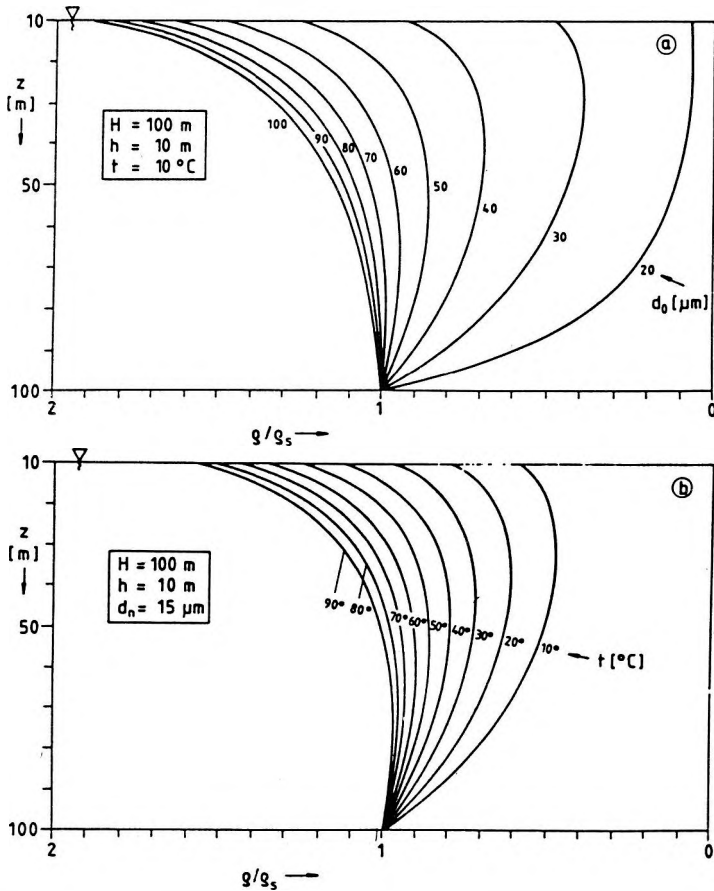


Fig. 3. Theoretical track density (Q/Q_s) – depth (z) profiles below the water table for an alpha-sensitive track detector and for vertical radon transport in microbubbles
 a) assuming “geogas” bubbles of different diameter and a water temperature of 10 °C
 b) as a function of water temperature, if the initial diameter of “geogas” bubbles is identical (15 μ m)

3. ábra. Alfa-részecskékre érzékeny nukleáris nyomdetektorral mérhető relatív nyomsűrűség (Q/Q_s) elméletileg várható változása a vízszint alatt mért mélység függvényében, mikrobuborékos, vertikális radontranszport esetén

- a) Különböző átmérőjű „geogáz” buborékokat és 10 °C-os vizet feltételezve
- b) Különböző hőmérsékletű vizekben, ha a „geogáz” mikrobuborékok kezdeti átmérője azonos (15 μ m)

Рис. 3. Теоретически ожидаемое изменение относительной плотности следов (Q/Q_s), измеряемых при помощи чувствительного к α -частицам ядерного детектора в зависимости от глубины под уровнем воды при микропузырькового вертикального переноса радона
 а) при предположении пузырей «геогаза» с различными диаметрами и температуры воды, равной 10 °C
 б) в водах при различных температурах при одинаковом исходном диаметре микропузырьков «геогаза» (15 мкм)

9. Role of petrophysical parameters in radon transport

In order to describe the radon transport in microbubbles under realistic geological conditions using Eqs. (7) to (9) some connection should be found between the variables in the equations and the rock physical parameters. Because of the significant spatial changes in the rock physical parameters this connection could be a trend only, established by statistical approach. In this way, however, it is possible to determine clearly the direction and measure of the effects of the individual rock properties on the radon transport. Rock physical parameters can be introduced into the equations describing the radon transport through the diffusion coefficient D , the concentration at the source c_s , and the maximum bubble velocity v_0 (or using Stokes' law through the maximum bubble diameter d_0). The role of D and c_s is not dealt with in the present paper, these topics have already been thoroughly and widely discussed in the literature [e.g. TANNER 1964]. In what follows we make some comments of conceptual importance only concerning the connection between the rock structure and bubble velocity.

9.1 Role of tortuosity and porosity

In our description of the radon transport the diameter of the microbubbles d and their upward flow velocity v have been connected in first approximation by Stokes' law (3). The Stokes' law, however, in this form applies only to the flow of bubbles in a fluid, and therefore it cannot take into account that in rocks this flow might occur along forced trajectories only, namely through the inter-connected fissure and pore system of rocks. The sinuosity of actual flow paths in rocks is expressed by the rock physical parameter of tortuosity (t). Using the tortuosity the upward component of the bubble velocity is given by

$$v_{\uparrow} \leq \frac{v}{t^2}. \quad (14)$$

It should be noted, however, that because of the narrowing of the flow paths at several places and adhesion forces between the pore wall and the bubble some of the bubbles might get stuck for longer times, their flow might slow down or they might be disintegrated into smaller bubbles. These effects might cause a further significant decrease in the resulting velocity. Therefore a wide distribution of velocities should be visualized, where Eq. (14) gives the upper limit of velocities only.

The vertical bubble velocity can be expressed by the porosity ε , which can be measured more easily than t . For loose sediments the relation between the tortuosity and porosity is given by a simplified form of Archie's formula

$$t^2 \cong \frac{1}{\sqrt{\varepsilon}} \quad (15)$$

Thus the vertical velocity component can be related to that obtained by using Stokes' law by

$$v_{\uparrow} \leq \sqrt{\varepsilon} \cdot v. \quad (16)$$

9.2 Role of grain size distribution

There is a parameter of more or less unknown value in Stokes' velocity function, the bubble diameter. The maximum value of that is somehow related to the texture of the rock. It is obvious that the narrowest cross section of the pore paths provides an upper limit for the bubble diameter. In fractured rocks (where the bulk of pore volume consists of an interconnected system of fractures and fissures, e.g. in fault zones) the size of the bubbles is determined supposedly by the minimum spatial dimension of the interconnected fracture system.

For porous rocks consisting of grains (e.g. sand, sandstone) an idealized model of the matrix structure should be used in the theoretical investigation of this question. Let us suppose an equigranular grain size distribution, i.e. it might be characterized by a single parameter, by grain diameter D_m (D_m may be called mean grain size as well). For this case the two extreme states, the possible loosest and most dense fills are shown in *Figure 4*. The real case might be somewhere between these two extremes. Anyway, the two limits of the largest bubbles that can pass through the grains and the two concrete values of rock porosity shown in *Figure 4* can be assigned to these two extreme cases [EGERER 1977]. Taking the origin of the ε - d coordinate system as a third point to the previously mentioned two points (obviously, if there is no porosity there are no bubbles) a parabola can be fitted arbitrarily to these three points which is described by

$$d = 1.26 D_m \varepsilon (\varepsilon + 0.21). \quad (17)$$

Using equations (16) and (17), and the Stokes' formula (3) — accepting the idealized conditions and other assumptions — a relationship could have been derived between the velocity v_0 in Eq. (8) describing the radon transport, and rock physical parameters. After all, for porous water-saturated rocks the bubble velocity (or its maximum value) could be traced back to two simple rock properties, the porosity and the mean grain diameter D_m :

$$v_0 \leq 0.088 \frac{g}{\eta_w} (\rho_w - \rho_g) \varepsilon^{5/2} (\varepsilon + 0.21)^2 D_m^2 \quad (18)$$

Two comments should be made on equation (18):

- (1) The velocity determined this way should be considered only as a maximum value, because of the reasons mentioned above. Only the "most lucky" bubbles may gain this velocity, but these might carry the bulk of the radon.
- (2) We have investigated the effect of the mean grain diameter D_m only for equigranular grain distribution, and this can be found only rarely in nature. The relation between D_m and the actual grain size distribution is very

difficult to investigate theoretically. It is probable, however, that in case of a wide grain size distribution D_m is shifted towards the finer grain sizes (the space between the larger grains is filled in with the smaller ones, thus the cross section available for bubble flow is reduced).

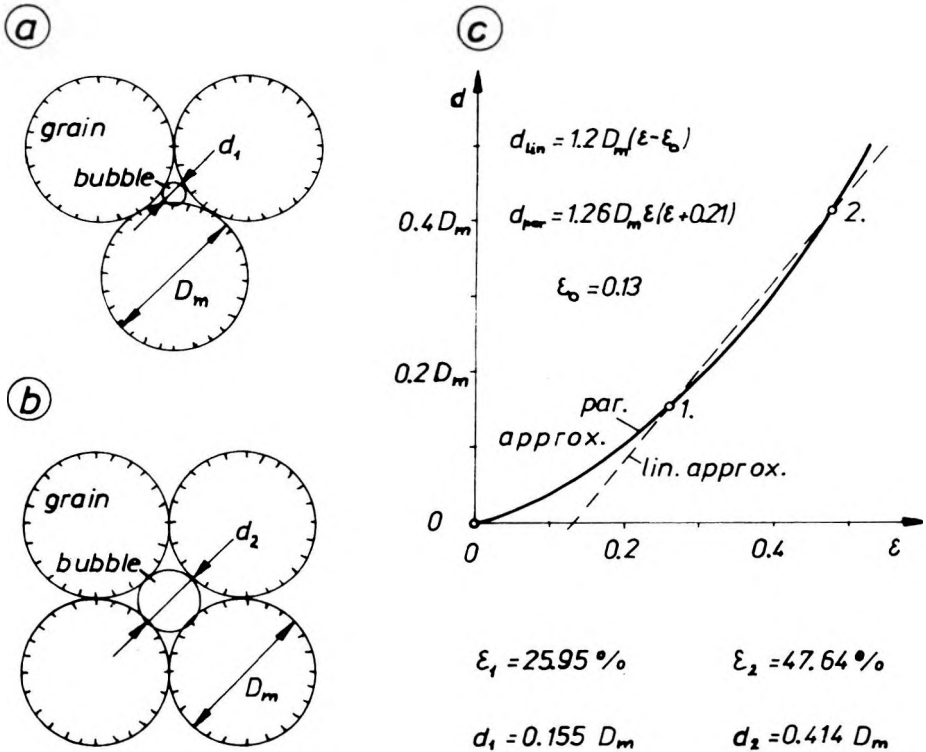


Fig. 4. The relationship between the possible maximum bubble diameter (d) and rock porosity (ϵ) for

- a) the most dense; b) the loosest fill, assuming an equigranular grain size (D_m) distribution;
- c) parabolic approximation of the $d(\epsilon)$ function

4. ábra. A lehetséges maximális buborékátmérő (d) és a kőzetporozitás (ϵ) kapcsolata a legszorosabb és b) leglazább szemcseilleszkedésnél, ekvigranuláris szemcseméret (D_m)-eloszlást feltételezve; c) a $d(\epsilon)$ függvény parabolikus közelítése

Рис. 4. Связь между максимальным диаметром пузыря (d) и пористостью породы (ϵ) при самом плотном а) и самом рыхлом б) прилегании зерн при предположении эквигранулярной зернистости (D_m); в) аппроксимация функции $d(\epsilon)$ параболой

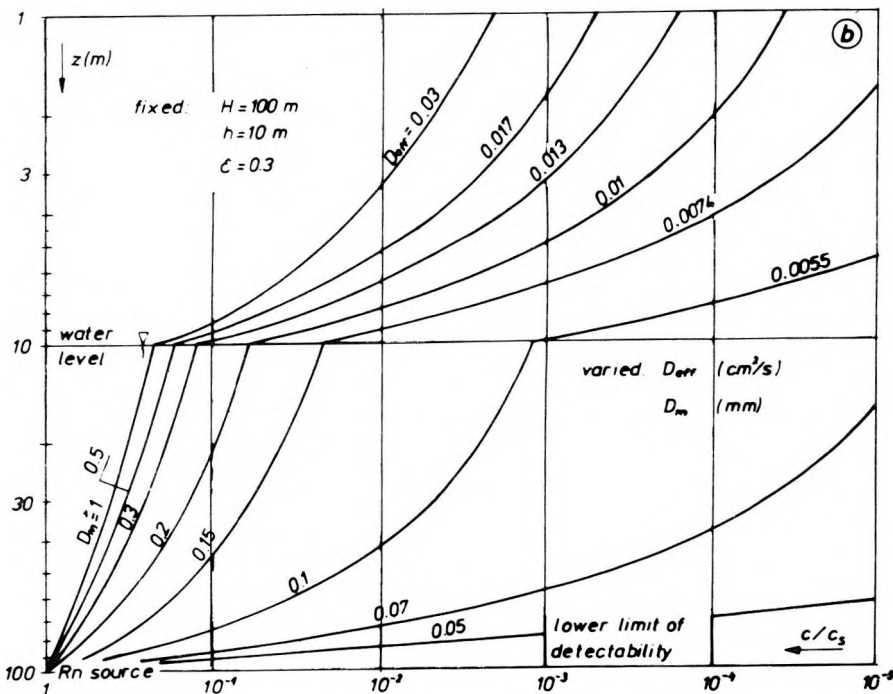
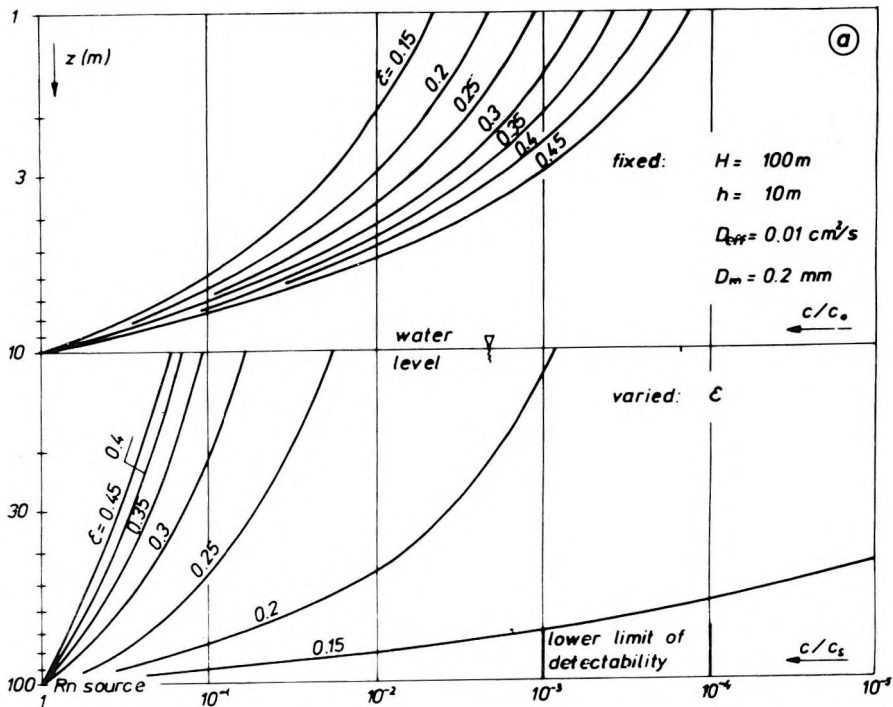
10. Theoretical radon profiles in porous rocks

The concentration profile calculated using equations (8) and (18) is shown in *Figure 5*. Here only the water saturated rock region (below the water table) is discussed.

The effect of rock porosity on the radon profile can be studied in *Figure 5/a*. In calculation of the curve set the following parameters were fixed: depth to the ore-body below the water table is 100 m; the mean grain diameter is 0.2 mm. It can be seen clearly that the radon profile is practically insensitive to variations in porosity for the given parameters and for porosities over 35%. For porosities lower than 20%, however, the radon concentration significantly attenuates with distance from the source.

Figure 5/b shows the effect of the grain mean diameter D_m on the radon profile (fixed parameters: $H = 100$ m, $\varepsilon = 0.3$) For grain diameters above 1 mm variations in D_m have no effect on the radon profile (this includes the extreme case of $D_m \rightarrow \infty$, i.e. the medium is water alone, if there is no other factor reducing the bubble size). It can be seen that down to $D_m = 0.2$ mm the decrease in the grain diameter does not effect significantly the radon concentration. Any further decrease in D_m , however, dramatically reduces the radon transport.

Based on the diagrams shown it seems that — assuming a radon transport in microbubbles — there is no practical possibility for detection of radon concentration anomalies due to deep sources if the overburden has a low effective porosity ($\varepsilon < 20\%$) and/or a small mean grain diameter ($D_m < 0.1$ mm) (e.g. mud, silt, clay, loess, etc.). Exceptions are the cases when other favourable properties of the rock structure (vertical fracturing, fault zone, etc.) provide other channels for radon transport. In porous ($\varepsilon > 25\%$) rocks of coarse grain size ($D_m > 0.2$ mm) and/or in rocks with macrofractures, along fractured and water saturated fault zones — at least at or near to the water table — the chances for detecting deep radon sources are excellent.



11. Practical recommendations

No doubt, coincidence of several favourable geological conditions is required for effective operation of radon transport in microbubbles from the viewpoint of uranium exploration. The presence of a high enough geogas flux and water saturated, loose porous rocks and the absence of layers impermeable to gases are all prerequisites. In favourable cases, however, mineralizations at depths of a few hundred meters can be detected by radon measurements, as has been demonstrated by several case histories.

According to our model calculations the radon, as one of the components of geogas flowing upward in microbubbles, reaches the water table at relatively high velocity. Its further movement towards the surface is, however, controlled by the "slow" diffusion. Therefore when the water table is at depths of several meters below the surface, detectors traditionally placed near to the surface cannot detect the radon from deep sources (Figure 2). Nevertheless, using shallow drill holes the radon monitors might be placed near to the water table and the detectability of deep radon sources could be improved by several orders of magnitude. The increase in exploration costs and a better chance for detecting deeper mineralizations are factors of opposite effect and an optimum should be found by strategical considerations.

The authors have developed a research technology and exploration tools based on the transport theory described. This technology has been routinely applied in uranium exploration in Hungary since 1983. BARANYI et al. [1985] have also published some practical results in addition to an experiment directly demonstrating the validity of the "geogas" bubble model [SOMOGYI and LÉNÁRT 1985].

Fig. 5. A theoretical approach to the connection between the vertical radon transport in microbubbles and petrophysical parameters, assuming a porous rock matrix consisting of grains.

- a) Effect of effective rock porosity (ϵ) on radon concentration profiles
- b) Effect of the mean grain size (D_m) on radon concentration profiles

5. ábra. A mikrobuborékos, vertikális radontranszport és a kőzetfizikai paraméterek kapcsolatának elméleti megközelítése, szemcsés-porózus kőzetstruktúrát feltételezve.

- a) A kőzetek effektív porozitásának (ϵ) hatása a radonkoncentráció-profilra
- b) A kőzetek mértékadó szemcseátmérőjének (D_m) hatása a radonkoncentráció-profilra

Рис. 5. Теоретическая аппроксимация связи микропузырькового вертикального переноса радона с физическими параметрами пород при предположении зернисто-пористой структуры породы

- a) влияние эффективной пористости (ϵ) пород на профиль концентрации радона
- b) влияние преобладающего диаметра зерн (D_m) пород на профиль концентрации радона

REFERENCES

- BARANYI I., GERZSON I., VÁRHEGYI A. 1985: A new hypothesis of radon migration and its practical application in the emanation exploration method of uranium occurrences (in Hungarian). *Magyar Geofizika*, **26**, 5–6, pp. 226–232
- BECK L. S., GINGRICH J. E. 1976: Track etch orientation survey in the Cluff lake area, Northern Saskatchewan. *CIM. Bulletin*, **69**, pp. 104–109
- CLEMENTS W. E., WILKENING M. H. 1974: Atmospheric pressure effects on Rn-222 transport across the earth-air interface. *J. Geophys. Res.*, **79**, 33, pp. 5025–5029
- EGERER F. 1977: Physics of rocks (in Hungarian). Tankönyvkiadó. Budapest, 224 p.
- FLEISCHER R. L., MOGRO-CAMPERO A. 1978: Mapping of integrated radon emanation for detection of long-distance migration of gases within the earth: Techniques and principles. *J. Geophys. Res.*, **83**, B7, pp. 3539–3549
- GINGRICH J. E. 1975: Results from a new uranium exploration method. *Transaction of SME.*, **258**, pp. 61–64
- GINGRICH J. E. 1984: Radon as a geochemical exploration tool. *J. Geochem. Explor.*, **21**, 1, pp. 19–39
- GINGRICH J. E., FISHER J. C. 1976: Uranium exploration using the track-etch method. *IAEA-SM-208/19*, pp. 213–224
- GRAMMAKOV A. G. 1936: On the influence of some factors in the spreading of radioactive emanations under natural conditions (in Russian). *Zhur. Geofiziki*, **6**, pp. 123–148
- KRISTIANSSON K., MALMQVIST L. 1982: Evidence for nondiffusive transport of $^{222}_{86}\text{Rn}$ in the ground and a new physical model for the transport. *Geophysics*, **47**, 10, pp. 1444–1452
- KRISTIANSSON K., MALMQVIST L. 1984: The depth-dependence of the concentration of $^{222}_{86}\text{Rn}$ in soil gas near the surface and its implication for exploration. *Geoexploration*, **22**, pp. 17–41
- LIKES R. S., MOGRO-CAMPERO A., FLEISCHER R. L. 1979: Moisture-intensive monitoring of radon. *Nucl. Instr. Meth.*, **159**, 2–3, pp. 395–400
- MALMQVIST L., KRISTIANSSON K. 1984: Experimental evidence for an ascending microflow of geogas in the ground. *Earth Planet. Sci. Lett.*, **70**, 2, pp. 407–416
- MALMQVIST L., KRISTIANSSON K. 1985: A physical mechanism for the release of free gases in the lithosphere. *Geoexploration*, **23**, 4, pp. 447–453
- SOMOGYI GY., MEDVECZKY L., VARGA Zs., GERZSON I., VADOS I. 1978: Field macroradiography measuring radon exhalation. *Isotopenpraxis*, **14**, 10, pp. 343–347
- SOMOGYI GY., NÉMETH G., PÁLFAI J., GERZSON I. 1982: Subsurface radon-distribution measurements with LR-115, CR-39 and TL-detectors. *Solid State Nucl. Track Det.*, Proc. 11th. Int. Conf., Bristol, 1981., P. H. Fowler and V. M. Clapham eds., Pergamon Press, pp. 525–529
- SOMOGYI GY., VARGA Zs., PARIPÁS B. 1983: Measurement of radon, radon daughters and thoron concentrations by multi-detector devices. *The Nucleus*, **20**, pp. 51–55
- SOMOGYI GY., LÉNÁRT L. 1985: Time-integrated radon measurements in spring and well waters by track technique. Presented at 13th Int. Conf. on Solid State Nucl. Track Det., Rome, 23–27. Sept. 1985
- SUGISAKI R., IDO M., TAKEDA H., ISOBE Y., HAYASHI Y., NAKAMURA M., SATAKE H., MIZUTANI Y. 1983: Origin of hydrogen and carbon dioxide in fault gases and its relation to fault activity. *J. Geol.*, **91**, pp. 239–258
- TANNER A. B. 1964: Radon migration in the ground — a review. *The Natural Radiation Environment*, J. A. S. Adams and W. M. Lowder eds., University of Chicago Press, pp. 161–190
- TITOV V. K., VENKOV V. A., AVDEEVA T. L., KUVSHYNNIKOVA E. J. 1985: Expositional emanation methods for exploration of mineral resources (in Russian). Nedra, Leningrad, 132 p.
- VÁRHEGYI A., BARANYI I., SOMOGYI GY. 1986: A model for the subsurface vertical transport of radon carried by geogas microbubbles (in Hungarian). *Izotóptechnika* **29**, pp. 73–104
- VOYTOV G. I. 1974: Evaluation of the intensity of gas-exchange on shield terrains (some examples from the Ukrainian shield) (in Russian). *Geol. Zs.*, **34**, 2, pp. 78–85
- VOVK I. F. 1981: Radiolitic model for the composition of solutions in the crystalline basement of shields (in Russian). *Geokhimiya*, **26**, pp. 467–480
- WARD W. J., III., FLEISCHER R. L., MOGRO-CAMPERO A. 1977: Barrier technique for separate measurement of radon isotopes. *Rev. Sci. Instrum.*, **48**, 11, pp. 1440–1441

GEOGÁZ MIKROBUBORÉKOK SEGÍTSÉGÉVEL MEGVALÓSULÓ FELSZÍNALATTI, VERTIKÁLIS RADON-SZÁLLÍTÁS MODELLJE

VÁRHEGYI András, BARANYI István és SOMOGYI György

A nagy mélységekből mikrobuborékok formájában feláramló „geogáz” jelenségére alapozva a szerzők a mélységi forrásból származó radon szállításának és kimutatásának egy új modelljét dolgozták ki. Az új modell előnye az eddigiekkel szemben, hogy segítségével feloldhatók az emanációs kutatómódszer ismert problémái (lehatolási mélység, reprodukálhatóság stb.), és a szállítási mechanizmusra földtani–fizikai szempontból reális, kvalitatív és kvantitatív leírást ad. A szerzők kiemelik a felszínalatti vizek és a mélyben keletkező gázok szerepét a radon migrációjában, röviden utalva utóbbiak lehetséges eredetére. Áttekintik a vízszint alatti nyomdetektoros radonkimutatás problémáit, és részletesen megvizsgálják egyes közetfizikai paraméterek (tortuozitás, porozitás, szemcseméret-eloszlás) és a szállítási jellemzők kapcsolatát. Különböző földtani körülmények és közetfizikai paraméterek feltételezésével elméleti úton számított mélységi radonkoncentráció és nyomdetektoros alfa-nyomsűrűség szelvényeket mutatnak be. Végül elemzik, hogy milyen földtani körülmények esetén van esély nagy mélységű radonforrás kimutatására, és új módszertani ajánlásokat tesznek az emanációs urán kutatómódszer hatékonyabb alkalmazására.

МОДЕЛЬ ПОДЗЕМНОГО ВЕРТИКАЛЬНОГО ПЕРЕНОСА РАДОНА, ОСУЩЕСТВЛЯЕМОГО С ПОМОЩЬЮ МИКРОПУЗЫРЕЙ ГЕОГАЗА

Андраш ВАРХЕДИ, Иштван БАРАНИ и Дёрдь ШОМОДИ

Авторами разработана новая модель переноса и детектирования радона, образовавшегося из глубоких источников, на основании явления «геогаза», поднимающегося с больших глубин в виде микропузырей. Достоинство новой модели заключается в том, что с его применением исчезают известные проблемы эманационного способа (глубинность исследования, повторяемость и др.) а модель переноса дает с геолого-геофизической точки зрения реальное качественное и количественное описание процессов. Авторами подчеркивается роль в миграции радона подземных вод и образовавшихся в глубине газов, с краткой ссылкой на их возможную генетику. Рассматриваются проблемы детектирования радона под уровнем воды, и детально изучается связь между характеристиками переноса и петрофизическими параметрами (извилистость, пористость, распределение размеров зерн). Показаны рассчитанные глубинное содержание радона и профили густоты альфа-следов при предположении разных геологических обстановок и петрофизических параметров. Анализируется, что при какой геологической обстановке имеется возможность детектировать глубинные источники радона, даются новые методические рекомендации для повышения эффективности эманационного поиска урана.



EARTHQUAKES IN THE REGION OF KOMÁROM, MÓR AND VÁRPALOTA

Gyöző SZEIDOVITZ*

Based on the observations of the last few centuries the direct surroundings of Komárom, Mór and Várpalota proved to be one of the most active areas of Hungary. With the assumption that the average seismicity of the area under investigation will not change significantly in the future the seismic risk of the area has been calculated using the method of CORNELL [1968].

Keywords: earthquakes, seismicity, seismic risk, Hungary

1. Introduction

The reason for investigating the three settlements mentioned in the headline together is that the earthquakes in this region have often occurred very near (within a year) to each other (for locality names see Fig. 6). During the last hundred years the region was not exposed to earthquakes. However, if a longer period is considered, it can be concluded that this is one of the most active regions of Hungary. Thus in the light of the most recent progress in earthquake re-evaluation [SZEIDOVITZ 1984] it is justified to discuss the intensity, magnitude and frequency of earlier and expected earthquakes in the region.

The earthquake causing devastation in Komárom in 1599 originated most likely in the area of our investigation. Not too much is known on that earthquake and even the epicentre is uncertain. After about 150 years of seismic inactivity two smaller earthquakes, hardly causing any damage to buildings, were observed in Komárom in 1757 and 1759. The activity of seismic source(s) in the region of Komárom had been increasing and reached its peak in 1763, when the earthquake causing the biggest devastation ever observed in Hungary broke out. This paper does not discuss the damage in detail, but refers to such descriptions [RÉTHLY 1952, SZEIDOVITZ 1984]. The main shock was introduced by continuously repeating foreshocks from 2 o'clock in the morning of 28th June 1763 and probably this was the reason for the relatively low number of casualties (63) compared to the devastation caused by the main shock between 5° and 6° in the morning (local time). The biggest damage was caused near Komárom in the settlements of the triangle between the rivers Vág and Danube (*Fig. 1*). The intensity of the earthquake in the epicentre reached 8.5° on the

* Department of Seismology, Geod. and Geophys. Res. Inst. Hung. Ac. Sci.
Meredek u. 18, Budapest H-1112, Hungary
Manuscript received (revised form): 15 April, 1986

MSK scale. The earthquake was detected on a large area (Fig. 2) and smaller or bigger building damages were caused even in Buda and Pest. Mainly dwelling houses and churches were damaged in the Castle district of Buda. Damaged buildings are marked with numerals in Fig. 3, and in the Appendix of the paper a short description of the damages is given. The main shock was followed by several aftershocks, but not too much is known on the intensity and source of them. They probably caused further damage to some of the buildings.

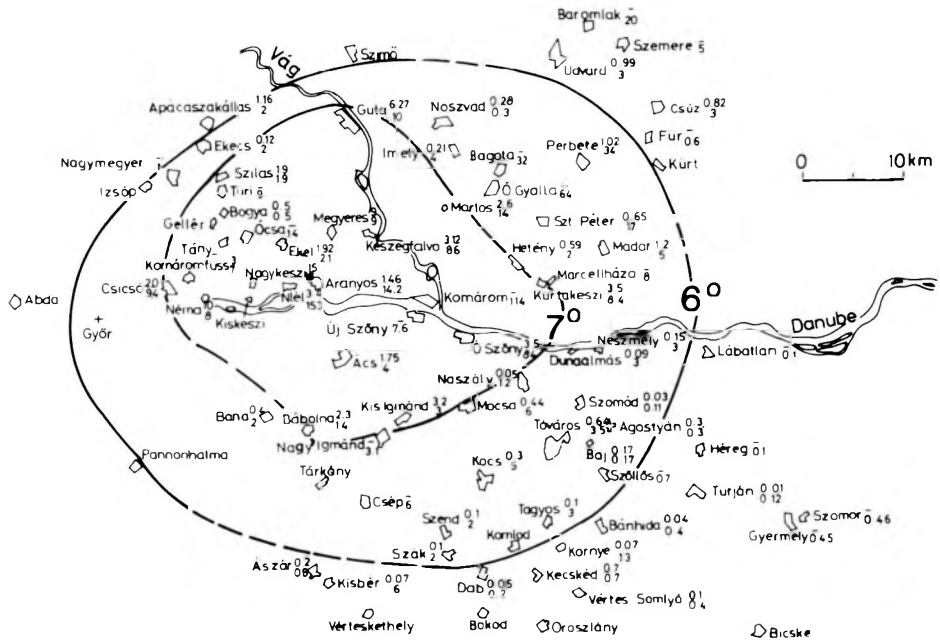


Fig. 1. Epicentral area of the Komárom earthquake of 28 June, 1763 with the 6° and 7° isoseism

Ács 1,75 — damage to one taxpayer's house, in Forint
 Ács 4 — total damage to one building, in Forint

1. ábra. Az 1763. június 28-i komáromi földrengés epicentrális területe a 6°-os és 7°-os izoszeiták feltüntetésével

Ács 1,75 — egy adózó házra eső kár (Ft)
 Ács 4 — egy épületre eső összes kár (Ft)

Рис. 1. Эпицентральная часть комаромского землетрясения 28-ого июня 1763 г. и изосейсы 6° и 7°

Ács 1,75 — средний ущерб на одного дома-налогоплателщика (форинт)
 Ács 4 — суммарный ущерб на одного здания (форинт)

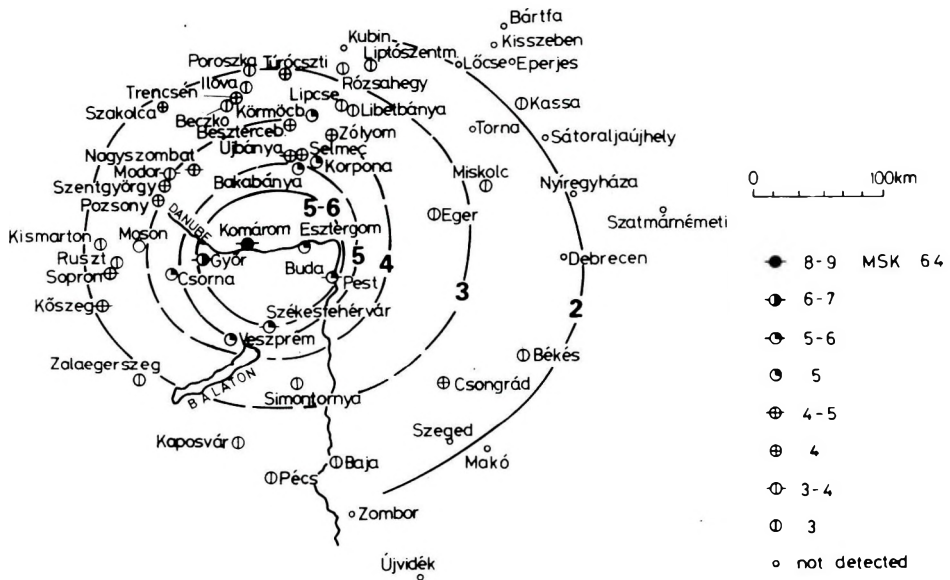


Fig. 2. Isoseisms of the Komárom earthquake of 28 June, 1763

2. ábra. Az 1763. június 28-i komáromi földrengés izoseizmitái

Рис. 2. Изосейсы комаромского землетрясения 28-ого июня 1763 г.

The activity of the source gradually decreased then, after a few years of seismic inactivity, an earthquake causing a major devastation occurred in 1783, ruining 500 houses in Komárom [SZEIDOVITZ 1984], however, the intensity of this earthquake was not as high as that of the 1763 one. The earthquake was detected on a relatively large area (isoseisms are shown on Fig. 4). The region of Komárom remained active for some time and some smaller earthquakes causing damage to buildings were registered until 1851. From the middle of the last century the seismicity reduced and in our century only a few smaller earthquakes showed the activity of the region.

Mór and its surroundings — mainly Isztimér — is not as active as the region of Komárom, but earthquakes causing heavy damage to buildings and casualties have already been observed. The first earthquake in the region of Mór was observed in 1763. This earthquake did not cause damage to buildings, the intensity in the epicentre probably did not exceed 5°. After 47 years without any seismic event, an earthquake of 8° intensity occurred in 1810. As has been proven by recent investigations, the epicentre of the earthquake was nearer to Isztimér. Several papers have been published on this earthquake [RÉTHLY 1952, SIMON 1932, SZEIDOVITZ 1984] but in spite of this hardly anything is known on the numerous aftershocks. Isoseisms of the earthquake are of a deformed ellipse shape with the principal axis parallel with the line connecting Mór and Isztimér

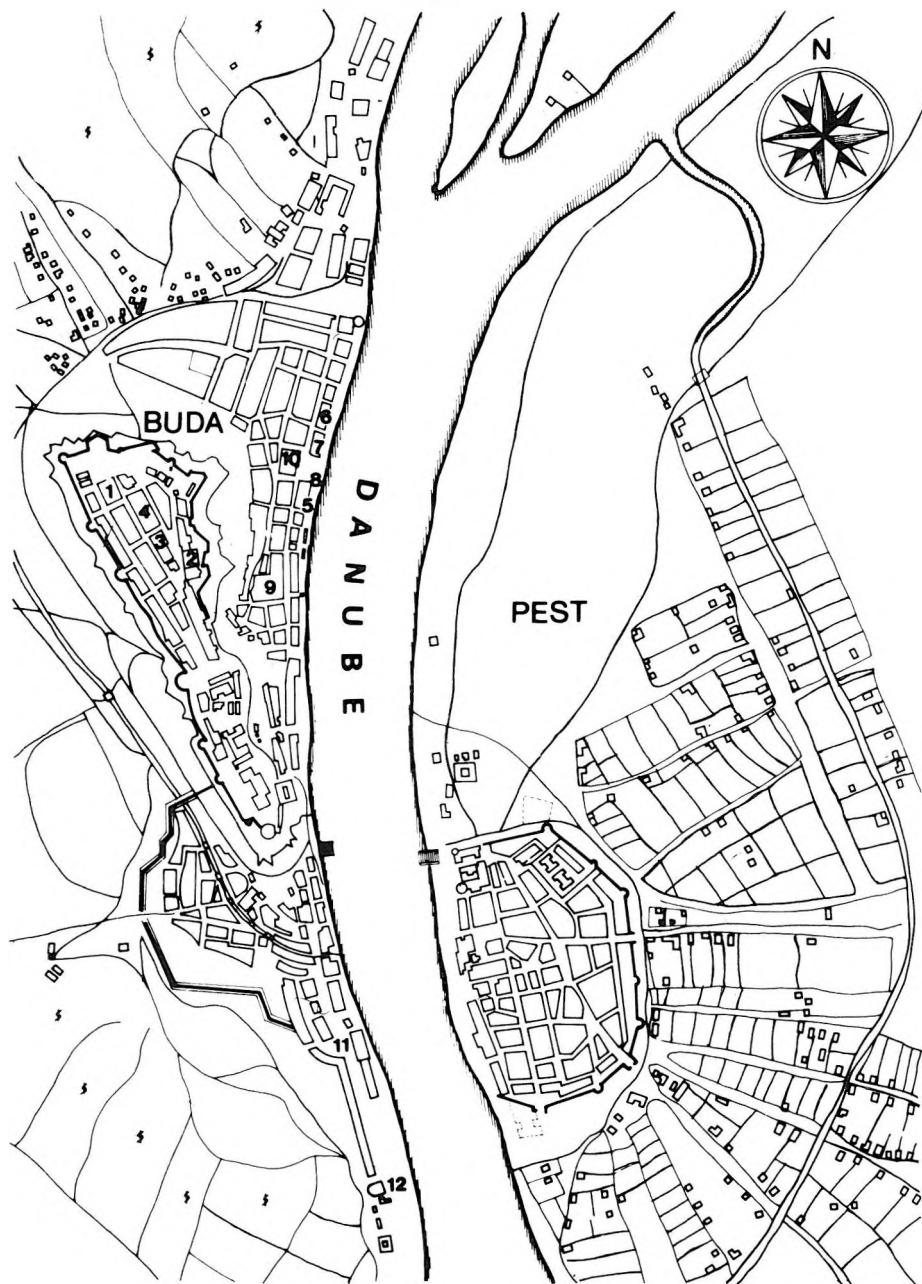


Fig. 3. Building damages at Buda caused by the Komárom earthquake of 28 June, 1763

3. ábra. Az 1763. június 28-i komáromi földrengés által okozott épületsérülések Budán

Рис. 3. Разрушение зданий на Буде в связи с комаромским землетрясением 28-ого июня 1763 г.

(Fig. 5). After the big earthquake the source remained active but since 1810 only smaller earthquakes were observed without any damage to buildings.

The wider environs of the Komárom and Mór source area are also active (Fig. 6). In the ± 5 km band along the line between Várpalota and Komárom, where the settlements of Nagyigmánd, Szend, Dad, Bakonysárkány, Aka, Mór and Isztimér are situated, smaller or bigger shocks were observed.

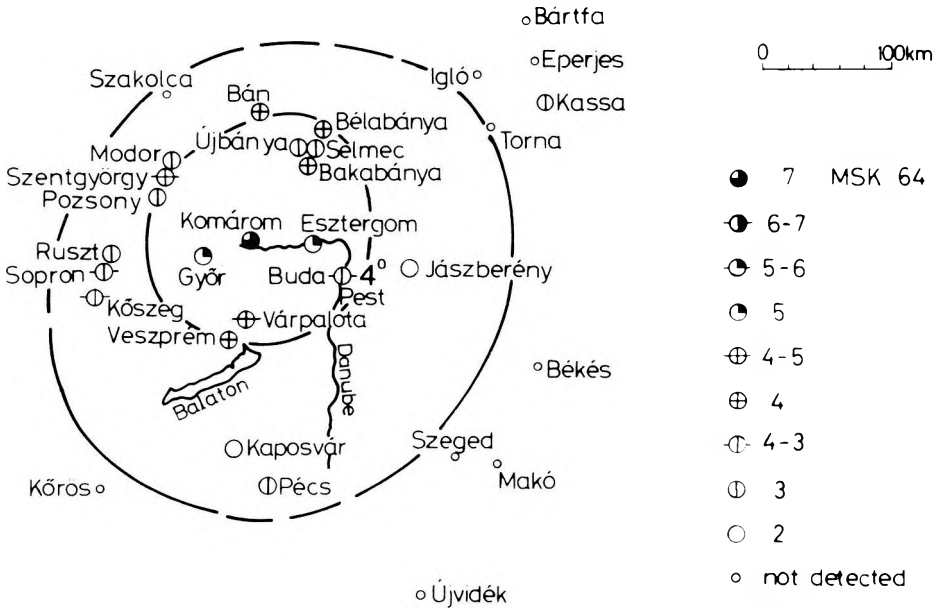


Fig. 4. Isoseism of the Komárom earthquake of 22 April, 1783

4. ábra. Az 1783. április 22-i komáromi földrengés izoszeiztái

Рис. 4. Изосейсы комаромского землетрясения 22-ого апреля 1783 г.

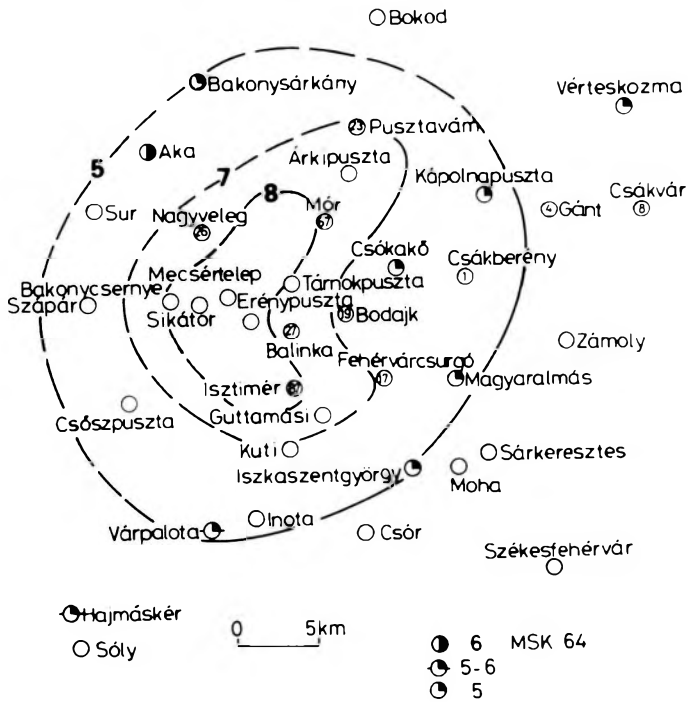


Fig. 5. Isoseisms of the Mór earthquake of 14 January, 1810
 (87) — damage to one taxpayer's house, in Forint

5. ábra. Az 1810. január 14-i móri földrengés izoszeiztái
 (87) — egy adózó házra eső kár (Ft)

Рис. 5. Изосейсы морского землетрясения 14-ого января 1810 г.
 (87) — ущерб на одного дома-налогоплательщика (форинт)

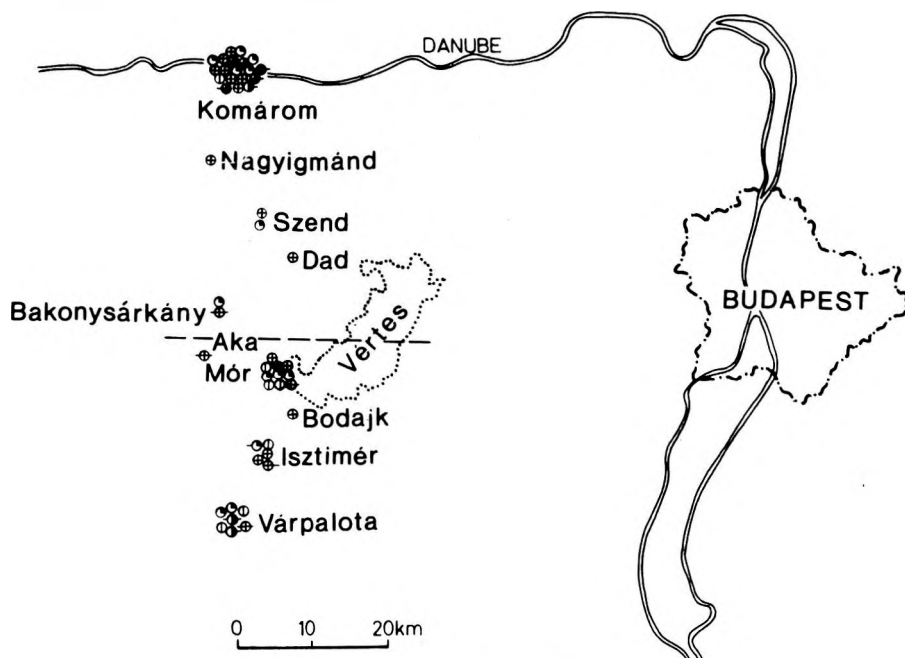


Fig. 6. Seismicity of Várpalota-Mór-Komárom

6. ábra. Várpalota-Mór-Komárom szeizmicitása

Рис. 6. Сейсмичность окрестности гг. Варпалота-Мор-Комаром

2. Theory of calculating seismic risk

According to accepted and proposed procedures [CORNELL 1968], it is assumed that the seismicity of a region is more or less constant, i.e. the seismic activity observed in the past is not going to change significantly in the future. However, it has to be noted that in spite of prognoses made from earthquake observations of several hundred or even of several thousand years surprising seismic events may occur. On less active areas, like Hungary, long term prediction cannot be given from short term observations, however, short term predictions reflect the seismicity to be expected in most of the cases. As the source and time of expectable shocks are not known exactly, these are probability variables and are assumed to be independent. It will be shown that when investigating smaller areas the independence of input parameters (time of the earthquake, intensity in the epicentre) cannot be ensured. Some of the calculation methods assume that the number of earthquakes within a time interval t show Poisson distribution. In spite of the fact that this distribution does not reflect the processes of accumulation and release of stress, the frequency of earthquakes is well described by it in many cases.

Calculation of the seismic risk of the region was carried out by the method of CORNELL [1968]. Without discussing the method let us consider the basic relations. Intensity can be determined from the magnitude (M) and focal distance (R) of the earthquake using the following equation

$$I = c_1 + c_2 M - c_3 \ln R \quad (1)$$

Coefficients c_i can be determined by root mean square methods. The probability that intensity I of the earthquake, having occurred at focal distance $R = r$, exceeds a random i value at surface point S can be given by the following expression

$$P(I \geq i | R = r) = P[(c_1 + c_2 M - c_3 \ln r \geq i | R = r)] \quad (2)$$

where $P(A/B)$ is the conditional probability of event A on event B . Assuming that M and R are independent

$$P(I \geq i | R = r) = P\left(M \geq \frac{i + c_3 \ln r - c_1}{c_2}\right) = 1 - F_M\left(\frac{i + c_3 \ln r - c_1}{c_2}\right)$$

where $F_m(m)$ is the distribution function of the magnitude. The connection between the number of shocks n_M with a magnitude equal or exceeding M is

$$\log n_M = a - bM \quad (3)$$

Coefficients a and b can be determined by adjustment of points in a log-normal scale.

Assuming that seismic events follow a Poisson distribution and their yearly frequency is low, the average repetition period of earthquakes and their yearly expected intensity can be calculated. It shall be noted, however, that in spite of the widespread use of the Poisson distribution for risk calculation, it does not reflect the stress accumulation preceding the earthquakes.

3. Seismic risk of the investigated region

After the above theoretical considerations it has to be examined if the observed data on earthquakes are suitable for risk calculations. The first question is the length of the observation period. Since regular observation of earthquakes in Hungary actually started in 1757, it would be expedient to process data from that date until now. It is a fact that since the introduction of instrumental observations at the beginning of the 20th century more reliable data are available, but as was mentioned before, during this relatively short time, no significant seismic event occurred, except at Várpalota. It is obvious that the longer the observation interval, the more reliable the results will be.

Earthquakes are usually followed by several aftershocks which cannot be regarded as independent seismic events. Since 1757 there have been several hundreds of earthquakes in the area, and main shocks had to be selected from

them. Lacking a better solution researchers consider a new earthquake as main shock after a certain inactive period (months, years). Thus the separation of main shocks and aftershocks is rather subjective. As a first approximation, events were considered main shocks if further earthquakes were not observed within an area of 10 km radius during the next year. Considering the fact that aftershocks may occur even years after the main shock, in the one year time span after the main shock aftershocks with several years of time delay may be represented. During the last 226 years only 44 earthquakes, satisfying the conditions, were identified. Distribution of the earthquakes during this time is shown in Fig. 7. As it can be seen, earthquakes occurred sometimes very shortly after each other. In the case of independent events, the probability of this is rather low, its order of magnitude can be estimated by the following consideration: let us separate the region to a northern and a southern part by halving the number of shocks. The partition line will fall between Bakonysárkány and Aka. The probability of the occurrence of 5 earthquakes within 1 year from 22 shocks on the northern and 22 on the southern part during 226 years can be calculated by the following relationship:

$$p = \frac{(N-k)!}{(n-k)! (N-n)!} \cdot \frac{N!}{n!(N-n)!} = 5.6 \cdot 10^{-6}$$

where n = the number of earthquakes (22)

N = the time span under investigation (226)

k = number of earthquakes on both source areas within the same year (5).

As the value of p is rather low, the two source areas cannot be regarded independent.

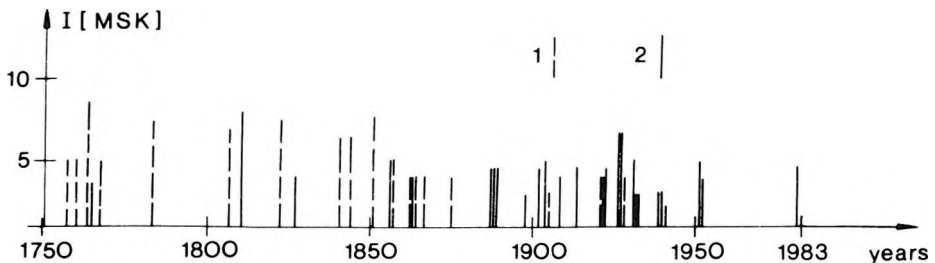


Fig. 7. Main earthquakes from 1763 till the present in the Komárom-Várpalota region
1 — Komárom sources; 2 — other sources

7. ábra. 1763-től napjainkig kipattant „főrengések” Komárom-Várpalota környezetében
1 — komáromi források; 2 — egyéb források

Рис. 7. «Главные» трясения с 1763 г. до наших дней окрестности Комаром-Варпалота
1 — комаромские очаги; 2 — другие очаги

The cause of the interaction of earthquakes is not known exactly, it is possible that there is some connection between the Mór trough and the fault lines near Komárom, however, no obvious geophysical or geological evidence supports it. The Vértes hills were uplifted during the last 1–2 million years [RÓNAI 1973] and as a result, significant stresses have been accumulated in the region, which are released periodically. It is possible that the energy release in one of the sources disturbs the accumulation of stresses in the other one. Irrespective of the reason for the connection between the sources it is quite probable that an earthquake in one source area will be followed by another one on the other side.

It has been mentioned that the number of earthquakes during a time unit will be of Poisson distribution. We have checked the assumption with the χ^2 test for our selected data. They followed the Poisson distribution with such low significance level ($P_{0.05}^{(1)}$) that the justification of our assumptions is doubtful. It is obvious that the assumptions made on independent earthquakes were incorrect — as was proven by the previous reasoning. If we impose stricter conditions by regarding events independent only if their spacing is at least one year on the whole area, for the 35 earthquakes selected on this basis the assumption of the Poisson distribution can be regarded justified ($P_{0.5}^{(1)}$).

For the calculation of the seismic risk the constants of a , b and c_i in Eqs. (1) and (3) should be determined from sufficient number of n_M , M , I , and R values. Before the introduction of instrumental recording, the magnitude of earthquakes could not be determined directly from seismograms, therefore we have determined the magnitudes of these shocks from their intensity in the epicentre and the source depth using the well known expression:

$$M = k_0 + k_1 I_0 + k_2 \log h.$$

The constants were determined from the magnitudes (M), source depths (h) and epicentral intensities (I_0) of 14 well documented earthquakes in Hungary:

$$M = 0.53 + 0.63 I_0 + 0.09 \log h. \quad (4)$$

Magnitudes of the earthquakes were determined by the method of BISZTRICSÁNY [1974], the depth of source with that of SPONHEUER [1960]. Intensities of earthquakes were always given in the MSK scale. Sometimes, however, the depth of the source could not be determined; in these cases, calculations were carried out with 7 km average depth value. This focal depth was taken partly because statistics show that earthquakes along faults never exceed this value and partly because a significant part of the earthquakes in Europe originates at a depth of 7–8 km [KÁRNÍK 1968]. Focal depths of 91 earthquakes in Hungary were determined by CSOMOR and KISS [1958, 1962]. The most common focal depth was found to be between 4 and 7 km. Regarding the problem of focal depth it should be mentioned that the coefficient of the third member in Eq. (4) is significantly less than that of the first and second members thus the few kilometers error made in the calculation of focal depth causes only 0.1–0.2 difference in the magnitude. Although the coefficients in KÁRNÍK'S [1968] equation

for Czechoslovakia differ from those given in Eq. (4), this causes only minor differences in the magnitudes being important in engineering practice.

If the magnitudes of earthquakes and the number of shocks are known, constants a and b in Eq. (3) can be determined. As earthquakes below magnitude 3 are observed on limited areas only, these are often not reported to the authorities — especially in the case of historical earthquakes. This might be the reason for knowing much less earthquakes of lower magnitudes than theoretically expected. For this reason earthquakes of magnitudes lower than 3 were not taken into account for the calculation of constants a and b . As it is known the value of a depends on the duration of the observation period, on the size of the investigated area and on the level of seismic activity. Coefficient b is more constant and varies according to the geological age of seismotectonic zones [MIYAMURA 1962]. It is obvious that, depending on the size of the area and the source geometry (line source or point source) chosen for the basis of the calculations, the values of constants a and b will also change. For the calculation of the seismic risk two models were selected. According to the first one, any earthquake in the future will originate along the fault parallel with the line connecting Komárom and Várpalota at a depth of 7 km. Although this model is not in concordance with the observations it takes into account unexpected seismic events resulting from the structure of the region. According to the second model future earthquakes are to be expected mainly in the region of Mór–Isztimér and Komárom. Constants a and b for both models are shown in Figs. 8 and 9.

Constants c_i in Eq. (1) were determined from the I , M , R values of the earthquakes observed in Hungary, i.e. the relation was supposed to be valid for the whole country. The values used for the determination of constants c_i are shown in Fig. 10. It is clear that earthquakes of the same magnitude can result in two or three times higher intensity — especially in the range of smaller magnitudes — even for equal focal distances, which shows the high degree of uncertainty of the determination of isoseisms and magnitude. For Hungary the c_i values determined from 99 sets of data gave the following relationship:

$$I = 2.80 + 1.44M - 1.50 \ln R \quad (5)$$

It is interesting to note that, comparing the above relationship with that for California [ESTEVA and ROSENBLUETH 1964], intensities belonging to magnitude 5 for the whole range of local distances in question of engineering problems exceed the values calculated from (5). To determine the seismic risk, the biggest earthquake to be expected in the given area has to be known. On the basis of the observations in the Caucasus, BORISSOFF, REISNER and SHOLPO [1976] determined the active zones of Hungary too. For the region under investigation they have predicted earthquakes of maximum 6.5 magnitude. This magnitude generally corresponds to a shallow source earthquake of about 8.5° epicentral intensity, in agreement with our observations.

In calculating seismic risk we divided the area to a 10 × 10 km grid and computed the intensity of earthquakes (probabilities: 0.02; 0.013; 0.01; 0.007

etc.) to be expected with 50, 75, 100 and 150 years frequencies in the intersection points. Points with the same expected intensity were connected. Thus the isolines do not mean the effect of an earthquake occurring somewhere along the fault is represented by isoseisms of this shape.

According to the first model, intensity of 7° is expected with 0.02 probability on 1600 sq. km area, while that of 8° is expected with 0.013 probability on 1000 sq. km area (Fig. 11). As these values are not supported by observations the results should be considered with some reservations. For example, an earthquake with an intensity of 8° in a 10 km region of the fault will reach 8.5° epicentral intensity (see Fig. 11, frequency 75 years). Thus calculating for further frequencies (100 years or more) has no reason at all.

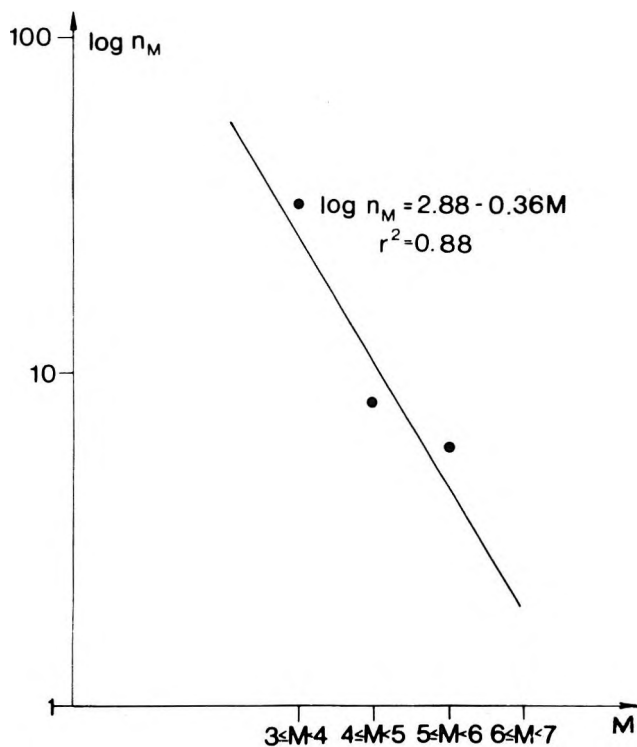


Fig. 8. Relation between the number and magnitude of earthquakes originating between Várpalota and Komárom, Model I

n_M = number of earthquakes with magnitudes $\geq M$; r = correlation coefficient

8. ábra. Várpalota és Komárom között kipattant földrengések száma és magnitúdója közötti összefüggés, I. modell

n_M = rengések száma, amelyek magnitúdója $\geq M$; r = korrelációs koefficiens

Рис. 8. Связь между количеством и магнитудой землетрясений в окрестности Варпалота-Комаром, модель I

n_M = количесиво землетрясений с магнитудой $\geq M$; r = коэффициент корреляции

According to the second model, two sources are assumed on the area under investigation: one at Komárom and the other at Mór–Isztimér. This latter one at the midpoint between the two settlements and both sources at 7 km depth. For this model the areas of equal intensities were determined even for the

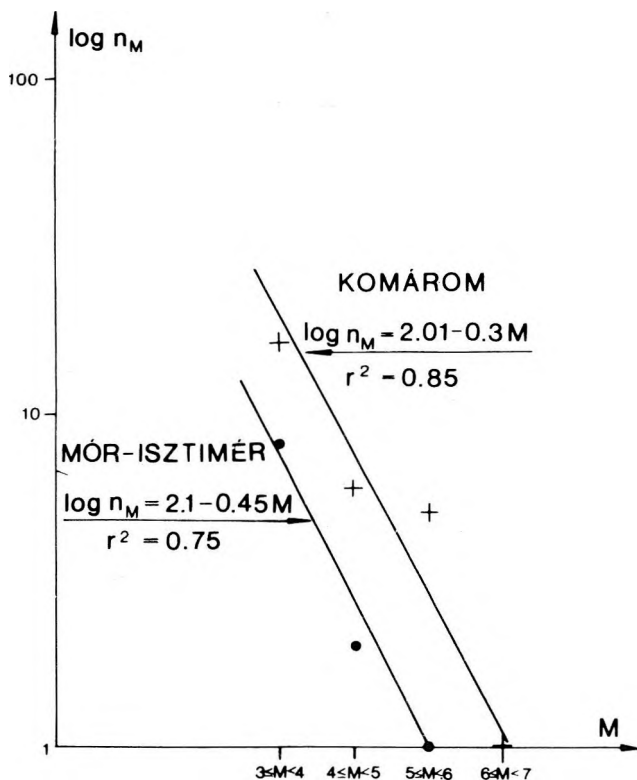


Fig. 9. Relation between the number and magnitudes of earthquakes originating from the Komárom and the Mór–Isztimér sources, Model II

n_M = number of earthquakes with magnitudes $\geq M$; r = correlation coefficient

9. ábra. Komáromi és mór–isztiméri forrásokban keletkezett földrengések száma és magnitúdója közötti összefüggés, II. modell

n_M = rengések száma, amelyek magnitúdója $\geq M$; r = korrelációs koefficiens

Рис. 9. Связь между количеством и магнитудой землетрясений, образовавшихся в комаромском и мór–истимерском очагах, модель II

n_M = количество землетрясений с магнитудой $\geq M$; r = коэффициент корреляции

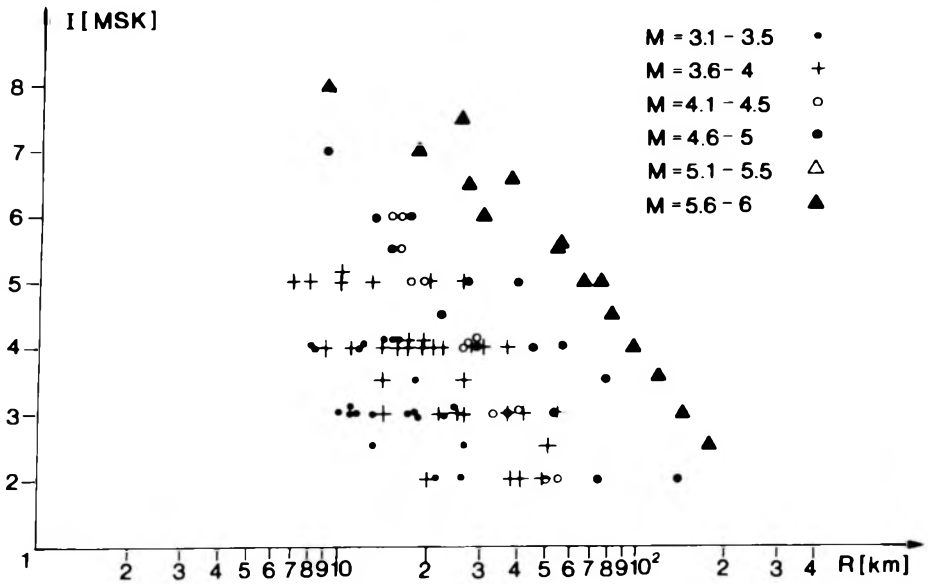


Fig. 10. Relation between earthquake magnitudes (M) and intensities (I) versus source distance (R)

10. ábra. Földrendgések mérete (M) és intenzitása (I) az R forrástávolság függvényében

Рис. 10. Размер (M) и интенсивность (I) землетрясений в зависимости от удаления источника (R)

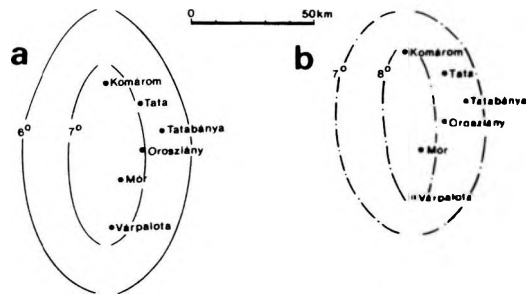


Fig. 11. Expected intensity according to Model I, with 50 years (a) and 75 years (b) frequency

11. ábra. Komárom és Várpalota között 7 km mélységben feltételezett törésvonal környezetében várható megrázottság 50 éves (a) és 75 éves (b) gyakorisággal

Рис. 11. Ожидаемая потрясаемость с частотой 50 лет (a) и с частотой 75 лет (b), в связи с предполагаемым разломом на глубине 7 км, между Комаром и Варялота

frequencies of 100 and 150 years (Fig. 12). The area of intensity of 7° exceeds 2000 sq. km for the 150 years case. This value has to be considered also with reservation because it follows from Eq. (5) that an earthquake of $M=6.5$ magnitude — regarded as expected maximum magnitude — will cause lower than 7° intensity at 30 km distance from the source. Thus we cannot expect simultaneous effect of both sources — being some 45 km apart — on some parts of the area. Therefore the size of the area with an intensity of 7° should be

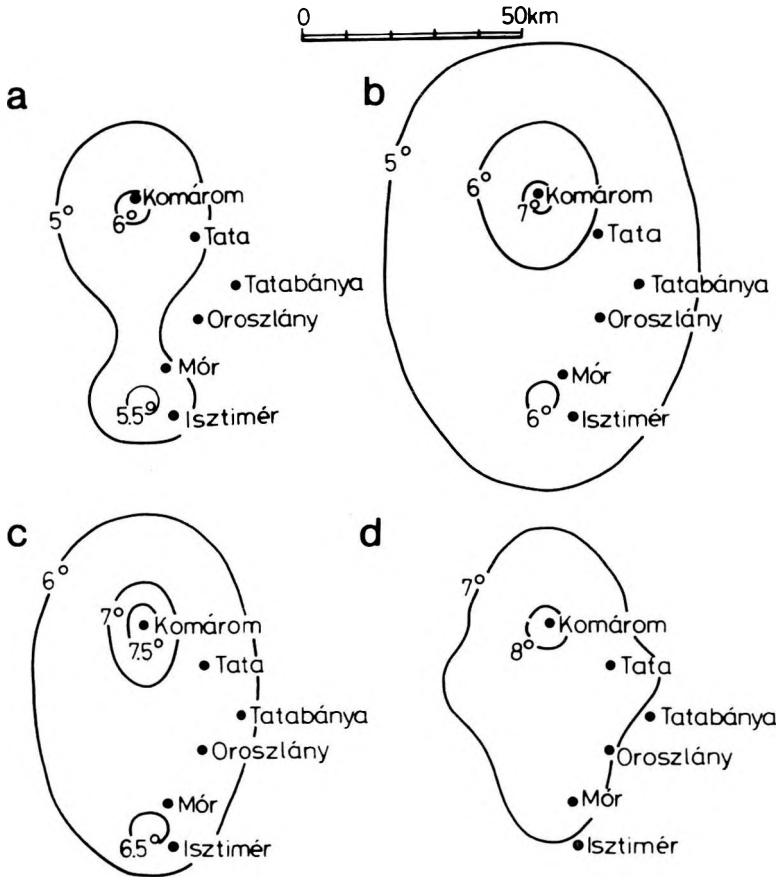


Fig. 12. Expected intensity according to Model II, with 50 years (a), 75 years (b), 100 years (c) and 150-years (d) frequency

12. ábra. Komáromi és mór-isztiméri források környezetében várható megrázottság 50 éves (a), 75 éves (b), 100 éves (c) és 150 éves (d) gyakorisággal

Рис. 12. Ожидаемая потрясаемость с частотой 50 лет (a) 75 лет (b) 100 лет (c) и 150 лет (d) в окрестности комаромского и мór-истимерского очагов

considered slightly overestimated. In the surroundings of Komárom, intensity of 8° can be expected with a frequency of 150 years. Determining the seismic risk of this area the Mór–Isztimér source shall not be taken into account.

Results follow observations as much as the special features of local earthquakes could be taken into account. As the effect of the Mór trough, the isoseisms are elongated in its direction — as can be seen in Fig. 5. In our calculations we have not taken this effect into account but utilized Eq. (5). The intensity modifying effects of the frequency dependent subsurface, were not considered either. Therefore our results are of informative nature only and on-site investigations are required before any new constructional project is sited on the area.

4. Reliability of the results

For the reliability of the results the following apply:

- Errors in the calculation of constants a , b , c_i cause $\pm 0.5^\circ$ uncertainty in the isoseisms.
- Selection of independent events is subjective.
- The Poisson distribution does not reflect the process of accumulation and release of strain.
- The models assumed significantly influence the results of the calculation.
- The seismicity of the area is not stable, seismic periods are followed by aseismic ones.

Considering the fact that the results of the above calculations are of limited reliability, it is necessary to try to estimate the seismicity of the area by some other method based on simple considerations. It is known that the time dependent subtotal of the Benioff number (S_B) is characteristic of the stress accumulation processes of an area [BENIOFF 1951]. The characteristic S_B values for Hungary and separately for the Transdanubian area — from earthquakes observed between 1880 and 1956 — were calculated by CSOMOR and KISS [1958, 1962]. It was established that during period of investigation the accumulation and release of the energy in Transdanubia was a uniform, continuous process. Contradicting this statement, large steps can be observed in the values of S_B before 1851 because of the earthquakes of Komárom and Mór (Fig. 13). Most probably between 1599 and 1757 only smaller earthquakes occurred, which were not recorded. From 1757 the seismicity of Komárom increased: several earthquakes, causing significant devastation, were registered until 1851. After that an inactive period followed when earthquakes of smaller energy were recorded only. This inactive period was probably not characterized by equilibrium but by the accumulation of stresses. To estimate the rate of stress accumulation let us assume that after the earthquake of 1599 the area became balanced and the building-up of stresses started, which lasted till 1757 (no earthquakes were experienced between the two dates).

An alternating stress accumulation and release process can be observed

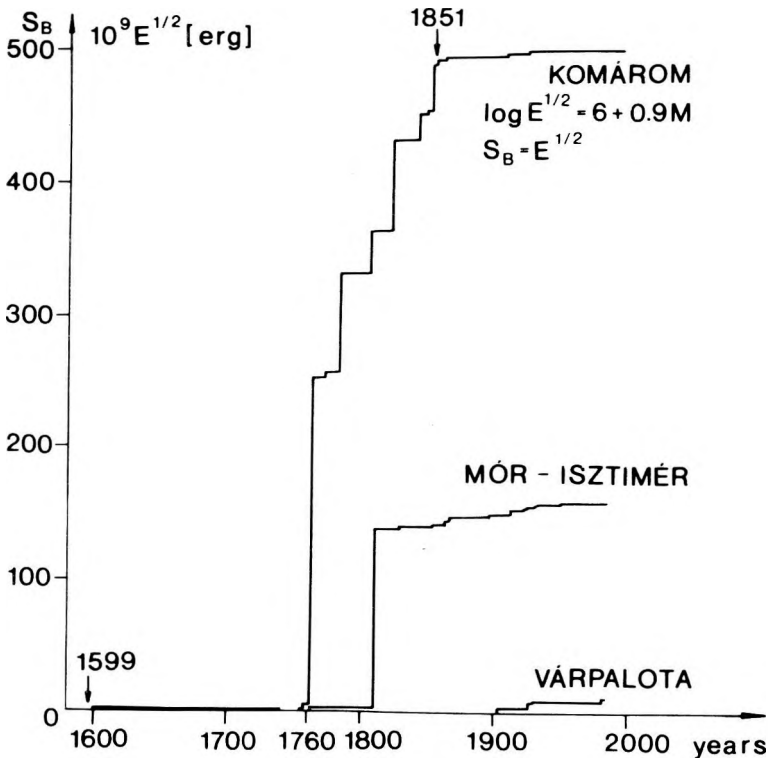


Fig. 13. Released energy, characterized by the Benioff number (S_B)

13. ábra. A három forrásterületről felszabadult energia Benioff-számmal (S_B) jellemzett értékének változása

Рис. 13. Изменение значения охарактеризованной числом Бенъоффа (S_B) освобожденной с трех очагов энергии

from 1757 till 1851, when — after 252 years — the source became inactive again. During this period the average increase of the Benioff number was:

$$S_B = 1.94 \cdot 10^9 \text{ erg}^{1/2}/\text{year}$$

while from 1851 to the present days:

$$S_B = 0.05 \cdot 10^9 \text{ erg}^{1/2}/\text{year}.$$

Assuming that the rate of stress accumulation has not changed from 1599 until now, $1.89 \cdot 10^9 \text{ erg}^{1/2}/\text{year}$ stress is accumulating since 1851. This means that the S_B value corresponding to an earthquake of magnitude 6 accumulates during 123 years.

The weakest point of our reasoning is the assumption of the state of equilibrium in 1599. As was mentioned earlier there was an earthquake causing

damages to buildings in Komárom in that year. The epicentre of the earthquake, however, is not known. In connection with that earthquake RÉTHLY [1952] mentioned three possible alternatives:

- The earthquake occurred in the surroundings of Komárom.
- The earthquake was detected on a large area and the source was probably beyond the borders of Hungary, perhaps in Austria.
- It was an earthquake of double source.

The facts that chimneys collapsed in Komárom, the earth was quaking for a longer time and springs broke forth lead to the conclusion that the source of the shock could not be in Austria, otherwise it should have been detected on areas nearer to the hypocentre, e.g. in Pozsony or Győr, but damages were not reported from these settlements. Most probably the source must have been somewhere between Komárom, Esztergom and Érsekújvár (Nové Zámky), because damages to buildings were reported from these towns.

Drawing long range conclusions from uncertain data is rather risky. If it is assumed that the earthquake of 1599 occurred within a stress accumulation period, and not all the stresses were released, the above considerations are not valid. This means that the rate of stress accumulation from 1851 to the present days is lower than estimated. It cannot be stated that the accumulated energy will be released in one single big earthquake, but most probably, as in the past, several smaller earthquakes will be experienced in the future too.

Appendix

Extracts from the report on the damages caused by the Komárom earthquake of 1763 at Buda (to be found in the National Archives, Loc. ant. 2724) translated from the latin original: "Memorable de terrae motu Consilio Locumtenentialy per Magistratum Budense 29 Julii, 1763".

In the Water Town (Fig. 3 — in the following, reference will always be made to this figure) most of the population detected earthquakes, early in the morning: three o'clock a smaller one and at quarter past five a bigger one, but neither of these caused damages. A quarter of an hour later an earthquake lasting for about one minute caused building damages mainly in the Castle District and in the Upper Town:

The crucifix of the Franciscan church fell down (1).

Stones fell down from the arches of the church of the Jesuits and walls of the rooms and corridors of the Monastery cracked (2).

Stones fell out from the walls of houses marked (3) and tiles fell down from the roofing.

In the Monastery of the Carmelites frames of the doors shifted in the walls, walls cracked (4).

Arches were damaged in the houses marked 5, 6, 10.

In the Water Town roofing of the houses were damaged, on the first floor

the covering of the ceiling fell off to the girders, some of the buildings are in the danger of collapsing (6).

Rooftiles fell down from the roofing of the church of Franciscans (7).

One of the crucifixes of the Parish church bent down together with the orb, walls were cracked and the upper part of the chimney fell down (8).

The stone ball fell down from the top of the Capuchin church (9).

The flow of water in the bath of Taban has increased and sprays far (11).

Water flow of the Gellért Bath increased: the flow is spurting far with a diameter of a man's leg (12).

REFERENCES

- BISZTRICSÁNY E. 1974: Engineering seismology (in Hungarian). Akadémiai Kiadó, Budapest, p. 215
- BENIOFF H. 1951: Earthquakes and Rock Creep. Part I: Creep Characteristics of Rocks and the Origin of Aftershocks. *Bull. Seism. Soc. Am.* **41**, 1, pp. 31–62
- BORISSOFF B. A., REISNER G. I., SHOLPO V. N. 1976: Tectonics and maximum magnitudes of earthquakes. *Tectonophysics*, **33**, 1–2, pp. 167–185
- CORNELL C. A. 1968: Engineering Seismic Risk Analysis. *Bull. Seism. Soc. Am.* **58**, 5, pp. 1583–1606
- CSOMOR D., KISS Z. 1958: Seismicity of Hungary. Part I. (in Hungarian). *Geophysical Transactions*, **7**, 3–4, pp. 169–180
- CSOMOR D., KISS Z. 1962: Seismicity of Hungary. Part II. (in Hungarian). *Geophysical Transactions*. **11**, 1–4, pp. 51–75
- ESTEVA L. and E. ROSENBLUETH 1964: Spectra of earthquakes at moderate and large distances. *Soc. Mex. de Ing. Sismica, Mexico* **2**, pp. 1–18
- KÁRNÍK V. 1968: Seismicity of the European Area. Part I. Czechoslovak Academy of Sciences, Praha, 364 p.
- MIYAMURA S. 1962: Magnitude-frequency relations and its bearings to geotectonics. *Proc. Japan Academy*, **38**, 1, pp. 27–30
- RÉTHLY A. 1952: Earthquakes in the Carpathian Basin (455–1918) (in Hungarian). Akadémiai Kiadó, Budapest, p. 510
- RÓNAI A. 1973: Map of crustal movements during the Quaternary (in Hungarian). *Geonómia és bányászat*, **6**, 1–4, pp. 241–243
- SIMON B. 1932: Data on the earthquake at Mór on the 14th of January 1810 (in Hungarian). *Székesfehérvári Szemle*, **11**, 7–8–9 (July–September), pp. 43–45
- SPONHEUER W. 1960: Methoden zur Herdtiefenbestimmungen in der Makroseismik. *Freiberger Forschungshfte*, C 88, Geophysik, pp. 1–117
- SZEIDOVITZ GY. 1984: Reinterpretation of the epicentral intensities and of the depth of the hypocentre of some Hungarian earthquakes (in Hungarian). *Földtani Kutatás*, **27**, 3, pp. 71–80

FÖLDRENGÉSEK KOMÁROM, MÓR ÉS VÁRPALOTA KÖRNYEZETÉBEN

SZEIDOVITZ Győző

Komárom, Mór, Várpalota szűkebb környezete az elmúlt néhány évszázad megfigyelései alapján hazánk egyik legaktívabb területének bizonyult. Feltételezve, hogy a vizsgált környezet átlagos szeizmicitása a jövőben sem fog lényegesen változni, Cornell eljárásával kiszámítottuk a területen várható földrengés kockázatot.

ЗЕМЛЕТРЯСЕНИЯ В ОКРЕСНОСТИ ГГ. КОМАРОМ, ВАРПАЛОТА, МОР

Дьёзё СЕЙДОВИЦ

Окресность гг. Комаром, Мор, Варпалота по данным наблюдений за прошедшие несколько веков является одним из самых активных участков Венгрии. Предполагая, что средняя сейсмичность исследуемого участка не будет в будущем изменяться, методом Корнелла рассчитан ожидаемый риск землетрясений.